ANL/ESD/TM--1

DE90 008159

ANL/ESD/TM-1

Computer Modeling of Erosion in Fluidized Beds

by R.W. Lyczkowski, J.X. Bouillard, D. Gidaspow,* and G.F. Berry

Energy Systems Division,
Argonne National Laboratory, 9700 South Cass Avenue, Argonne, Illinois 60439

July 1986 (published January 1990)

Work sponsored by United States Department of Energy,
Morgantown Energy Technology Center

---

*Gidaspow is affiliated with the Illinois Institute of Technology, Department of Chemical Engineering, Chicago.

CONTENTS

CONTENTS (Cont'd)

FIGURES

FIGURES (Cont'd)

FIGURES (Cont'd)

TABLES

FOREWORD

This report summarizes early progress in the Argonne National Laboratory program in modeling erosion in fluidized beds. Unfortunately, during subsequent progress in the program, the report's preparation and production was delayed. Since the initial drafts were written, both the hydrodynamic model and the monolayer energy dissipation (MED) model developed herein have been significantly improved. Although many of the conclusions presented here remain valid, the authors advise that readers note the above caveat when examining the results of the hydrodynamic computations and the MED and Finnie erosion models contained herein.

ACKNOWLEDGMENTS

This work was performed for the U.S. Department of Energy, Morgantown Energy Technology Center. The Project Manager from Oct. 1, 1984, through Sept. 30, 1985, was Thomas J. O'Brien. We thank him for his many suggestions and helpful comments, and, particularly, for his moral and financial support during that period, as well as for later careful review of the draft manuscript of this report. The project was managed after Oct. 1, 1985, by Holmes A. Webb, whom we thank for suggesting the monolayer energy dissipation erosion model. Our thanks, also, to Professor S.L. Soo for confirming the calculations in Section 3.2.1.

We thank Shyh-Tsung Cheng for measuring the experimental time-averaged porosities, Yong-Chil Seo for taking the high-speed motion pictures, and the National Science Foundation for financial support for the experimental phase of this work, performed at the Illinois Institute of Technology.

COMPUTER MODELING OF EROSION IN FLUIDIZED BEDS

by

R.W. Lyczkowski, J.X. Bouillard, D. Gidaspow, and G.F. Berry

ABSTRACT

Erosion in fluidized-bed combustors, which comprises a near-commercial method of burning coal cleanly, has surfaced as a serious issue that may have adverse economic effects. The evidence suggests that the key to understanding this erosion is detailed knowledge of the coupled and complex phenomena of solids circulation and bubble motion. The FLUFIX computer code has been developed for this purpose. Computed hydrodynamic results compare well with limited experimental data (including the bubble frequency and size and the time-averaged porosity distribution) taken in a thin two-dimensional rectangular fluidized bed containing a rectangular obstacle. Six erosion models, which form a preliminary consolidation, are critiqued; a methodology is described whereby the computed hydrodynamic results can be used with these erosion models. All previous attempts (none involving fluidized beds) to couple fluid mechanics and erosion models are reviewed. Both transient and time-averaged energy dissipation models are developed, and shown to generalize the so-called power dissipation model used successfully to analyze slurry jet pump erosion. It is demonstrated, by explicitly introducing the force of the particle on the eroding material surface, that impaction and abrasive erosion mechanisms are basically the same. Linkage is made to the single-particle erosion models. The implementation and finite-difference equations are summarized. Finally, transient, time-averaged, and time-averaged transient energy dissipations for the energy dissipation and Finnie erosion models are compared. The computed erosion rates are compared with each other and with available erosion data literature to validate the calculations. The results are reasonable, but a single-obstacle erosion experiment is necessary, to validate the computations.

1 INTRODUCTION

1.1 FLUIDIZED-BED COMBUSTORS

Fluidized-bed combustors (FBCs) are being developed as a means of burning high-sulfur coal in an environmentally acceptable manner. Atmospheric fluidized-bed combustors (AFBCs) are already enjoying some success in the industrial marketplace as a

highly competitive technology for producing heat and process steam while meeting stringent pollutant emission regulations. Pressurized fluidized-bed combustors (PFBCs) at 10-16 atm (1.01-1.62 MPa) for use in combined-cycle electricity generation have progressed to pilot-plant scale. Because PFBCs are more compact, provide better environmental performance, and have higher thermal efficiency than AFBCs, the former may be used more successfully for power generation.

Erlich[1] has reviewed the substantial progress made in FBC technology since 1970, when the Clean Air Act was passed by the U.S. Congress. Fluidized-bed combustion had been the subject of research on a small scale from the early 1970s in the U.S., as well as in England.[2-4] (The concept and usage of fluidized beds, however, goes back to the 1920s-to-1930s.[3,4]) The environmental benefits that attracted interest in the 1970s were (1) the reduced nitrogen oxides (NO_x) emissions made possible by lower (800-900°C) coal combustion temperatures and (2) up to 90% SO_2 capture using limestone directly in the fluidized bed.[5] Because of the lower combustion temperatures, the ash is below its sintering or melting point and little or no alkali metal vaporization occurs. Thus, buildup of clinkers and undesirable deposits on the tubes immersed within the fluidized bed, on the waterwalls containing the bed, and downstream in the convection pass tube banks is minimized.

The U.S. oil embargo in 1973 further stimulated interest in FBC technology development.[4,6] With the effects of acid rain apparently accelerating -- including the death of large portions of forests and of all animal life in many lakes and ponds in Europe and now in the U.S. -- FBC technology seems certain to attract increased interest.

In 1969, the U.S. Environmental Protection Agency (EPA) began exchanging information with the National Coal Board (NCB) in England.[2,3] Close cooperation continues to this day at the Grimethorpe Experimental PFBC Facility in England. This project, which started in 1975, was funded equally by England, the Federal Republic of Germany, and the United States under the auspices of the International Energy Agency (IEA). An overall project review has been issued recently.[7]

The Tennessee Valley Authority (TVA) and the Electric Power Research Institute (EPRI) have operated a 20-MW(e) AFBC since 1982 and are proceeding with plans for a 160-MW(e) demonstration plant.[1] Krishnan et al.[6] have recently reviewed U.S. FBC technology. Erlich[1] points out that some 50 companies in 25 countries offer fluidized-bed boilers for sale. These boilers range in size from 1 MW(t) to more than 100 MW(t), and units up to 490 MW(t) in size are being designed. Fluidized-bed combustion appears to be destined for commercial success in the 1980s.[4,5]

1.2 THE EROSION ISSUE

Fluidized-bed combustors apparently work better than could have been anticipated, a rather unusual situation for a new technology. However, the issue of erosion has surfaced as a serious problem. Some thought was given to the erosion of tubes in FBCs in 1970[1]; however, the general attitude held then was that erosion was not a problem.[8] In the few instances where erosion was noticed, it was localized and appeared to be the result of unusual conditions that could be resolved by changes in

operating conditions and design modifications. The units were small and operated for short periods of time, typically no more than 1000 h.

Most materials work on fluidized-bed combustion systems has been concerned with corrosion of in-bed components or with combined erosion-corrosion of gas turbine blading materials, because the latter problems were thought to be more severe than erosion of in-bed components. Stringer[8] argued that, given the existing erosion criteria, one would conclude that erosion should not be a problem in fluidized beds under "normal" conditions.

As more FBC units of large scale have accumulated substantial numbers of operating hours, more instances of general, rather than localized erosion have been encountered. For instance, severe wear on in-bed tubes was reported by the International Energy Agency/Grimethorpe (IEA/G) PFBC facility in 1982.[9] The maximum tube wall metal wastage after 468-h operation was 1.2 mm, which is more than 50% of the 2-mm minimum thickness considered acceptable for safe operation. This translates into an erosion rate of 2.5 mm/1000 h. Because the tube walls are only 4.5 ± 0.5 mm thick, failures would begin to occur in less than 2000 h (about two months) of continuous operation. Intensive, short-term investigations at a number of institutions under contract to IEA/G resulted in the recommendation of design changes (lower fluidizing velocity, fins on tubes, etc.) that achieved partial mitigation of the wear and allowed the test program to be continued.

Several tube failures actually occurred in a 16-MW(t) AFBC after approximately 4000 h of service.[10] The initial tube wall thickness was 4.2 mm; hence, the average erosion rate was 1 mm/1000 h. In China, where more than 2000 FBC boilers are in operation, FBC boiler developers report excessive erosion rates, 1.3 mm/1000 h, of in-bed tube surfaces, probably resulting from the use of low grade Chinese coals of high ash content.[11] In-bed tubes in China are partially protected from excessive erosion through the use of fins and studs, which break up solids flow patterns around the tubes. These measures have not been completely successful in eliminating tube wear, but they may extend tube life by a factor of almost 20. Tube bank lifetimes of 100,000-160,000 h (10-15 y) are not yet possible.

Other FBCs, such as the 1.81 m x 1.81 m, approximately 2-MW(e) Babcock & Wilcox (B&W)-EPRI research AFBC at Alliance, Ohio, and the overbed feed 3.6 m x 5.5 m, 20-MW(e) TVA-EPRI pilot plant AFBC at Paducah, Kentucky, apparently have operated for thousands of hours without showing any appreciable evidence of erosion.[6,8] The B&W facility did experience severe bundle damage when a deflector plate was lost,[8] and the TVA/EPRI facility experienced erosion in the underbed feed system.[6]

Circulating fluidized-bed combustors (CFBCs) eliminate in-bed tubes and rely on vertical water walls to remove heat. Refractory lining is required on the walls of the hot cyclones to prevent erosion. Bubbling FBCs (BFBCs), rather than CFBCs, are of primary interest in this report. However, the methodologies and models developed are general and would be applicable to CFBCs, as well as to both AFBCs and PFBCs and other in-bed and out-of-bed components (such as fuel feed-nozzles, waterwalls, and the gas-pass boiling bank, where erosion has also been found to occur).[5,9,12] The Georgetown AFBC had 452 of its 980 gas pass boiling bank tubes replaced after 13,636 h of operation, as a

result of severe erosion. Hereafter, where reference is made to FBCs, it is to be understood that they are BFBCs.

Erosive wear of materials is known to be controlled by several complex phenomena that influence the erosion behavior of heat-exchanger tubes and support hangers in FBCs. Among these phenomena are (1) the feedstock characteristics, such as chemical composition, particle size and size distribution, and hardness; (2) the operating conditions, such as fluidizing velocity, temperature, and pressure; and (3) the mechanical design of the combustor, including the diameter and pitch of tubes within tube bundles, distance from the air distributor and coal and limestone introduction points, and materials of construction for tubes and support hangers. The complex interaction of these variables determines the nature and quality of fluidization (slugging vs. smooth), the combustion gas composition, the possible formation of protective deposits or excessive corrosion, and, finally, the rate of erosion.

Stringer and Wright[8,12] have indicated that a number of additional erosion mechanisms may operate in FBCs, although not at all times or in all units. These mechanisms include:

- Particles "loaded" onto the surface by a block of other particles.
- Fast-moving particles in the wake of rising bubbles.
- Large, but slow-moving, particles with high kinetic energy.
- Particles thrown onto metal surfaces by the collapsing of bubbles.
- Particles accelerated onto in-bed components under the influence of in-bed jets associated with coal and limestone feedports, limestone recirculation ports, and air streams used to keep bed drains clear of obstructions.
- Particles trapped within and moving with large-scale flow patterns (gulf streams) in the fluidized bed.

In summary, it is not possible at present to explain why some fluidized beds or bed regions experience rapid erosion and others do not. Consequently, it is not possible to suggest completely satisfactory remedies or design a fluidized bed for which it is known that erosion would not be a problem. The ad hoc approaches mentioned above are unlikely to succeed in the long term without a better understanding of the underlying processes.[8] One of the major objectives of this study is to improve that understanding.

2 MODELING OF FLUIDIZED-BED SOLIDS MOTION

The key to understanding erosion in fluidized beds is a detailed knowledge of the coupled and complex solids circulation and bubble motion. Much experimental work in gas-solid[13] and gas-liquid-solid[14] fluidized beds has been carried out during the last 30 years. The aim of that work has been to understand bubble formation, frequency, size, and velocity and the manner in which the bubbles affect the mechanisms of mixing, heat transfer, gasification, and combustion. Not until quite recently, with the emergence of the erosion issue, has equivalent experimental work been done to investigate the effects of these phenomena on erosion.[15] Therefore, much less is known about how solid particles actually move and interact with system components, in FBC bubbling beds[16] than in beds that do not contain such components.

Because of experimental difficulties, solids motion studies are not common. Motion-picture and photographic techniques have been used in conjunction with thin "two-dimensional" fluidized beds,[17] beds that are much less thick than wide. This approach is both tedious and time-consuming. The uncertainties in determining the particle velocity have been reduced by the "quasistereoscopic" technique, which has a claimed accuracy within ±2.4 mm/s.[18] Miniature, transistorized "radio pills" with in-bed pickups have been used,[19] but the size and density of the pill are not the same as those of the bed material, and the pickups may alter the flow field. Fiber-optic probes have been used, but they too are intrusive and may significantly alter the flow field.[20] A novel nonintrusive, radioactively-tagging facility, the Computer Aided Particle Tracking Facility (CAPTF), has been used to obtain time-averaged solids circulation data in fluidized beds, both with and without immersed tubes.[21,22]

Understanding of how bubbles interact with solid surfaces within fluidized beds is almost nonexistent. These surfaces may take the form of instrument probes used to detect the bubbles themselves[23] and, in the case of fluidized-bed combustors, heat-exchanger tubes and baffles placed in the bed, in the free-board, or both.[24,25]

State-of-the-art computational techniques and improved computing capability have made it possible to model the movement of solids and bubbles in FBCs. Significant progress has been demonstrated in the ability of the hydrodynamic model of fluidization to predict bubble formation (including frequency of formation, growth rate, size, trajectory, rise velocity, and conditions giving rise to bubble splitting). Just as importantly, solids volume fraction and gas velocity computations also have been performed.

The hydrodynamic approach to fluidization, which started with Davidson in 1961,[26] serves as the basis of the three extant two-dimensional fluidized-bed codes: CHEMFLUB, FLAG, and IIT (also called FLUFIX). The capabilities of these codes were reviewed by Smoot[27] and Gidaspow.[28] The progress made in the last ten years of modeling a small-scale, highly instrumented, "two-dimensional" fluidized bed at the Illinois Institute of Technology (IIT), using the FLUFIX computer code, has served in great part to validate the hydrodynamic model.[29-34] This progress has been reviewed recently by Gidaspow.[28]

The FLUFIX computations and validations cited above were performed for fluidized beds containing no obstacles, but the capability exists for including obstacles. Therefore, a model of fluidization in a two-dimensional rectangular bed with a central jet and a rectangular obstacle was formulated, and computations were performed.[35] This section presents a summary of the hydrodynamic model, the computations, and a comparison with the experimental results. The validated hydrodynamic computations are needed as inputs to the various erosion models described in this report.

2.1 HYDRODYNAMIC MODEL

The hydrodynamic model of fluidization uses the principles of conservation of mass, momentum, and energy. The continuity equations and the separate phase momentum equations for two-dimensional, transient, isothermal two-phase flow in Cartesian coordinates, which form the basis of the FLUFIX code, are given below (terms are defined in the Nomenclature at the end of this report):

Gas Phase Continuity

$$\frac{\partial}{\partial t}(\rho_g \varepsilon) + \frac{\partial}{\partial x}(\varepsilon\, \rho_g U_g) + \frac{\partial}{\partial y}(\varepsilon\, \rho_g V_g) = 0 \tag{2.1}$$

Solid Phase Continuity

$$\frac{\partial}{\partial t}[\rho_s(1 - \varepsilon)] + \frac{\partial}{\partial x}[\rho_s U_s(1 - \varepsilon)] + \frac{\partial}{\partial y}[\rho_s(1 - \varepsilon)V_s] = 0 \tag{2.2}$$

Gas Phase Momentum in x-Direction

$$\frac{\partial}{\partial t}(\rho_g\, \varepsilon\, U_g) + \frac{\partial}{\partial x}(\rho_g\, \varepsilon\, U_g U_g) + \frac{\partial}{\partial y}(\rho_g\, \varepsilon\, V_g U_g) = -\varepsilon \frac{\partial P}{\partial x} + \beta_x(U_s - U_g) \tag{2.3}$$

Solid Phase Momentum in x-Direction

$$\frac{\partial}{\partial t}[\rho_s(1 - \varepsilon)\, U_s] + \frac{\partial}{\partial x}[\rho_s(1 - \varepsilon)\, U_s U_s] + \frac{\partial}{\partial y}[\rho_s(1 - \varepsilon)\, V_s U_s] = -(1 - \varepsilon)\frac{\partial P}{\partial x} + \beta_x(U_g - U_s) + G(\varepsilon)\frac{\partial \varepsilon}{\partial x} \tag{2.4}$$

Gas Phase Momentum in y-Direction

$$\frac{\partial}{\partial t}(\rho_g \varepsilon V_g) + \frac{\partial}{\partial x}(\rho_g \varepsilon U_g V_g) + \frac{\partial}{\partial y}(\rho_g \varepsilon V_g V_g) = -\varepsilon \frac{\partial P}{\partial y} + \beta_y (V_s - V_g) - \rho_g \varepsilon g \tag{2.5}$$

Solid Phase Momentum in y-Direction

$$\frac{\partial}{\partial t}[\rho_s(1-\varepsilon) V_s] + \frac{\partial}{\partial x}[\rho_s(1-\varepsilon) U_s V_s] + \frac{\partial}{\partial y}[\rho_s(1-\varepsilon) V_s V_s] = -(1-\varepsilon)\frac{\partial P}{\partial y} + \beta_y (V_g - V_s) - \rho_s (1-\varepsilon) g + G(\varepsilon)\frac{\partial \varepsilon}{\partial y} \tag{2.6}$$

The solids elastic modulus, $G(\varepsilon)$, is used to calculate the normal component of the solids stress through the following relationship:

$$\partial\tau = \frac{\partial\tau}{\partial\varepsilon}\partial\varepsilon = G(\varepsilon)\partial\varepsilon \tag{2.7}$$

which is similar to what is done in solid mechanics. Equations 2.1-2.6 are used in Sec. 5.2 to derive the energy dissipation model.

There are six nonlinear, coupled, partial differential equations for the six dependent variables to be computed: the void fraction, ε; the pressure, P; and the gas velocity components U_g and V_g and the solids velocity components U_s and V_s in the x- and y-directions, respectively. The equations are written in a form similar to that used in the K-FIX computer code, from which FLUFIX has been developed.[36] Stresses associated with gas and solids viscosities have been deleted; Rivard and Torrey[37] found that, for many applications, these terms are unimportant and significantly increase the computational effort. The conservation equations in the FLUFIX code are solved in conservation-law form in two-dimensional Cartesian and axisymmetric cylindrical coordinates using the Implicit Multifield (IMF) numerical technique.[38] Cartesian coordinates were used in the present computations.

The treatment of the pressure gradient term in the gas and solid phase momentum equations above results in an initial value problem that is ill-posed, as is discussed in detail by Lyczkowski et al.[39] This situation leads to a conditionally stable numerical solution. One way to overcome the problem is to retain a normal component of solid phase stress, τ, sometimes associated with solid phase pressure or particle-to-particle interactions, in the solid phase momentum (Eqs. 2.4 and 2.6).

In addition to increasing stability, the primary computational function of the solids stress term is to keep the bed from compacting below the defluidized or packed-bed state of approximately 0.38-0.4 porosity. Any solids stress model that accomplishes this is adequate. The Rietma and Mutsers data[40] used previously[28-34] was found to be inadequate for cases involving obstacles, because it resulted in overcompaction, and was

modified to overcome this shortcoming. A more subtle function of the solids stress term (gained from computational experience) is that it affects the instantaneous bed interface and bubble shapes and timing.

To place this term in perspective, we must consider the mechanisms of the compaction of powders.[41,42] The motivation for the most generally satisfactory expression is the experimental observation that plotting the logarithm of consolidating pressure versus volume yields a substantially straight line for both metallic and nonmetallic powders undergoing compaction. We used this simple theory to derive a generalized solids elastic modulus coefficient, $G(\varepsilon)$, of the form

$$G(\varepsilon) = G_o \exp\left[-c(\varepsilon - \varepsilon^*)\right] \tag{2.8}$$

where c (the compaction modulus) is the slope of ln G versus ε, and ε^* is the compaction gas volume fraction. The normalized units factor, G_o, has been taken to be 1.0 for convenience. Considerable disagreement exists over the exact form of this relationship. Shimora has summarized 15 different expressions.[42]

Equation 2.8 is a convenient and consistent expression with which to interpret the physical significance of solids pressure data. We have converted the Rietma and Mutsers data,[40] as curve fit by Gidaspow and Ettehadieh;[32] the expression used by Gidaspow and Syamlal for solids-gas critical flow;[43] and the expression we have been using for hydrodynamics and erosion calculations for a fluidized bed containing an obstacle[35] into the form of Eq. 2.8, as shown in Table 1.

In the above analysis, $G(\varepsilon) = 1.0$ Pa when $\varepsilon = \varepsilon^*$. The Rietma and Mutsers model is inappropriate to keep the bed from compacting, because the model was developed for data taken at a much higher compaction porosity (0.62), and the compaction modulus is very low. Porosities below 0.2 have resulted with this model. The Gidaspow and Syamlal model, developed from solids-gas flow data through aerated hoppers, is appropriate at a compaction porosity near minimum fluidization (0.422).[44] The compaction modulus is high because the particles are being compacted as they flow down through the hopper. Our model has a somewhat higher compaction modulus and a lower compaction porosity,

TABLE 1 Solids Elastic Modulus Parameters

Reference	c	ε^*	Model
Lyczkowski, Bouillard, and Gidaspow[35]	600	0.376	1
Gidaspow and Syamlal[43]	500	0.422	2
Rietma and Mutsers[32,40]	20	0.62	3

more appropriate for a packed bed (0.376); this is necessary because of the greater compaction resulting from solids striking the obstacle.

The other major empirical input in this cold bed model is the fluid-particle drag coefficient, β. This coefficient, obtained from standard correlations,[32,33] was used unchanged for calculations involving an obstacle. Below a porosity of 0.8, β is given by the Ergun equation;[45] above 0.8, it is given by Wen and Yu's expression.[46]

2.2 REPRESENTATIVE COMPUTATIONAL RESULTS AND COMPARISONS WITH DATA

The basic configuration being modeled is the same as that in a publication by Gidaspow and Ettehadieh[32] (see Fig. 1). The computational region is 19.685 cm wide (x direction) by 58.44 cm high (y direction). The cell dimensions are $\Delta x = 0.635$ cm and $\Delta y = 4.87$ cm, so that the number of computational cells is 31 in the x-direction and 12 in the y-direction, for a total of 372. In the figure, the numbers in parentheses refer to key cell numbers (I,J). Symmetry about the central jet is assumed; hence, the actual bed width is 39.37 cm. In previous modeling work without an obstacle,[28] symmetry was assumed, and agreement with data was good. The jet half-width is 0.635 cm (one cell width). The jet velocity is 578 cm/s, and the secondary air velocity of 23.36 cm/s maintains the bed without a jet at minimum fluidization. The particle diameter is 503 μm, and the density is 2.61 g/cm^3. The obstacle is placed two nodes above the jet and is two nodes wide by two nodes high (1.27 cm wide by 9.74 cm high). Because the initial bed height is 29.22 cm (six cells high), the obstacle lies completely within the bed. Although this configuration is not typical of FBC geometries, it was selected because (1) it is similar to the model without the obstacle, so that prior experience is relevant; and (2) it serves to further validate the hydrodynamic model.

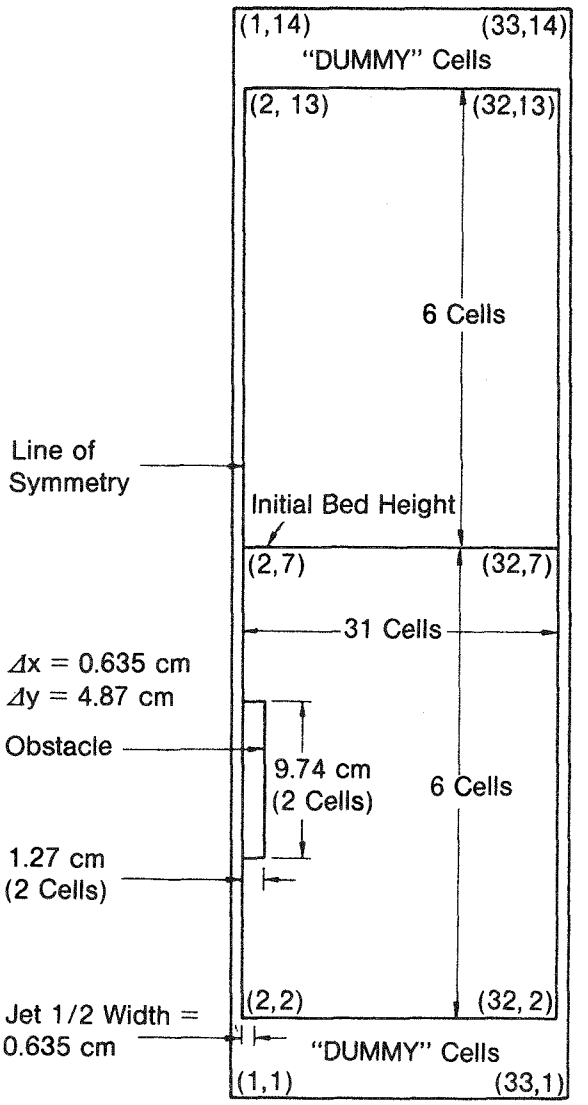

FIGURE 1 FLUFIX Computational Mesh for Coarse Mesh, Showing Obstacle Location

The boundary conditions are described here. At the inlet (J =2), the axial gas velocity is set equal to the experimentally determined minimum-fluidization superficial velocity, 26.0 cm/s. There are no solids entering, hence, the inlet porosity is set to 1.0. The pressures in the dummy cells at the top (J = 14) are set equal to atmospheric pressure (101.3 kPa), and V_s = 0 at the exit (J = 13); that is, wire mesh is simulated to prevent solids carry-over. The pressures in the bottom row of dummy cells (J = 1) are set equal to atmospheric pressure plus 1.2 times the total bed weight (105.5 kPa), to simulate the distributor plate pressure drop measured in the experiment. On all solid surfaces except the inlet, outlet, and line of symmetry, no-slip boundary conditions are used (i.e., normal and tangential velicities for each phase are set equal to zero).

Initially, the lateral gas velocity is zero, the axial gas velocity is equal to the interstitial gas velocity at minimum fluidication, and the solids lateral and axial velocities are zero. The bed porosity is uniform at 0.42. The initial pressure distribution corresponds to the hydrostatic bed height. At time t greater than zero (0^+), the gas flow through the jet into cell (2,2) is increased to 578 cm/s. A fixed time step of 0.1 ms was used. Typical running time on an IBM 3033 computer was about one hour for each second of transient time in the simulation.

The computations were performed before high-speed (800 frames/second) motion pictures were taken of a flow visualization experiment modified to include an obstacle. This experiment is described in Ref. 31. A detailed schematic diagram of the plastic two-dimensional fluidized bed is shown in Fig. 2. Figure 3 shows a still frame from this motion picture at about 0.25 s into the transient (there is an uncertainty of about 0.02 s in the time the jet was turned on), illustrating the formation of the first bubble. The numbers above the white horizontal lines are the bed height in inches. The bed height has increased from its initial value of 29.22 cm (11.5 in.) to 35.6 cm (14 in.) near the bed center and to 33 cm (13 in.) near the bed edge. The bubble height is between 25.4 and 30.5 cm (10-12 in.), and the bubble width is between 5.08 and 10.16 cm (2-4 in.). Figure 4 shows a dot plot representation of the computed porosity distribution at 0.255 s. The dots are distributed randomly throughout each computational cell. The densest shading represents a packed-bed state ($\varepsilon \approx 0.4$), and white represents all gas ($\varepsilon = 1.0$). The right side of Fig. 4 is a contour plot representation of the computed porosity distribution at the same time. Comparing the dot and contour plot representations shows that the perceived edge of the bubble is a contour of porosity, ε, of about 0.7-0.8.

Comparison of Figs. 3 and 4 reveals generally good agreement. The predicted size and location of this first bubble agree well with the experimental results, and the expanded bed height and shape are approximately correct. The slight asymmetries present in the experiment were not accounted for in the model. Hence, the formation of a vortex street above the obstacle (which appears to sweep particles back and forth, keeping them from piling up) is absent, and the computations show a solids buildup.

A computation utilizing a finer mesh was performed to obtain better resolution. The number of computational cells in the x-direction was the same, but the number in the y-direction was increased to 48 (Δy = 1.217 cm). This change makes the cell aspect ratio much closer to unity ($\Delta y/\Delta x$ = 1.92) than is the case for the 31 x 12 node computational mesh ($\Delta y/\Delta x$ = 7.67). The agreement between the 31 x 12 node mesh and the 31 x 48 node mesh computations is good, as can be seen by comparing Figs. 4 and 5.

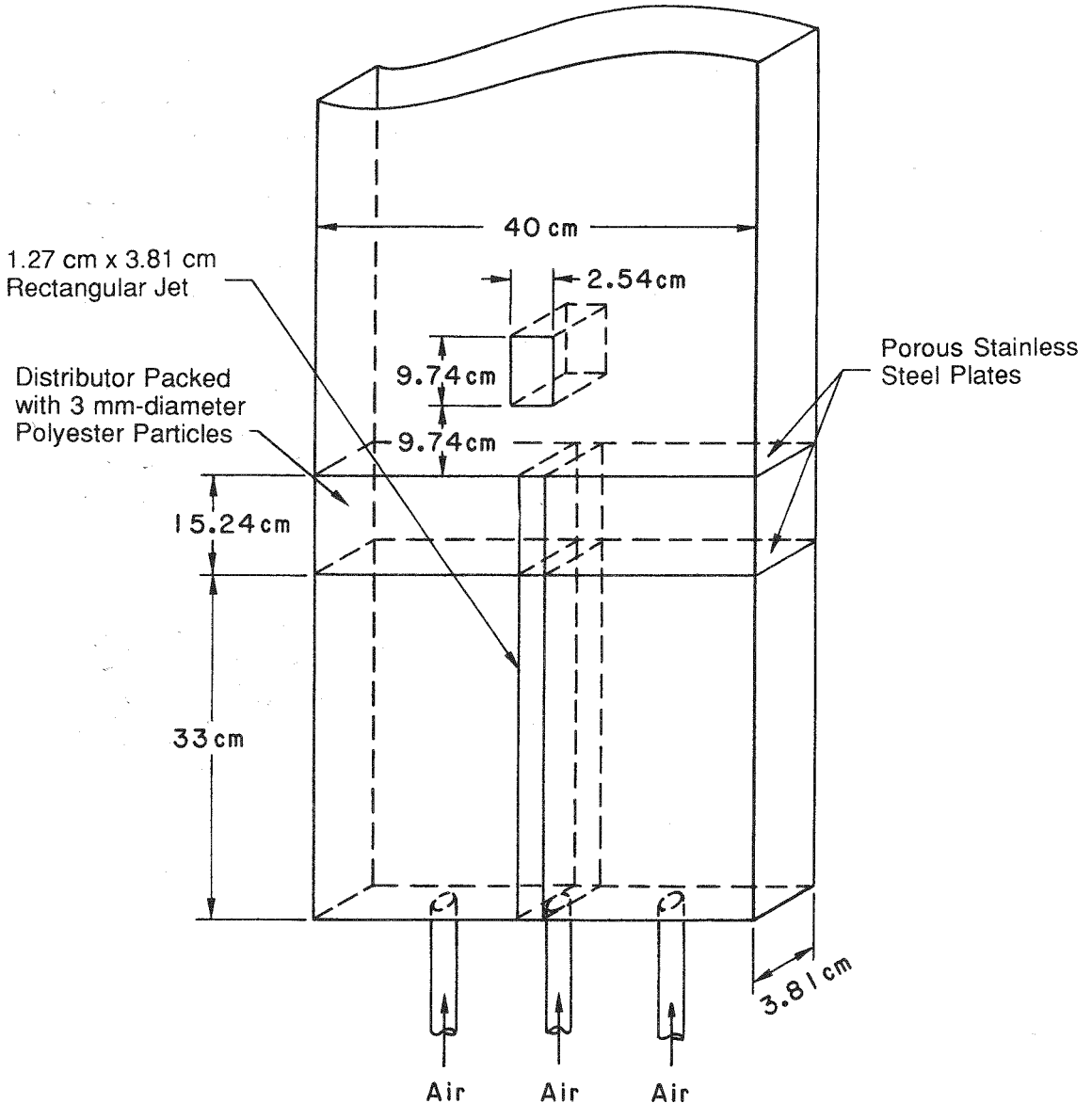

FIGURE 2 Detailed Schematic of the Two-Dimensional Cold Fluidized Bed with a Rectangular Central Jet and Rectangular Obstacle

The expanded bed shape is in better agreement with the experiment and is also sharper, indicating that the bed interface is resolved better with the finer mesh. Fine details, such as the splash of solids against the bottom of the obstacle, are also resolved. The price paid for the finer resolution is considerably longer computing time (approximately 10 times as much as required for the coarser mesh).

The solids velocity and porosity patterns at 0.255 s, plotted in Fig. 7, indicated the existence of a vortex pattern in the wake of the rising bubble near the lower sides of the obstacle. Also revealed is a larger general solids concentration pattern, induced by

the rising bubble. Such solids motions give rise to the erosion of immersed heat exchanger tubes in fluidized-bed combustors.

With the 31 x 48 node mesh, it is possible to resolve the angularity of the bubble bottom. Figure 6 shows a still frame from the high-speed motion picture at about 0.11 s. At this time the bed has barely expanded, and the size of the bubble is significantly less than at 0.25 s, as shown in Fig. 3. The bed height is just over 30.5 cm (12 in.). Figure 7 shows dot and contour plot representations of the computed porosity distributions at 0.13 s. Comparison of Fig. 7 with Fig. 6 reveals good agreement in terms of the bubble size and the angle at the bottom of the bubble. The experimental angle is 42°; the computed angle (solid line in Fig. 7), 36°, does not vary significantly over a ±0.02-s time span. The computed bed expansion is also in good agreement with experiment.

Comparative analysis of a computer-generated motion picture of the contour plot representation of the computed porosity distribution and the high-speed motion picture study reveals good agreement for the frequency of the bubble around the obstacle (~4 Hz) and the higher-frequency, small bubble that forms under the obstacle (~10 Hz). This smaller bubble can be seen under the obstacle in Figs. 3-5.

Figure 8 illustrates the computed porosity fluctuations around the obstacle. Locations 1 and 2 are below the obstacle, locations 3 and 4 are on the side, and locations 5 and 6 are on top of the obstacle. The porosity amplitudes were not measured and, hence, are not validated. We suspect that the computed porosity amplitudes may be somewaht low, because the porosities to not approach 1.0 on the bottom and side of the obstacle after the passage of the first bubble. As can be seen in Fig. 8, the porosity only approaches 0.7-0.85 after the first bubble has passed (after 0.3 s).

Additional studies that modified the form of the hydrodynamic model momentum equations and the solids stress.[47] The conclusion reached is that the computed bubbles do vary, but all are in generally good agreement with the high-speed motion picture study. This agreement implies that the solids flow patterns are also reasonably correct, although they were not measured at this time. Multiple experimental runs should be performed, so that the slightly different bubble patterns that result from random variations in initial conditions from run to run can be averaged out.

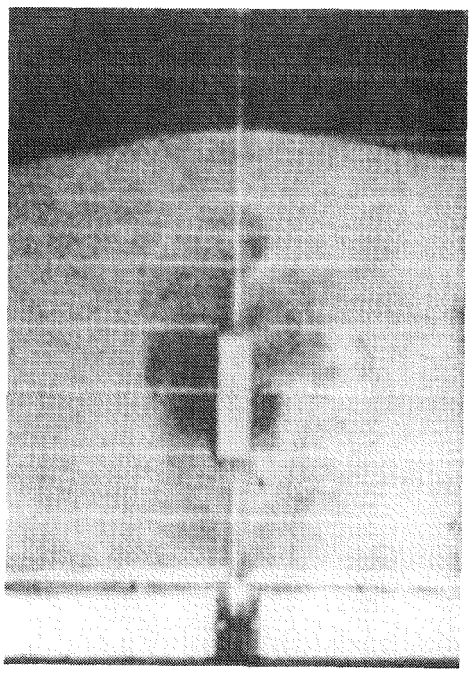

FIGURE 3 High-Speed Motion Picture Still from a Two-Dimensional Flow Visualization Experiment of a Fluidized Bed with an Obstacle, Central Jet, and Secondary Air Flow at Minimum Fluidization (time ≈ 0.25 s)

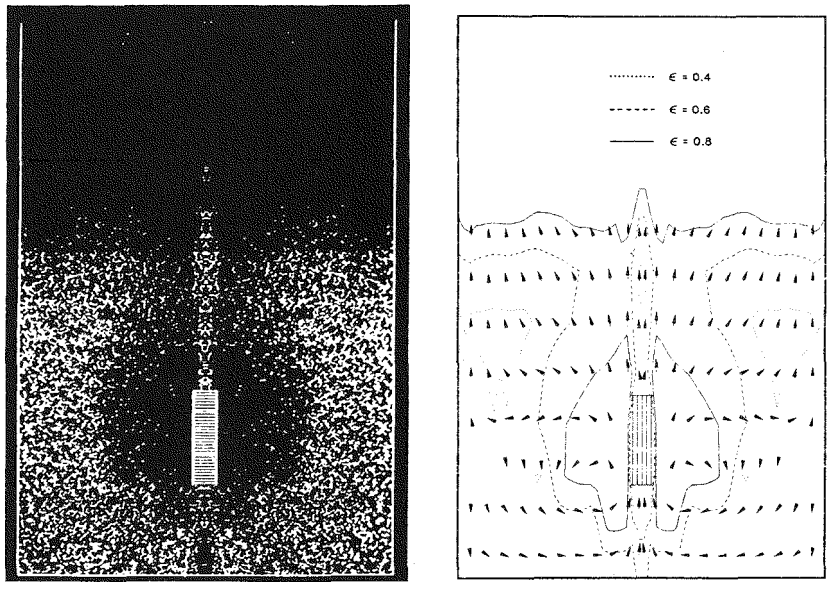

FIGURE 4 Computer-Generated Porosity Distributions for a Two-Dimensional Fluidized Bed with an Obstacle, Central Jet, and Secondary Air at Minimum Fluidization at 0.255 s, 31 x 12 nodes

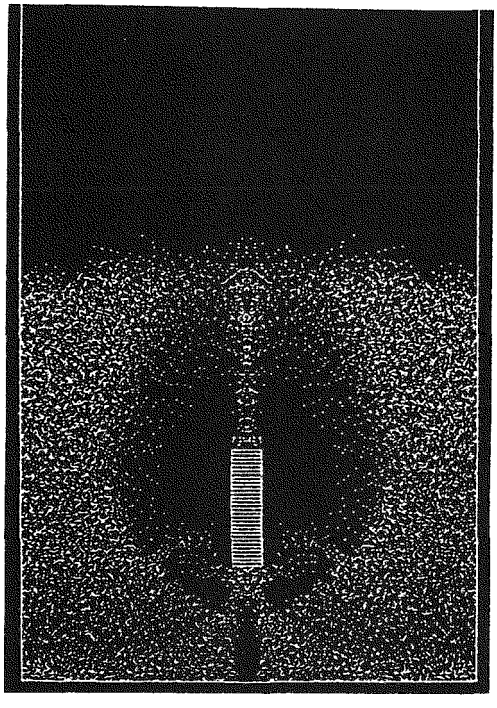

FIGURE 5 Computer-Generated Porosity Distribution for a Two-Dimensional Fluidized Bed with an Obstacle, Central Jet, and Secondary Air Flow at Minimum Fluidization at 0.255 s, 31 x 48 nodes

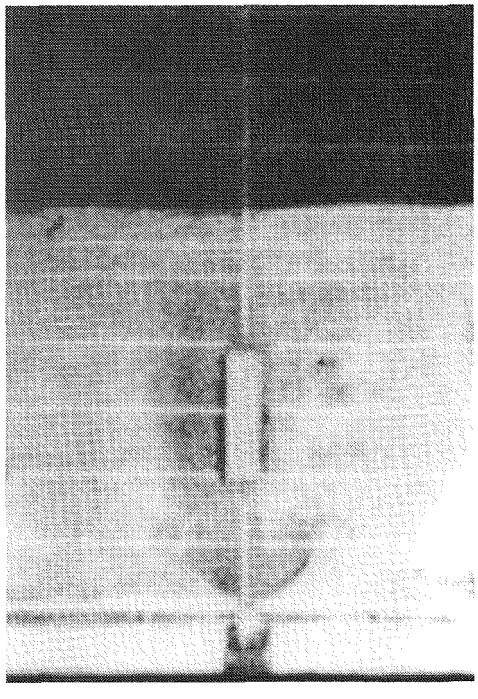

FIGURE 6 High-Speed Motion Picture Still from a Two-Dimensional Flow Visualization Experiment of a Fluidized Bed with an Obstacle, Central Jet, and Secondary Air at Minimum Fluidization (time ≈ 0.105 s)

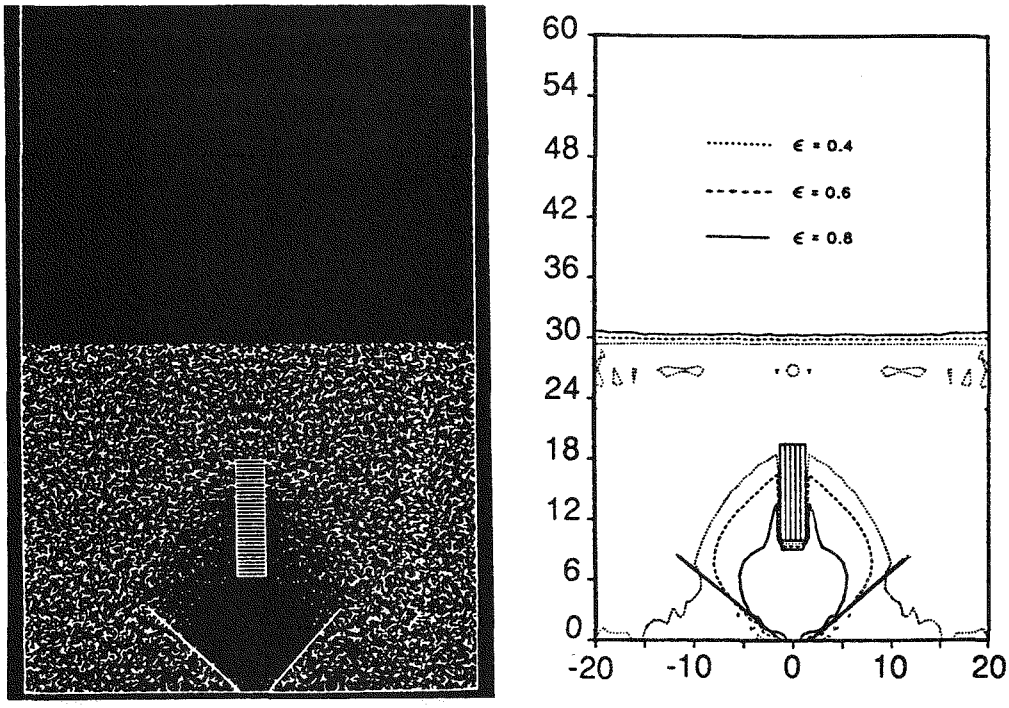

FIGURE 7 Computer-Generated Porosity Distributions for a Two-Dimensional Fluidized Bed with an Obstacle, Central Jet, and Secondary Air at Minimum Fluidization at 0.13 s, 31 x 48 nodes

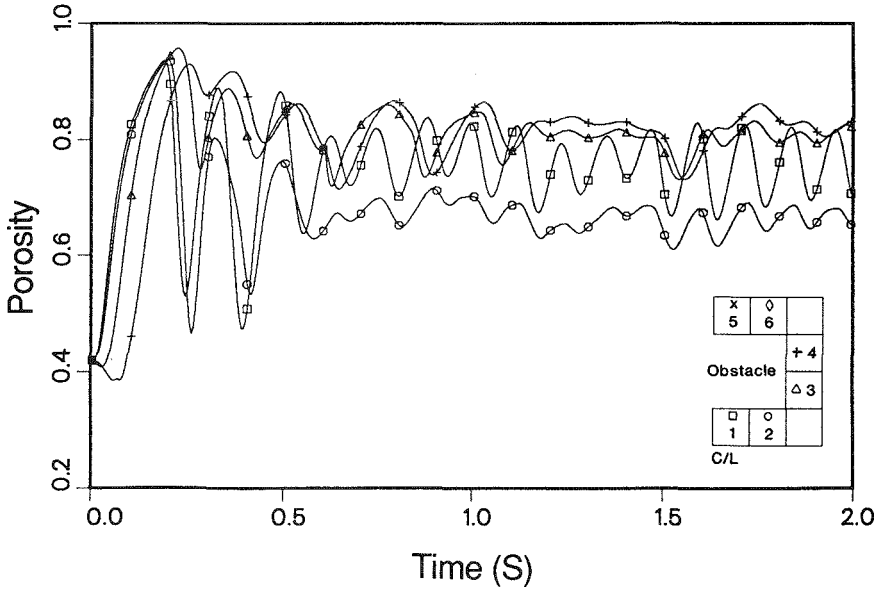

FIGURE 8 Computed Porosity Fluctuations around a Rectangular Obstacle Immersed in a Two-Dimensional Fluidized Bed with a Central Jet and Secondary Air at Minimum Fluidization

As mentioned earlier, it was assumed for the computer simulation that the initial solids velocity is zero, that the bed porosity is uniform at 0.44, and that the gas mass flux corresponds to minimum fluidization conditions. The high-speed motion picture study revealed that very small bubbles were observed to originate from the side of the obstacle before the jet was turned on. This same phenomenon was observed by Loew et al.[18] and Buyevich et al.[48] Buyevich et al., who studied a rectangular obstacle in two-dimensional fixed and fluidized beds, explained the phenomenon of bubble formation as arising from the low gas flow resistance next to the obstacle (due to high local porosity). The resultant excess gas flow, which was measured in a fixed bed to be 5-10 times that in the bulk of the bed, produces the bubbles.

Computations were performed with the central jet off and the secondary air at minimum fluidization. For these computations, symmetry was not assumed. The number of nodes in the transverse direction was increased to 64 (from 33 for the coarse mesh nodalization). The inlet velocity was maintained at 23.36 cm/s. As can be seen in Fig. 9, the results are not quite symmetrical. This asymmetry is probably triggered by perturbations introduced into the uniform flow as a result of asymmetric sweeping through the computational cell during the iteration process. A bubble forms under the obstacle and moves upward, splitting in the process; split bubbles then move up the sides of the obstacle and eventually out of the bed. Examination of the computer-generated motion picture showed that bubbles formed below the obstacle and moved upward at a frequency of approximately 3 Hz. It is clear from Fig. 9 that the fluidized bed was not in a completely uniform initial condition when the jet was turned on. This could explain some differences between the experiment and the calculated results.

The time-averaged porosity distributions were also measured in the two-dimensional fluidized bed that included an obstacle. These distributions are shown in

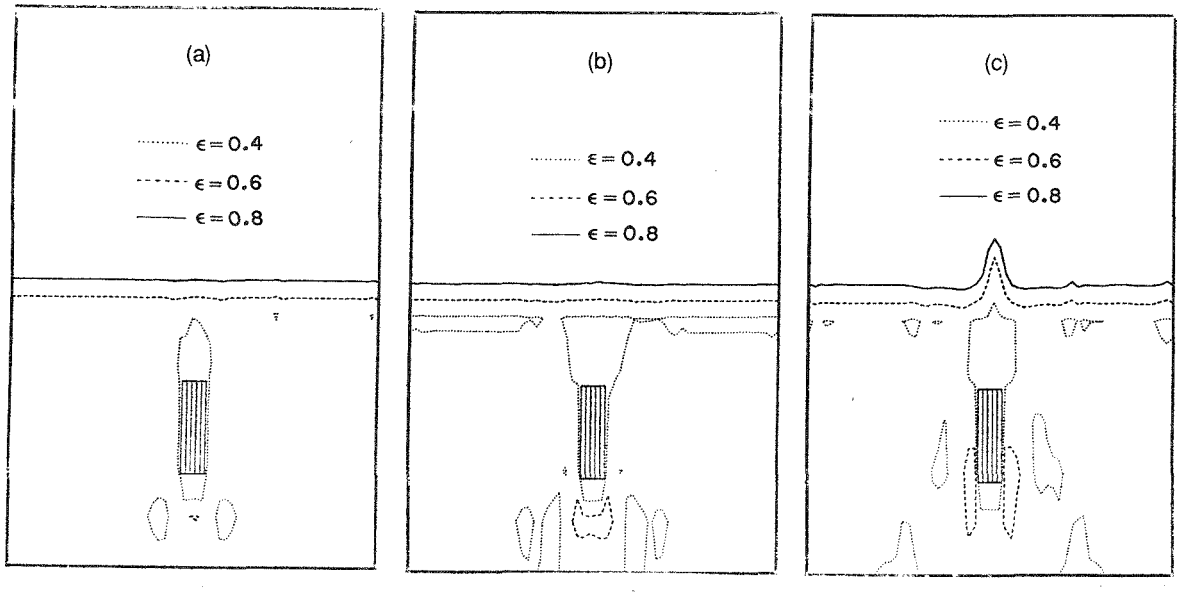

FIGURE 9 Computed Porosity Distribution in a Two-Dimensional Fluidized Bed at Minimum Fluidization with an Immersed Rectangular Obstacle at (a) 0.1 s, (b) 0.2 s, and (c) 0.3 s

Fig. 10, where they are compared with the time-averaged FLUFIX computations using approximately the same scale. The agreement is generally very good; in fact, it is better than that previously reported for the case without an obstacle.[31] The angle and extent of the slumped zone, $\varepsilon = 0.4$, are in reasonable agreement with the experimental results, as are the bed height and shape. The presence of a layer of gas on the side of the obstacle is also predicted; the shape and extent of this layer is in good agreement with the data. The vertical bars on the time-averaged computations are estimated error ranges obtained by time-averaging over different time intervals between 1.5 and 2.5 s.

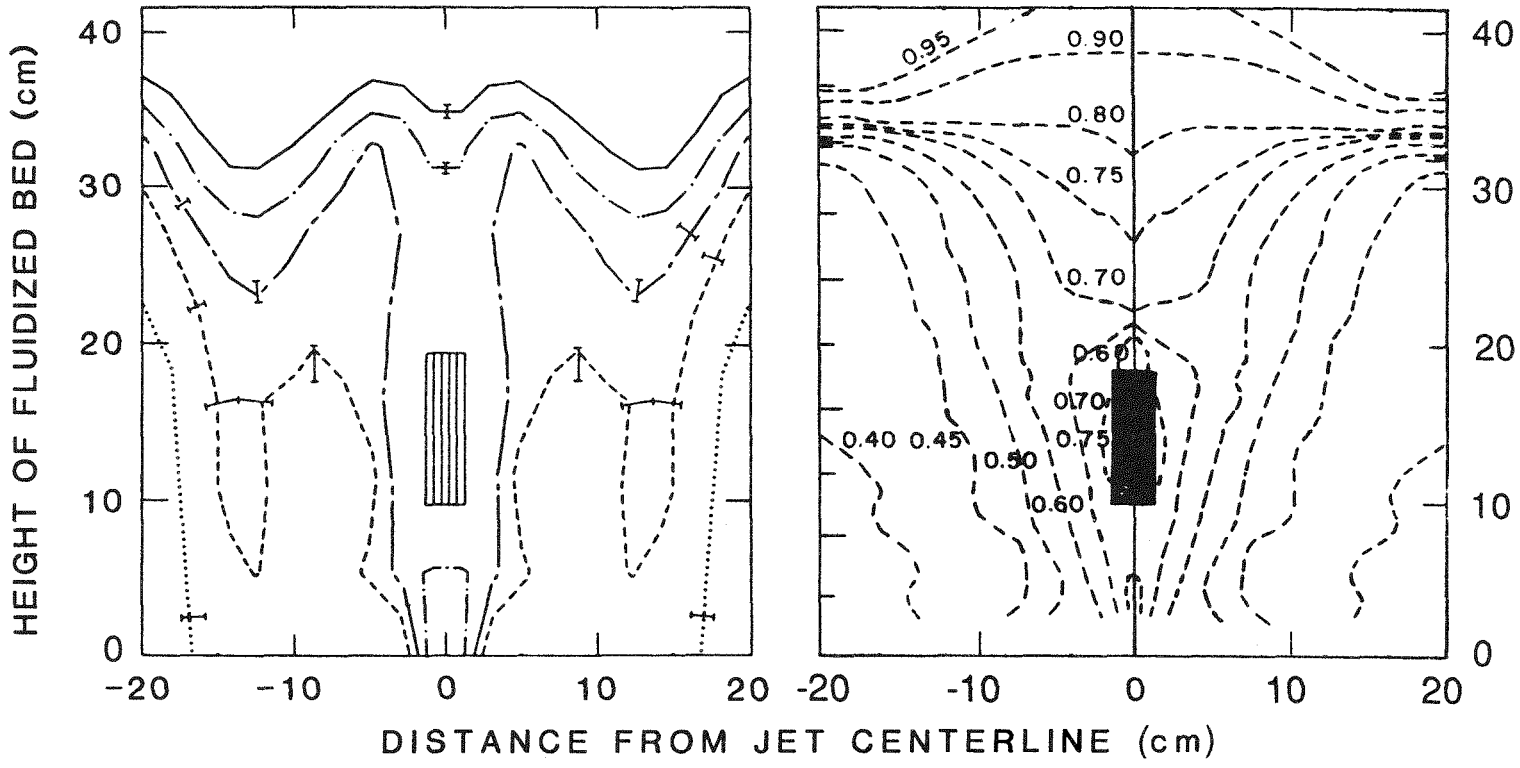

FIGURE 10 Comparison of Experimental (right) and Computed (left) Time-Averaged Porosity Distributions in a Two-Dimensional Fluidized Bed with an Obstacle, Central Jet, and Secondary Air at Minimum Fluidization (I = error range; ε = as indicated: ....., 0.4; - - - -, 0.5; — - — -, 0.6; •-•-, 0.7; ___, 0.8)

3 OVERVIEW OF EROSION MODELING AND MECHANISMS

This section presents an overview of the erosion models that we consider reasonable candidates for inclusion in a preliminary consolidation, i.e., a collection of various types of erosion models that would be driven -- for the first time to our knowledge -- by the types of hydrodynamic fluidized-bed calculations presented in Sec. 2.

The marriage of hydrodynamic and erosion models has been fairly recent. This may account for the general attitude that present-day erosion models do not yet satisfactorily explain erosion patterns in FBCs. To be successful, the fluid mechanics and erosion models must be used together.

The erosion models that form the preliminary consolidation may be organized as follows:

1. Single-particle (dilute phase) models. The consideration for the development of this type of model is the interaction of a single particle with a planar wall. Depending on the model, the wall material is assumed to be removed in (a) a purely ductile mode, (b) a purely brittle mode, or (c) a combination of ductile and brittle modes.

2. Dense phase fluidized-bed models. The consideration for the development of this type of model is the repeated interaction of many particles with the wall. Depending on the model, the wall material is assumed to be removed in (a) a purely ductile mode, (b) a purely brittle mode, or (c) a low-cycle fatigue-failure mode.

3. Power and energy dissipation models. These models are based on the very general consideration of erosion resulting from energy transfer from the solids in a two-phase mixture to the eroding surfaces.

All but the power and energy dissipation models are algebraic in nature.

A detailed literature review of erosion models is not attempted here. Engel has provided a good literature review up to 1976,[49] and Sarkar has provided one up to 1980.[50] Three recent reviews[51-53] deal specifically with erosion in FBCs; two were done at the Morgantown Energy Technology Center (METC), and the third was prepared for METC.

In this report, we summarize the models we have selected from the literature, explain why we selected them, and point out their shortcomings. We also explain why we were led to the more fundamental energy dissipation approach to modeling erosion. Because we cannot claim that this approach will ultimately be more successful than the others, the other models selected for the consolidation are also considered. At this time, most of the calculations have been done with the energy dissipation model, and limited comparisons have been made with the others. Although the results look promising, no

directly appropriate erosion experiments in fluidized beds are as yet available to validate the models. The order-of-magnitude agreement with published erosion rate data, taken at comparable jet and/or superficial fluidizing velocities, provides some basis for guarded optimism. The linking of the models and criteria for their selection are suggested.

3.1 SINGLE-PARTICLE EROSION MODELS

Single-particle erosion models treat the erosion process in terms of the interaction of a single particle with the eroding surface. Such models may be more appropriate for the case of erosion due to dilute solid suspensions, as in pneumatic conveying pipelines and elbows or in turbine blade cascades. In these cases, the particle-particle interactions are negligible, and the erosion process may be thought of as removal of surface material by the cumulative action of the individual particles. In this sense, these models are noncontinuum models.

3.1.1 Finnie's Ductile Erosion Model

According to Engel,[49] Finnie was the first (in 1958) to derive a single-particle erosive cutting model.[54] In 1960, Finnie discussed the assumptions of the model, quoted the results, and compared the results with experimental data.[55] This model set the basic pattern and tone for all single-particle models, so it is discussed here in some detail. The major assumption is that a particle, approaching the eroding surface (or target) at angle α measured from the surface (the impingement angle), will remove material in much the same way as a machine tool would. The particle is assumed to be much harder than the surface and does not break up. The surface material is assumed to deform plastically during the cutting process; hence, the material is ductile. Ductile materials, such as aluminum or structural steel, can develop a relatively large tensile strength before they rupture.

The final expression for the volume of target material, W, removed obtained by Finnie is as follows:[55]

$$W = \begin{cases} c \dfrac{M\vec{V}^2}{\psi p K} \left[\sin(2\alpha) - \dfrac{6}{K} \sin^2(\alpha) \right] & \tan\alpha \leq \dfrac{K}{6} \quad (3.1a) \\ c \dfrac{M\vec{V}^2}{\psi p K} \left[\dfrac{K \cos^2(\alpha)}{6}\right] & \tan\alpha > \dfrac{K}{6} \quad (3.1b) \end{cases}$$

Finnie took K = 2, where K is the ratio of vertical to horizontal (frictional) force,[55] and $\psi = 1$, where ψ is the ratio of the depth of contact to the depth of the cut. The constant c allows for the fact that many particles will not be as effective as the idealized model particle; Finnie arbitrarily took c = 1/2. With M the total mass of abrasive particles, $\vec{V}$ the abrasive-particle velocity, and p the eroding surface "flow stress," W is the total volume of target material removed. To obtain the mass of eroded material removed, W is multiplied by ρ_t, the target density.

The erosion rate (or erosion velocity), $\dot{E}$, is usually given as

$$\dot{E} = \dot{W}/A_t \tag{3.2a}$$

where $\dot{W}$ is the volumetric rate of target material removal, and A_t is the average area of the target. The erosion rate (or erosion velocity) of the target itself, $\dot{E}_t$, is given by

$$\dot{E}_t = -\dot{E} = -\dot{W}/A_t \tag{3.2b}$$

because the volumetric rate of change of the target itself is negative.

In order to apply the Finnie model to compute erosion rates in fluidized beds using FLUFIX-computed hydrodynamic results, Eq. 3.1 must be modified. First, the total particle mass, M, is replaced by the mass flux of solids, $\dot{m}_s = (1 - \varepsilon)\rho_s |\vec{v}_s|$, where $(1 - \varepsilon) = \varepsilon_s$ is the solids volume fraction, ρ_s is the particle density, and $|\vec{v}_s|$ is the magnitude of the velocity of the solid phase. The mass flux, $\dot{m}_s$, is assumed to be positive toward the eroding surface. The particle velocity, $\vec{V}$, is replaced by $\vec{v}_s$ to obtain

$$\dot{E} = \begin{cases} C \dfrac{(1 - \varepsilon)\rho_s |\vec{v}_s| (\vec{v}_s)^2}{p} f(\alpha) & \dot{m}_s > 0 \\ 0 & \dot{m}_s \leq 0 \end{cases} \tag{3.3}$$

where $\dot{E}$ is the erosion rate (in m/s) and $C = c/\psi K$. The erosion rate is positive if the solids velocity vector points toward the eroding surface; otherwise, it is zero.

With K = 2, the angular dependency function $f(\alpha)$ is given by

$$f(\alpha) = \begin{cases} \sin(2\alpha) - 3\sin^2(\alpha) & \alpha \leq 18.43^\circ \quad (3.3a) \\ \cos^2(\alpha)/3 & \alpha > 18.43^\circ \quad (3.3b) \end{cases}$$

Below 18.43°, the surface is cut until the particle leaves the surface; above 18.43°, cutting ceases before the particle leaves the surface. The transition angle given in Eq. 3.3 is close to the angle of maximum erosion, α_{max}, given by Ref. 49 as

$$\alpha_{max} = \frac{1}{2} \tan^{-1}(K/3) \tag{3.3c}$$

With K = 2, $\alpha_{max} = 16.85^\circ$. Equation 3.3 is in the same form as that used by Pourahmadi and Humphrey in their erosion modeling studies.[56] They defined C as the fraction of particles cutting in an idealized manner, consistent with Finnie's 1972 modification of his model.[57] (If one uses Finnie's values of c, ψ, and K, then C = 1/8.)

Pourahmadi and Humphrey[56] used the following expression for f(α):

$$f(\alpha) = \begin{cases} \sin(2\alpha) - 4\sin^2(\alpha) & \alpha \leq 14.04^0 \quad (3.4a) \\ \cos^2(\alpha)/4 & \alpha > 14.04^0 \quad (3.4b) \end{cases}$$

It may be that they used the original Finnie model with K = 1.5, in which case a value of C = 1/6 is obtained. Alternatively, they may have used Finnie's modified model,[57] which accounted for particle inertia, with K = 2; in this case, C = 1/8. The value of C used by Pourahmadi and Humphrey is never mentioned, so either case is possible.

At 18.43°, Finnie's model (K = 2, C = 1/8) yields an erosion rate for ductile target materials given by

$$\dot{E}_{FM} = 0.075 \frac{\dot{m}_s \left(\vec{v}_s\right)^2}{2p} \quad (3.5)$$

which is, in effect, the maximum value. Equation 3.5 predicts that only 7.5% of the particle's kinetic energy goes into erosion for a given hardness, p. The corresponding percentage for Pourahmadi and Humphrey's expression (C = 1/6) is 7.8%. Using Eq. 3.5, Finnie[55] analyzed some data taken for silicon carbide eroding SAE 1020 low carbon steel and found that the value of p exceeded the "true stress at fracture in a tension test" by a factor of almost three. However, if Finnie's 1972 modification of his model (which accounts for particle inertia) is used together with his recommended values of c, ψ, and K, then 5.9% of the particle's kinetic energy would go into erosion, instead of 7.5%.

Erosion models in general, and Finnie's erosion model in particular, cannot be used to calculate absolute erosion rates *a priori*. Finnie's erosion model can be used, together with estimates of target material flow stress (or hardness), to back out a value for parameter C to match the data. On the other hand, if a value for C is assumed, then the value of the flow stress or hardness appropriate for erosion is backed out of the data.

The angular dependence of the erosion rate predicted by using the original Finnie model and its first modifications is quite good up to 45°. Above 45°, the Finnie model underpredicts the erosion rate; at 90°, it predicts no erosion at all, whereas the analyzed data clearly indicate that this prediction is not correct. Further reworking of Finnie's theory did not resolve this problem.[58] The Finnie model also predicts no erosion at 0° (scouring erosion). Shewmon and Sundararajan,[59] who reviewed the literature on erosion in 1983, concluded from scanning electron microscope (SEM) examinations of erosion surfaces that the cutting tool analogy is not valid. They regarded the Finnie model as being of historical interest only and suggested other mechanisms, such as shear localization leading to lip formation and fracture.

3.1.2 Bitter's Combined Ductile and Brittle Erosion Model

The basic assumptions in Bitter's analysis are that deformation and cutting erosion occur simultaneously and that the two effects can be linearly superimposed.[60,61] Thus, Bitter's work extends Finnie's model and corrects it by bringing in the concepts of a threshold erosion rate and energy dissipation. Physically, the impinging particle cannot erode the target material if its impacting velocity is smaller than a threshold velocity, V_{el}.

Brittle Erosion Model

In Bitter's model, the brittle erosion rate is postulated to be equal to the energy dissipation of an elastic sphere deforming the planar target material surface elastically and plastically, divided by an energy (itself dependent on material properties) needed to remove material. This brittle erosion model is given by

$$W_b = \begin{cases} \dfrac{M\,[\vec{V}\sin(\alpha) - V_{el}]^2}{2\varepsilon_b} & \vec{V}\sin(\alpha) > V_{el} \quad (3.6a) \\ 0 & \vec{V}\sin(\alpha) < V_{el} \quad (3.6b) \end{cases}$$

where ε_b is the material-dependent deformation wear factor. The threshold velocity, V_{el}, is the velocity of collision at which the elastic limit of the eroding surface is just reached, given theoretically from the Hertz contact theory[49] by

$$V_{el} = 15.4\,\sigma_y^{5/2}\,\rho_p^{-1/2}\,E_r^{-2} \quad (3.7a)$$

where σ_y is the plastic load limit, ρ_p is the particle density, and E_r is the reduced Young's modulus of elasticity. The value of E_r is given by

$$E_r = \frac{1}{[(1-\gamma_p^2)/(\pi E_p)] + [(1-\gamma_t^2)/(\pi E_t)]} \equiv \frac{1}{(k_p + k_t)} \quad (3.7b)$$

where γ_p and γ_t are the Poisson's ratios, and E_p and E_t are the Young's moduli of elasticity, of the particle and target, respectively. The threshold velocity, V_{el}, which can be computed from Eq. 3.7a, can be determined from particle rebound data using the following relation:[60]

$$V_2 = (2V_1V_{el} - V_{el}^2)^{1/2} \quad (3.8)$$

where V_1 and V_2 are the velocities at the beginning (approach) and end (rebound) of collision, respectively.

Ductile Erosion Model

The portion of Bitter's model devoted to ductile erosion consists of the following:

$$W_d = \begin{cases} \dfrac{2\,MC'\,[\vec{V}\sin(\alpha) - V_{el}]^2}{[\vec{V}\sin(\alpha)]^{1/2}} \\ \quad \times\ \vec{V}\cos(\alpha) - \dfrac{C'\,[\vec{V}\sin(\alpha) - V_{el}]^2}{[\vec{V}\sin(\alpha)]^{1/2}} \quad \phi & \alpha \leq \alpha_o \quad (3.9a) \\ \dfrac{M\,\{\vec{V}^2\cos^2(\alpha) - K_1\,[\vec{V}\sin(\alpha) - V_{el}]^{3/2}\}}{2\phi} & \alpha > \alpha_o \quad (3.9b) \end{cases}$$

where ϕ is the material-dependent cutting wear factor. The constants C' and K_1 are given by[44]

$$C' = 0.288\,(\rho_p/\sigma_y)^{1/4}/\sigma_y \qquad (3.10a)$$

and

$$K_1 = 8.036\,\sigma_y^{\,2}\,E_r^{\,-2}(\sigma_y/\rho_p)^{1/4} \qquad (3.10b)$$

The angle α_o may be estimated from Finnie's model (Eq. 3.1), or by equating Eqs. 3.2b and 3.2c and solving for α. The total erosion rate, W, is then given by the sum of W_b and W_d.

The effect of K_1 is negligible in Eq. 3.9b (where $\alpha > \alpha_o$) and can safely be dropped.[61] If ϕ is associated with $3\psi_p$, then (except for the factor c) Eq. 3.1b (tan $\alpha >$ K/6) of Finnie's erosion model and Eq. 3.9b ($\alpha > \alpha_o$) of Bitter's erosion model are the same.

The interesting features of Bitter's model are that (1) for soft ductile materials, it produces wear curves similar to Finnie's, but with nonzero wear at 90°; and (2) for hard brittle materials, it

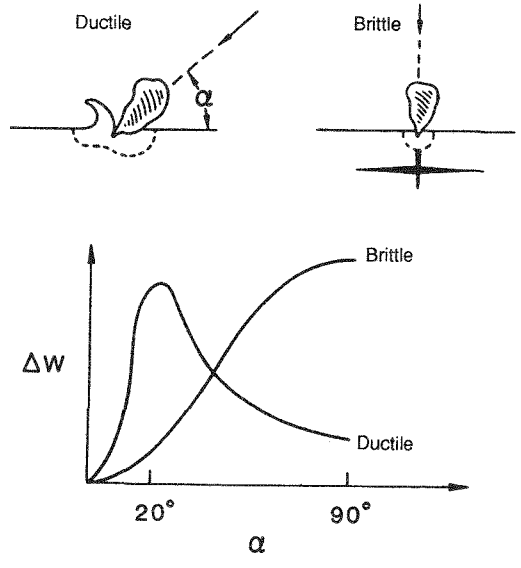

FIGURE 11 Erosion Mechanisms Show Wear Trends as a Function of Impact Angle (α = impingement angle)

produces wear curves that reach a maximum at 90°. The shapes of these curves are shown schematically in Fig. 11.

Bitter's model involves more material properties than Finnie's and includes those of the particle. However, Bitter's model still predicts zero wear at a zero impingement angle. In fact, the erosion rate is zero when $\alpha < \sin^{-1}(V_{el}/|\vec{V}|)$, which is greater than zero. Bitter's model, like Finnie's, also assumes that the particles do not erode. The application of Bitter's model to calculation of wear in fluidized beds, using hydrodynamic results computed by FLUFIX, is essentially the same as that of Finnie's model (see Sec. 3.1.1).

3.1.3 Neilson and Gilchrist's Combined Ductile and Brittle Erosion Model

Neilson and Gilchrist[62] simplified Bitter's combined model by postulating a simplified ductile erosion model while retaining Bitter's brittle erosion model (Eqs. 3.6 and 3.7). The result is given by

$$W = W_d + W_b = \begin{cases} \dfrac{M[\vec{V}^2 \cos^2(\alpha) - V_p^2]}{2\phi} + \dfrac{M[\vec{V}\sin(\alpha) - V_{el}]^2}{2\varepsilon_b} & \alpha < \alpha_o \quad (3.11a) \\ \dfrac{M\vec{V}^2 \cos^2(\alpha)}{2\phi} + \dfrac{M[\vec{V}\sin(\alpha) - V_{el}]^2}{2\varepsilon_b} & \alpha > \alpha_o \quad (3.11b) \end{cases}$$

with the proviso that $W_b = 0$ when $\vec{V}\sin(\alpha) < V_{el}$.

In addition to a threshold velocity normal to the eroding surface, $V_n = V_{el}$, there is a threshold velocity parallel to the eroding surface, V_p, given by

$$V_p^2 = \vec{V}^2 \cos^2(\alpha)[\sin(n\alpha) - 1] \quad (3.12)$$

where n is an empirical constant and $\alpha_o = \pi/2n$. Substitution of Eq. 3.12 into Eq. 3.11a results in

$$W = W_d + W_b = \frac{M\vec{V}^2 \cos^2(\alpha)\sin(n\alpha)}{2\phi} + \frac{M[\vec{V}\sin(\alpha) - V_{el}]^2}{2\varepsilon_b} \qquad \alpha < \alpha_o \quad (3.13)$$

Comparison of the first terms of Eqs. 3.13 and 3.11b with Bitter's ductile erosion model, Eq. 3.9, reveals the extent of the simplification. The first term of Eq. 3.11b is the same as Bitter's ductile erosion model (Eq. 3.9b) with $K_1 = 0$. The second terms of Eqs. 3.13 and 3.11b are the same as Bitter's brittle erosion model, Eq. 3.6.

3.1.4 Sheldon and Finnie's 90° Brittle Erosion Model

Brittle materials, such as ceramics or glass, cannot deform plastically; instead, they crack and fracture when subjected to tensile stress. The angle of maximum erosion for brittle materials is near 90°.

Sheldon and Finnie[63] analyzed brittle erosion occurring at 90°. Their final result for spherical particles is given by

$$W = C_e R_p^{\xi} V^{\eta} \tag{3.14}$$

where:

$$\xi = 3f/(f - 2), \tag{3.15a}$$

$$\eta = 2.4f/(f - 2), \text{ and} \tag{3.15b}$$

$$C_e = E_t^{0.8}\sigma_b^{2} \tag{3.15c}$$

In the above relations, R_p is the particle radius, f is the coefficient of friction, and σ_b is the flexural strength. This model gives velocity exponents of 3.2, 2.72, and 2.66 for f = 8, 16.9, and 20 (glass, graphite, and hardened steel), respectively.

3.2 FLUIDIZED-BED EROSION MODELS

Single-particle erosion models have been the subject of much more research than fluidized-bed erosion models. Only two fluidized-bed erosion models have been found in the literature; they are summarized in this section.

3.2.1 Soo's Ductile and Brittle Erosion Models

Soo[64] extended his treatment of heat transfer and charge transfer by impact to a treatment of material removal in the case of small deviations from elastic impact. Conceptually, Soo's models resemble Bitter's models in that the energy expended to remove material must exceed the yield stress in order for ductile or brittle failure to produce wear. Soo's erosion models treat ductile wear and brittle wear separately.

Ductile Wear

Soo's ductile wear model is expressed in terms of

$$\dot{E}_d = \cos(\alpha)[1 - K_d^{*}\sin(\alpha)^{-1/5}]\rho_p \vec{V}^3 C_d f(1 + r^{*})(2.94)(5/16)\eta_d/\varepsilon_d \tag{3.16}$$

where C_d is a correction factor for nonsphericity ($\simeq 1$); r* is the ratio of rebound to approach velocity, V_2/V_1; ε_d is the energy required to remove a unit volume of ductile material; and η_d is the mechanical efficiency of impact ($\sim 10^{-4}$). (Soo's ε_d plays the same role as that of ϕ in Bitter's ductile erosion model.) The dimensionless resistance parameter, K_d^*, is given by

$$K_d^* = 6\pi^2\sigma_d(k_p k_t)^{1/2}/[2^{2/5} f C_d (1 + r^*)^{1/5} N_{IM}^{1/5}] \tag{3.17a}$$

where N_{IM} is the impact number:

$$N_{IM} = (5\pi^2/2)\rho_p \vec{V}^2 (k_p k_t)^{1/2}[(k_p k_t)^{1/2} + (k_t/k_p)^{1/2}]^4 \tag{3.17b}$$

On the assumption that motion in a fluidized bed is random, Soo averages Eq. 3.16 over all directions and magnitudes to obtain

$$\dot{E}_{dFB} = (1 - 0.9586\ \bar{K}_d^*)\rho_p(\bar{V}^2)^{3/2} C_d \bar{f}(1 + \bar{r}^*) \tag{3.18}$$
$$(2.94)(5/16)[2/(3\sqrt{\pi})]\ \eta_d/\varepsilon_d$$

where the overscore, $\bar{}$, denotes averaging. This erosion rate is no longer a function of angle, and $\bar{V}^2$ (the intensity of random motion) replaces $\vec{V}^2$ in the impaction number, Eq. 3.17b. Because a fluidized bed is not truly random, Eq. 3.16 may be preferred over Eq. 3.18.

Brittle Wear

Soo's brittle wear model is expressed in terms of

$$\dot{E}_b = \sin(\alpha)[1 - K_b^*(\sin(\alpha)^{-1/5}]\rho_p V^3 C_b (1 + r^*)(2.94)(5/16)\eta_b/\varepsilon_b \tag{3.19}$$

where C_b, ε_b, and η_b are the analogous terms for C_d, ε_d, and η_d in the ductile erosion model and K_b^* is given by

$$K_b^* = 6\pi^2\sigma_b(k_p k_t)^{1/2}/[2^{2/5} C_b (1 + r^*)^{1/5}\ N_{IM}^{1/5}] \tag{3.20}$$

By averaging over all directions and magnitudes, as in the ductile erosion model, Soo obtains the following fluidized-bed brittle erosion model:

$$\dot{E}_{bFB} = (1 - 0.8981\ \bar{K}_B^*)\rho_p(\bar{V}^2)^{3/2}C_b(1 + \bar{r}^*)$$
$$(2.94)(5/16)[2/(3\sqrt{\pi})]\eta_B/\varepsilon_B \qquad (3.21)$$

Clearly, Soo's erosion models resemble those that have been discussed previously. However, there are differences in the details of the exact angular dependence and the way in which the material properties enter.

Results from Soo's erosion models have not been compared with experimental data. Soo estimates that, in the case of 700-μm dolomite particles wearing 316 stainless steel, $1 - K_d^* \simeq 10^{-2}$, $f \simeq 0.1$, and $\eta_d C_d \simeq 10^{-4}$. Assuming that $1 + r^* \simeq 1$, the ductile erosion estimated using Soo's model (Eq. 3.18) is as follows:

$$\dot{E}_{dFB} = \frac{0.69 \times 10^{-7}\rho_p(\bar{V}^2)^{3/2}}{2\varepsilon_d} \qquad (3.22)$$

This result is five orders of magnitude lower than $\dot{E}_{FM}$, the maximum erosion rate given by Finnie's model (Eq. 3.5). Models of ductile erosion of tubes in FBCs are probably more appropriate than brittle erosion models.

Soo's model can be used with FLUFIX-computed hydrodynamic results by replacing ρ_p with $(1 - \varepsilon)\rho_s$ and $\vec{V}^3$ with $|\vec{v}_s|(\vec{v}_s)^2$.

3.2.2 Wood and Woodford's Fatigue Erosion Model

From their studies of tube erosion in fluidized beds, Wood and Woodford[65] concluded that damage is not a cutting phenomenon but is more like a local fatigue phenomenon. In basic studies of abrasion,[66] a similar mechanism has been identified.

The starting point of Wood and Woodford's model is Hutching's model[67] involving constant indentation pressure acting on a rigid particle, impacting a plastically deforming material that has no elastic recovery. The Wood and Woodford model is given by

$$\dot{E} = \frac{\beta M_p}{N_f P}\frac{\dot{N}}{A}\frac{U_p^2}{2} \qquad (3.23)$$

where β is a fraction of the indented volume, V; M_p and U_p are the mass and velocity of the particle, respectively; N_f is the number of cycles to fatigue failure; and $\dot{N}/A$ is the impact rate per unit area. This impact rate is given by

$$\frac{\dot{N}}{A} = \frac{1}{2}\,\frac{6(1-\varepsilon)}{\pi d_p^3}\,U_p \tag{3.24}$$

where d_p is the particle diameter. According to Wood and Woodford, the factor of 1/2 in Eq. 3.24 accounts approximately for the fact that the expected impact velocity is a fraction of the mean velocity of all particles. As in Hutchings' model, the pressure, p, could be given by $p = C\sigma_y$, where σ_y is the uniaxial yield stress. Because particle velocities were not measured in the Wood and Woodford study, they used a simple (and possibly incorrect) model for the solids velocity and generated curves of normalized erosion rates, $\dot{E}/[\beta/N_f p]$.

In order to justify their model, Wood and Woodford assumed the Coffin-Manson equation:

$$N_f = \left(\frac{\varepsilon_f}{2\Delta\varepsilon_p}\right)^2 \tag{3.25}$$

where ε_f is the tensile stress at failure and $\Delta\varepsilon_p$ is the plastic strain range. They set $\varepsilon_f/\Delta\varepsilon_p = 1$ and $\beta = 1$. They then substituted for p from

$$p = \frac{1}{2}\,M_p U_p^2/V_c \tag{3.26}$$

where V_c is the crater volume used to obtain the specific erosion rate, S, equal to the ratio of mass loss per unit area, $\dot{m}/A$, to mass flux of incident particles, $M_p\dot{N}/A$:

$$S = \frac{\dot{m}/A}{M_p\dot{N}/A} = \frac{\dot{E}\rho_t}{M_p\dot{N}/A} = \frac{4\rho_t V_c}{M_p} \tag{3.27}$$

Then they calculated V_c from an independent experiment,[68] in which they observed a crater diameter, d, of 6.4 μm for 1.9-mm silica sand eroding A286 steel as:

$$V_c = \left(\frac{\pi}{48}\right)d^3\left(\frac{d}{d_p}\right) \tag{3.28}$$

or 6×10^{-20} m^3 for 15×10^{-6} kg of particles. Using $\rho_t = 8.2 \times 10^3$ kg/m^3, Eq. 3.27 yields 1.3×10^{-10}. This value is on the same order of magnitude as the measured specific erosion rate (deduced from independent measurement of $\dot{N} = 500\ s^{-1}$):

$$S_{exp} = \frac{1.3 \times 10^{-12}}{500 \times 15 \times 10^{-6}} = 2 \times 10^{-10} \tag{3.29}$$

4 PREVIOUS EFFORTS TO COUPLE FLUID MECHANICS AND EROSION MODELS

The three major categories of single-particle erosion models discussed in Sec. 3 -- ductile (cutting), brittle (deformation), and fatigue (repeated low-frequency particle-surface interaction) -- all establish a relationship between the erosion rate and the particle kinetic energy. Beyond this similarity the models in different categories differ in terms of the detailed relationships (involving material properties) that enter into the erosion models' use of all or a portion of the kinetic energy of the particles.

Portions of other models may be useful in modifying or extending the single-particle models, as well as the power and energy dissipation models discussed in Sec. 5. This is particularly true in regard to material properties and relationships between them and the particle energy. For example, under certain circumstances particle impact and rebound velocity data may be used to estimate the portion of the particle's kinetic energy transferred to the surface; which, in turn, determines the material removal.[69,70] Such information is needed directly in several of the models.

The major shortcoming of all the models discussed thus far is that they incorporate the macroscopic or nominal fluid mechanical properties of particle velocity and impact angle, rather than local (or differential) properties. They also fail to account directly for particle fragmentation (or attrition) and concentration of particles in the fluid stream. Finnie stated in 1972[57] that no satisfactory explanation of concentration dependence existed, and that very little had been published concerning the effect of the carrier fluid itself.

Knowing that the local erosion depends mostly on the local velocity, Wolak et al.[71] measured the velocities of 60-mesh (250-μm) SiC particles exiting nozzles located at various distnaces from a planar target for different loading ratios. They found that (1) the particles accelerated as they left the nozzle, (2) the particles reached a maximum velocity some distance from the nozzle, and (3) the particle velocity also varied in the radial direction. The implication is that the macroscopic erosion models may predict erosion patterns incorrectly because of local variations in the particle energy.

Using dimensional analysis, Tsai et al.[72] identified seven dimensionless groups, listed in Table 2, considered to be important in excessive wear. Several of the groups include information about fluid mechanical variables, such as the boundary layer thickness, δ; carrier fluid viscosity, μ_f; concentration of particles, c_p; and relative velocity between particles and carrier fluid, v_r. None of these variables is included in the erosion models discussed in Sec. 3.

The last group in Table 2 accounts explicitly for the hardness of the particles. Tsai et al. found that, over a fairly wide range of variables, the overall dependence of the erosive wear on the particle and erodent material hardness is approximately $S_p^{1/2}/S_s$ for slurries. The dependence on particle hardness appears to disappear when $S_p > S_s$ (Ref. 49, p. 105).

TABLE 2 Fluid-Mechanical Parameters Important in Erosion

Term	Name	Definition
$d_p\rho_f V_r/\mu_f$	Particle Reynolds number	Relative measure of inertial-to-viscous effects for the particles in suspension
δ/d_p	"Impact-cushioning" number	Argued to be a measure of the extent to which viscous effects cushion particle impact on the eroded surface
ρ_p/ρ_f	"Particle inertia" number	Relative measure of particle phase to fluid phase density (characterizes relative inertial effects of the two phases)
V_r/V_p	"Slip" number	Ratio of relative particle velocities (characterizes slip velocity effects)
c_p/ρ_p	"Energy dilution" number	Argued to be a measure of the extent to which the fluid phase dilutes the kinetic energy content of the particle phase in suspension
$\rho_t/\rho_p V_p^2$	"Barrier" number	Relative measure of the energy barrier that suspended particles must overcome on impact to create conditions that are propitious for erosion
ρ_p/ρ_t	"Disorder" number	Postulated as an indication of the tendency for erosion to occur on the impact of a particle with sufficient energy to cause erosion

Source: Ref. 72.

The use of purely empirical erosion correlations (such as those in Ref. 72) is not recommended, because they may be highly system-dependent. We believe that a more fruitful avenue is to couple the fluid mechanics with erosion models used locally.

4.1 EROSION IN TURBOMACHINERY

The coupling between fluid mechanics (also termed hydrodynamic modeling) and erosion modeling is fairly recent and coincides closely with the increasing interest in burning coal to reduce the U.S. dependence on imported oil. Long before the FBC

erosion issue developed (see Sec. 1.2), erosion problems were encountered in turbomachinery components. The success achieved in coupling fluid mechanics and erosion models to predict erosion in this and other areas is described in this section.

Tabakoff and coworkers at the University of Cincinnati have been engaged in turbine blade erosion and particulate flow research since 1971.[70,73-75] It is their hope that the incorporation of erosion into the engine design as a parameter could lead to the production of an erosion-tolerant engine. They have developed a steady-state computer program capable of describing three-dimensional particle trajectories through turbo-axial or radially rotating turbomachinery. Tabakoff has reviewed this group's work up to 1982.[70]

In his review of the erosion literature, Tabakoff concluded

> ...that in the investigation of erosion there have been three predominant approaches taken. The first method involves making assumptions about the erosive process and the introduction of parameters which make the proposed theory conform to experimental results. The second method is one in which the dynamic forces acting between the particle and the material surface are considered, along with well-known material properties. In this scheme assumptions are made as to the condition of the material during the impacts. The third method is to assume that there is no common material property that can be used to describe erosion. In this method a hypothetical erosion resistance property is invented and different materials are related by this property.

The group's own experimental data on the coefficient of restitution (the ratio of rebound to approach velocities) and the ratio of rebound to impingement angle are obtained experimentally by use of high-speed photography or laser doppler anemometry and are expressed in terms of impingement angle. In the computer model first developed in 1973-1974, these ratios are used to account for momentum loss of the particles caused by collision with the turbine blades or channel walls in the Lagrangian trajectory calculations.[73,74]

The major force on the particles is given by a drag expression similar to the one used in the FLUFIX code. The added mass, Basset, and Bagnold forces on the particles are neglected. The compressible, nonviscous, steady-state gas phase momentum equations are assumed to be unaffected by the particles. This implies low particle loadings, an assumption that allows the use of existing single-phase computer codes for turbomachinery. The three-dimensional Eulerian gas flow and Lagrangian particle trajectory equations are solved on a square grid with the coordinates fixed on the rotating blade, (one row of blades is solved at a time).

This same group has also simulated erosion with a Monte Carlo technique.[75] The erosion model used to compute the erosion rates also incorporates the particle rebound data; it is given by a semi-empirical equation that relates the mass of material removed (in mg) to the mass of particles (in g), as follows:

$$S = K_1 f(\alpha)\vec{V}^2 \cos^2\alpha(1 - R_T^2) + K_3(\vec{V} \sin \alpha)^4 \quad (4.1)$$

where:

$$R_T = 1 - 0.0016\ \vec{V} \sin \alpha \quad (4.2a)$$

and

$$f(\alpha) = \begin{cases} 1 + K_{12} \sin [(90/\alpha_o)\alpha] & 0 < \alpha < 2\alpha_o \quad (4.2b) \\ 1 & \alpha > 2\alpha_o \quad (4.2c) \end{cases}$$

where α_o is the angle corresponding to maximum erosion. The parameters α_o, K_1, K_{12}, and K_3 are material-dependent empirical constants. Comparison of Eq. 4.1 with Eq. 3.11 shows that this model is a variant of Neilson and Gilchrist's combined ductile and brittle erosion model. The approach velocity, $\vec{V}$, and impact angle, α, are computed from the particle trajectory computer program.

Private discussions with J. Stringer of the Electric Power Research Institute (EPRI) indicate that Tabakoff's methodology for predicting erosion was considered for FBC applications.[76] Because the particle loading is so much higher in an FBC than in turbomachinery, the particle trajectory calculations would have to include particle-particle interactions and erosion simulation using the Monte Carlo technique; these calculations would be very time-consuming, even if they were valid. In addition, the gas phase fluid mechanics code would not be appropriate, because the effect of the particles on the gas would be significant.

4.2 EROSION IN HORIZONTAL TUBES

Sheldon, Maji, and Crowe[77] developed a numerical method to predict erosion on a horizontal, round tube wall. Is is known as particle-source-in-cell (PSI-Cell),[78] in which the particles are treated as sources of mass, momentum, and energy in the gas phase. The momentum equations for the incompressible, two-dimensional viscous Eulerian gas phase include a momentum sink term due to particle drag and, thus would appear to be an improvement over Tabakoff's equation; however, the former do not contain the void fraction as a variable. Hence, the assumption of low particle loadings is again implicit, and the approach is similar to the "dusty gas" model of Rudinger and Chang.[79] The Eulerian gas flow equations and Lagrangian particle trajectory equations are solved iteratively, using an extension of the TEACH program developed at Imperial College, London.[80] Included in the PSI-Cell technique is a two-parameter turbulence model and heat transfer; but it appears that they were not used in this erosion prediction.

The particle trajectory calculations use empirical rebound angle and coefficient of restitution data in a manner similar to that of Tabakoff.[70] The erosion model is very simple and is given by

$$\left(\frac{\text{mass removed}}{\text{mass abrasive}}\right) \simeq f(\alpha)V^{2.35} \tag{4.3}$$

where $f(\alpha)$ is given by an experimental curve. The exponent of the particle velocity is taken from Sheldon and Finnie's 90° brittle erosion model.[63] The erosion curve for $f(\alpha)$ was determined for impingement angles as low as 4° by using hardened steel shot (Ro45) of 270-μm average diameter striking 6061-T6 aluminum alloy, a ductile material. The rebound data were obtained from multiple flash exposures of 3.175-mm ball bearings striking the same aluminum alloy. Erosion data taken by blasting the steel shot through a horizontal tube 4.95 mm in diameter and 30.5 cm long, made of the same aluminum alloy, were in reasonable agreement, considering that the majority of particles were incident at less than 5° (probably deduced from the trajectory computations), which corresponds to almost pure abrasion (scouring). Whether a coefficient of proportionality was introduced into Eq. 4.3 is uncertain.

4.3 EROSION IN CURVED ELBOWS

In 1983, Pourahmadi and Humphrey[56] published a more sophisticated steady-state, two-dimensional hydrodynamic model to predict erosive wear in straight channels and curved ducts. In that article, the dilute particle loading assumption is again made but, this time, the particle momentum equation is formulated following the Eulerian approach (treating the particles as a continuum). Thus, the void fraction becomes an explicit variable in this model. The standard two-parameter turbulence model is used for the turbulent viscosity of the gas phase. A turbulent-particle diffusion correlation is used, as well as a single-parameter turbulent-particle viscosity model. Stokes's drag law is employed in both the gas and particle momentum equations. Both phases are assumed to be two-dimensional, steady-state, incompressible, and isothermal. The solution procedure is also given by an extension of the TEACH code.[80]

The erosion model used is given by the single-particle Finnie model, expressed by Eq. 3.2a, with $f(\alpha)$ given by Eq. 3.4. The flow pressure, p, is replaced by the Vickers hardness. The square-cross-section, curved perspex-plastic-duct erosion experiments of Mason and Smith[81] were analyzed for two cases: radius of curvature to channel widths of 5 (strong curvature) and 12 (mild curvature). The particles used were 55-μm alumina. Although the relative erosion pattern predictions of $\dot{E}/\dot{E}_{max}$, where $\dot{E}_{max}$ is the maximum erosion rate, were in generally good agreement, the absolute magnitudes of $\dot{E}$ were described as inaccurate by Pourahmadi and Humphrey.[56] They admitted that the very low values of erosion that were measured experimentally had been predicted as higher by their model. However, they believed that the relative comparisons did have value for design purposes and that the model is useful for understanding the controlling parameters. The factor c in the erosion model, described as the "fraction of particles cutting in an idealized manner," is never quantified, nor is the Vickers hardness of perspex plastic.

5 POWER AND ENERGY DISSIPATION EROSION MODELS

The origins, derivation, and numerical implementation of the power dissipation and energy dissipation erosion models are described in this section. We show that the conceptual bases for this approach can be traced back to empirical laws of size reduction, grinding and comminution. We attempt to unify the concepts of ductile, brittle, abrasive, and impaction erosion. The power dissipation model is shown to be a special case of what we call the energy dissipation model.

5.1 POWER DISSIPATION EROSION MODEL

The concept that energy dissipation of the particles impinging on a surface gives rise to deformation wear was postulated as long ago as 1963 by Bitter.[60] It was, however, the slurry erosion literature that provided us with the beginning point of the energy dissipation model.[82] Because the angle of approach of the particles eroding a slurry pipeline is essentially zero, none of the models described thus far appeared to be useful. Therefore, a new model -- termed the power dissipation model -- was developed.

5.1.1 Motivation and Origins

The particle grinding (comminution) and abrasive erosion models provide the genesis of the so-called power energy dissipation erosion model. As long ago as 1885, Kick[83] postulated that the energy, U, required to fracture particles in ball mills is directly proportional to the particle volume and independent of the number and size of the particles. This postulate, known as Kick's law, can be expressed as

$$U = K_1 V_p \tag{5.1}$$

where V_p is the volume of particles being ground in the ball mill and K_1 is a constant of proportionality having units of pressure.[84]

Rabinowicz's much later expression[66,85] for two-body abrasive (sandpaper or scouring) erosion of a surface by particles is given as

$$\frac{V_t}{L} = kF/(3\ H) \tag{5.2}$$

where V_t is the volume of target removed, L is the distance traveled by the particle, F is the applied load (force), H is the hardness of the surface, and k is a dimensionless adjustable constant (sometimes called the abrasive wear coefficient[66]) related to the average angularity of the abrasive particles. The equivalence of Eqs. 5.1 and 5.2 is easily seen by rewriting them in terms of V_p and V_t:

$$V_p = U/K_1 \tag{5.3a}$$

and

$$V_t = kFL/(3\ H) \tag{5.3b}$$

The factor of 3 in Eq. 5.3b relates the yield strength, σ_b, to hardness, H, by $\sigma_y = 3$ H. FL is an energy (force times distance). Comparison of Eqs. 5.3a and 5.3b reveals that FL is equivalent to U, K_1 is equivalent to (3/k)H, and V_t is equivalent to V_p. Thus, the two seemingly dissimilar processes of grinding of particles in ball mills and abrasive wear of a surface by particles are describable by the same relationship.

In their high-speed-photography slurry studies, Shook et al.[86] observed that the particle motion was parallel to the pipe wall in the region of high concentration where the erosion rates were high. Hence, the simple Rabinowicz abrasion relationship holds. A heuristic generalization of this relationship is made in order to compute the volumetric loss-per-unit-time per unit area, $\dot{E}$, caused by the flow of a slurry. Using Eq. 5.3b, $\dot{E}$ is given by the following for a constant applied force, F:

$$\dot{E} = \dot{V}_t/A_t = kF\dot{L}/(3A_tH) \tag{5.4a}$$

where $\dot{V}_t$ plays the same role as $\dot{W}$ in Sec. 3.1.1. The time rate of change of length, $\dot{L}$, is replaced by the velocity of the solids, $\vec{v}_s$, and the applied load, F, is replaced by the force of the solids on the material surface, $\vec{F}_s$, to obtain

$$\dot{E} = \dot{V}_t/A_t = C\vec{F}_s \cdot \vec{v}_s/(A_tH) \tag{5.4b}$$

where C is a factor that includes k/3 (to account for the fact that not all the volume V_t is removed).[66] The force of the particles on the surface can be computed from

$$\vec{F}_s = -(1-\varepsilon)\rho_s \frac{d\vec{v}_s}{dt^s} V_f = -(1-\varepsilon)\rho_s \left(\frac{\partial \vec{v}_s}{\partial t} + \vec{v}_s \cdot \nabla \vec{v}_s\right) V_f \tag{5.5}$$

where V_f is the volume of the fluid and d/dt^s is the total derivative following the solids. Combining Eqs. 5.4b and 5.5, one obtains

$$\dot{E} = -C\ (1-\varepsilon)\rho_s \frac{d\vec{v}_s}{dt^s} \cdot \vec{v}_s \left(\frac{V_f}{A_t}\right)/H \tag{5.6}$$

Equation 5.6 is the basic form of the "power dissipation" erosion model proposed in 1984 by Ushimaru et al.[82] The factor C was not explicitly noted but was used, as will be discussed at a further print. Ushimaru et al. used a "layer thickness" Δ, which can be associated with V_f/A_t. Defining the particle flux to be $\vec{q}_s = (1 - \varepsilon)\rho_s \vec{v}_s \Delta$, the power dissipation, P, can be defined as follows:[82]

$$P = \frac{d\vec{v}_s}{dt} \cdot \vec{q}_s \tag{5.7}$$

Replacing the hardness, H, by a "specific energy," E_{sp}, the erosion rate for the power dissipation model, $\dot{E}_{PD}$, becomes

$$\dot{E}_{PD} = -CP/E_{sp} = -C \frac{d\vec{v}_s}{dt^s} \cdot \vec{q}_s/E_{sp} \tag{5.8}$$

$\dot{E}_{PD}$ is positive, because the particles must decelerate in order for the force of the solids on the surface, $\vec{F}_s$, to be positive (Eq. 5.5). The sign differs from that of Ushimaru et al.,[82] because they obviously considered their symbol, e, for the erosion rate to stand for $\dot{E}_t = -\dot{E}$, the erosion rate of the target itself.

Equation 5.6 states that the erosion rate is given by the total differential of the particle kinetic energy, multiplied by the mass flow of particles and divided by some material property resembling or related to hardness. Hence, we will write Eq. 5.6 symbolically as follows:

$$\dot{E}_{PD} = - \frac{C}{E_{sp}} \left(\frac{dKE_{sPD}}{dt}\right) \left(\frac{V_f}{A_t}\right) \tag{5.9}$$

where the kinetic energy dissipation of the solids is defined as

$$\frac{dKE_{sPD}}{dt} = (1 - \varepsilon)\rho_s \vec{v}_s \cdot \frac{\partial \vec{v}_s}{\partial t} + \left(\vec{v}_s \cdot \nabla \vec{v}_s\right) \tag{5.10a}$$

An alternative derivation, based on thermodynamic considerations, relates the kinetic energy dissipation to the eroding target material pressure, P_t, through

$$\frac{dKE_{sPD}}{dt} \cdot V_f = P_t \frac{dV_s}{dt} = P_t A_t \dot{E}_t \tag{5.10b}$$

where dV_s/dt is the volumetric time rate of change of the eroding solid material. Equation 5.10a states that the total solids kinetic energy dissipated equals a solid pressure times a displacement. The erosion rate of the target, $\dot{E}_t$, is then obtained from

$$\dot{E}_t = \frac{\frac{dKE_{sPD}}{dt}}{P_t} \left(\frac{V_f}{A_t}\right) = - \dot{E}_{PD} \tag{5.11}$$

where dKE_{sPD}/dt, the solids kinetic energy, plays the role of U in Kick's law (Eq. 5.1). The power dissipation erosion model has been derived heuristically in this section by generalizing the empirical abrasive erosion relationships. The more general energy

dissipation model will be derived by more fundamental means in Sec. 5.2. The power dissipation model will be shown to be a special case of the energy dissipation model.

Ushimaru et al.[82] implemented this apparently fundamental power dissipation erosion model to analyze steady-state scouring erosion in a slurry jet pump and obtained reasonable comparisons with data. They used a hydrodynamic code similar to that used by Sheldon, Maji, and Crowe[77] (a variant of the TEACH code[80]).

The fluid flow equations used earlier[77] were extended to handle dense solid-liquid slurries. The Eulerian particle momentum equation treats the particles as a continuum. The standard two-parameter turbulence model was used for the liquid phase. A boundary-fitted coordinate transformation technique was used to generate the computational mesh. The other features of the model closely resemble those of Pourahmadi and Humphrey's.[56]

The computed results of the two-dimensional, incompressible, steady-state code were used as inputs to the power dissipation erosion model. This erosion model was implemented in one dimension, to compute the erosion rate of the slurry jet pump walls.

The steady-state one-dimensional form of the power dissipation model is given by

$$\dot{E}_{PD} = -C\ (1 - \varepsilon)\rho_s U_s U_s \frac{\partial U_s}{\partial x} \Delta/E_{sp} \tag{5.12a}$$

With reference to Fig. 12, the finite-difference approximation to Eq. 5.12a for erosion of a horizontal surface is given by

$$\dot{E}_{PD} = -C\ (1 - \varepsilon_o)\rho_s U_{s1}\ U_{s1}\left(\frac{U_{s2} - U_{s1}}{\Delta x}\right) \Delta y/E_{sp} \tag{5.12b}$$

where Δy has been used for Δ, the layer thickness, and the donor cell formulation has been used for U_{so}.

Ushimaru et al.[82] applied an empiricism that indicates that, when metal is removed with sandpaper, less than 10% of the grains in contact with the surface actually remove metal.[87] The remaining particles cause only elastic deformation, which does not result in material wear. Hence, the factor C was taken to be 0.1. As discussed above and in Sec. 3, such factors are influenced by the hardness of the erodent relative to the eroding surface and the erosion mechanism, cutting tool (impaction) or sandpaper (abrasion).

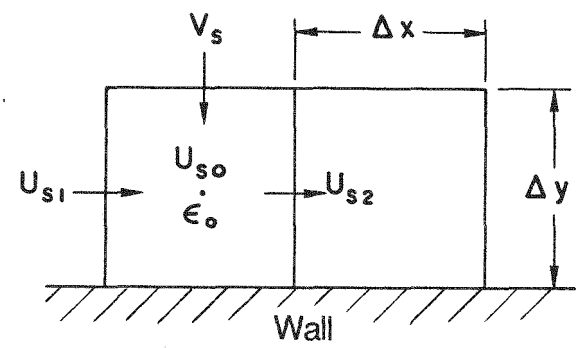

FIGURE 12 Finite-Difference Region for Power Dissipation Erosion Model

5.1.2 Linkage to Algebraic Erosion Models

It is possible to develop a link to the algebraic single-particle and fluidized-bed impaction erosion models discussed in Sec. 3. These models rely on particle energy dissipation and energy transfer to the eroding surface. On the other hand, the abrasion erosion models utilize the force of the particles on the eroding material surface. By explicitly computing this force via Eq. 5.5, we can show the basic equivalence of these two types of erosion models. This equivalence, which arises because both erosion models rely on the concept of cutting of the eroding surface, has not been discussed in the erosion literature. The only difference is in the view of how the cutting takes place -- by the action of the energy of the particle or by the action of the force of the particle. We will use the Finnie erosion model as an example of the linkage.

The steady-state form of the power dissipation erosion model can be written as:

$$\dot{E}_{PD} = - \frac{C}{E_{sp}} (1 - \varepsilon)\rho_s \vec{v}_s^2 \cdot \nabla(\vec{v}_s)\left(\frac{V_f}{A_t}\right) \tag{5.13}$$

Finnie's erosion model can be written as

$$\dot{E}_F = \frac{C}{\Delta_c} (1 - \varepsilon)\rho_s |\vec{v}_s| \vec{v}_s^2 \, \Delta_c f(\alpha)/p \tag{5.14}$$

where Δ_c is the depth of the cut. Now the linkage can be made explicit:

Finnie Model		Power Dissipation Model	
$\dfrac{(1 - \varepsilon)\vec{\rho}_s \lvert\vec{v}_s\rvert \vec{v}_s^2 \, f(\alpha)}{\Delta_c}$	<------->	$- (1 - \varepsilon)\rho_s \vec{v}_s^2 \cdot \nabla(\vec{v}_s) = - \dfrac{dKE_{sPD}}{dt}$	(5.15a)
Δ_c	<------->	V_f/A_t	(5.15b)
and			
p	<------->	E_{sp}	(5.15c)

The differential form of the solids kinetic energy replaces the magnitude of the algebraic solids kinetic energy times an angular dependence, divided by a depth of cut. The ratio of fluid volume to target area replaces the depth of cut, and the specific energy replaces the flow pressure. There is an implicit fluid-mechanical angular effect in the differential form of the kinetic energy. Function $f(\alpha)$ may be viewed as a part of the material-property relationships (as well as Δ_c), because it results from integrating the equations of motion for the particle gouging the eroding wall.

5.1.3 Extension to Account for Particle Size and Threshold Energy Dependence

As was shown in Secs. 5.1.1 and 5.1.2, the power dissipation model evolves from the empirical laws of comminution and abrasion, and can be linked to algebraic single-particle and fluidized-bed impaction erosion models. However, the former laws hold only for very small particles, typically less than 1 μm. Another relationship, Rittinger's law, also goes back more than 100 years.[84,88] It states that the energy required to crush a substance is proportional to the production of new area according to the following relationship:

$$U = K_2(A - A_1) \tag{5.16a}$$

where K_2 has the units of N/m. Walker and Shaw[84] showed that Eq. 5.16a is equivalent to the much more meaningful form,

$$\frac{U - U_o}{V_p} = K_2/\delta \tag{5.16b}$$

where $\delta = A/V_p$ is the thickness of the layer removed, assumed to be the same as the particle size. Equation 5.16b states that the energy needed to crush a volume of particles actually decreases for larger particles. Rewriting Eq. 5.16b in terms of the volume of particles, V_p, results in

$$V_p = \frac{U - U_o}{K_2/\delta} \tag{5.17a}$$

Using the analogy between Kick's law and Rabinowicz's abrasion expression (Eqs. 5.3a and 5.3b in Sec. 5.1.1), we replace $U - U_o$ by $FL - (FL)_o$ to obtain

$$V_p = \frac{FL - (FL)_o}{K_2/\delta} \tag{5.17b}$$

In this form, Rittinger's law looks like Rabinowicz's abrasion model with a hardness that depends on particle size, $(3/k)\,H = K_2/\delta$, where K_2 is a material property resembling surface tension and $(FL)_o$ is a sort of threshold energy, which may itself depend on particle size. Expressing Eq. 5.17b in terms of the volumetric loss per unit time per unit area, we obtain

$$\dot{E} = \frac{\dot{V}_p}{A_t} = \frac{C[\vec{F}_s \cdot \vec{v}_s - (\vec{F}_s \cdot \vec{v}_s)_o]\, d_p}{A_t K_2} \tag{5.18}$$

where d_p has replaced δ. Thus, the erosion rate depends directly on the particle size. Substitution of Eq. 5.5 into Eq. 5.18 produces

$$\dot{E} = - \frac{C(1 - \varepsilon)\rho_s [\frac{d\vec{v}_s}{dt_s} \cdot \vec{v}_s - (\frac{d\vec{v}_s}{dt_s} \cdot \vec{v}_s)_o] \, d_p}{E'_{sp}} \tag{5.19}$$

where $E'_{sp} = K_2 (A_t/V_p)$ is a material property resembling hardness and possibly dependent on particle size.

Thus, in this extension of the power dissipation model, the erosion rate depends on a threshold energy and the particle diameter. This threshold energy is similar to the threshold energies used by Bitter[60,61] and by Neilson and Gilchrist[62] in their single-particle-impaction erosion models.

We have demonstrated that there is a strong connection between cutting or impaction erosion and abrasion erosion. This association was made possible by introducing the force of the particles on the eroding surface and by associating this force times a displacement with the particles' kinetic energy.

Shook et al.[86] found slurry erosion rates to increase with particle diameter. The dependence could be linearized for particle diameters over a range of 100-400 μm. Above this size, the erosion rate increased hardly at all. Below 100 μm, the erosion rate fell to zero, which, we infer, supports the existence of a threshold energy.

Walker and Shaw[84] argue that the important aspect of particle size dependence for the grinding energy requirements has to do with the probability of finding flaws in the particles. Very small particles, because they have correspondingly fewer flaws, are much more difficult to break up, and follow Kick's law. Larger particles have a larger number of flaws, and break up below their theoretical strength; so they follow Rittinger's law. The fact that normally brittle and ductile materials also follow Kick's and Rittinger's laws is also explained by the size effect. Very high-pressure, small particles cause plastic flow to occur before a flaw is encountered. Thus, materials like marble, which are brittle in the bulk, are ductile in the size range of ball mill grinding (1-1000 μm), and follow the same laws that apply to the grinding of steel by belts and wheels.

Such behavior has also been observed in later, independent erosion tests by Sheldon and Finnie.[63] They found that, at the same nominal velocity of 152 m/s, 9-μm SiC particles eroded glass in a ductile manner, whereas 21-μm and 127-μm SiC particles exhibited brittle wear. Hence, the concept of the explicit angular dependence describing single-particle ductile and brittle erosion may not be applicable to multiple-particle erosion. What may actually be occurring is a continuous energy transfer to the surface by the particles, producing pressures that may be in excess of the plastic flow limits. This pressure distribution is determined by the fluid mechanics of the continuum of particles, and could be computed from the force of the particles on the surface.

It is possible that particle surface roughness acts very much like very small particles; in this case, the erosion behavior would follow a ductile model. Most of the surface damage to the eroding surface is caused by the roughness, much as in a ball mill. This may explain why Wood and Woodford [68] found that dolomite and alundum, which differ greatly in hardness, erode tubes at very much the same rate. The erosion experiments with dolomite had to be terminated after only 20 h, because the filtering system could not handle the fine dust created by the comminution of the particles.

5.1.4 Extension to Two Dimensions

As discussed in Sec. 5.1.1, the power dissipation model used by Ushimaru et al.[82] was used in one dimension (finite-differenced next to the eroding wall), even though the solid phase flow is two-dimensional. Hence, the velocity in the y direction, V_s, shown in Fig. 12 was not used. This is justifiable if the solids flow next to the wall in the axial direction is much greater than in the transverse direction (i.e., $U_s >> V_s$). Examination of their computed velocity fields showed this to be a good assumption.

The solids (and gas) velocity fields corresponding to the two-dimensional fluidized-bed computations reported in Sec. 2.2 were time-averaged over 2.5 s. This has been determined to be a long enough for good time-averaging, because the gas mass flux exiting the top of the bed differs by less than 1% from that entering the bottom of the bed. The solids velocity vector plot in Fig. 13 shows three regions of recirculation: two on either side of the obstacle, indicating a vortex, and one above the obstacle. The gas flows upward everywhere. The time-averaged porosity distribution was shown in Fig. 10, where it compared well with the data. Examination of the computed time-averaged solid phase velocity field next to the obstacle leads to the conclusion that it is highly two-dimensional. Hence, the one-dimensional power dissipation model given by Eq. 5.5 is inadequate.

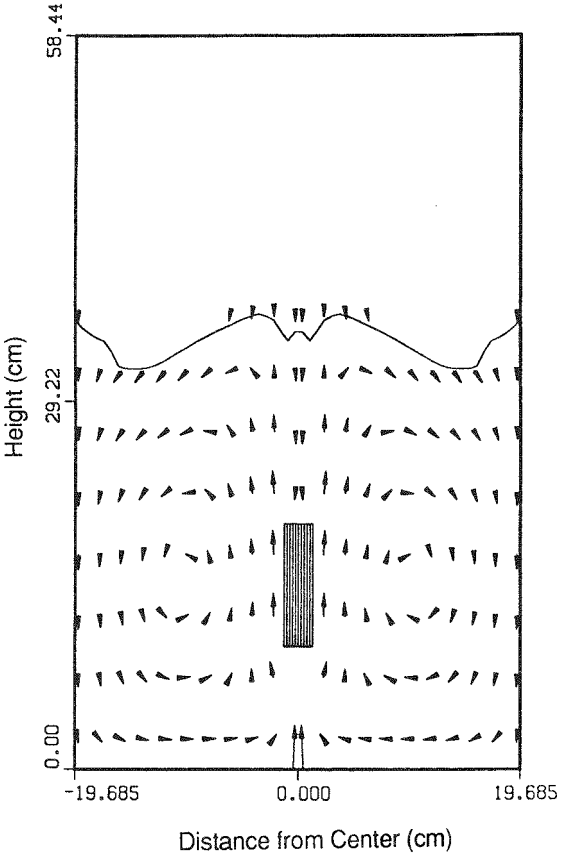

FIGURE 13 Solids Velocities Time-Averaged over 2.5 s

The extension of the power dissipation model to two dimensions is given by the following equation:

$$\dot{E}_{PD} = -C\left(\frac{V_f}{A_t}\right)\rho_s\,(1-\varepsilon)\left[U_s\left(U_s\frac{\partial U_s}{\partial x} + V_s\frac{\partial U_s}{\partial y}\right) + V_s\left(U_s\frac{\partial V_s}{\partial x} + V_s\frac{\partial V_s}{\partial y}\right)\right]/E_{sp} \tag{5.20}$$

For erosion on a horizontal surface (shown in Figs. 12 and 14), $V_f/A_t = \Delta x \cdot \Delta y/\Delta x = \Delta y$. For erosion on a vertical surface, $V_f/A_t = \Delta x \cdot \Delta y/\Delta y = \Delta x$.

It may be interesting to interpret a somewhat simplified two-dimensional power dissipation model in terms of the concepts of impaction and scouring or abrasive wear. If the cross-product terms $U_s(\partial V_s/\partial x)$ and $V_s(\partial U_s/\partial y)$ are neglected, Eq. 5.20 becomes

$$\dot{E}_{PD} = -C\left(\frac{V_f}{A_t}\right)\rho_s\,(1-\varepsilon)\left(U_s^2\frac{\partial U_s}{\partial x}\right)/E_{sp} - C\left(\frac{V_f}{A_t}\right)\rho_s\,(1-\varepsilon)\left(V_s^2\frac{\partial V_s}{\partial y}\right)/E_{sp} \tag{5.21a}$$

The first term of Eq. 5.21a is the model Ushimaru et al. [82] used for scouring erosion. We will refer to it as the scouring erosion model, $\dot{E}_{SPD}$. The second term of Eq. 5.21a can be interpreted as an impaction erosion model, $\dot{E}_{IPD}$. Thus, Eq. 5.21a can be written as

$$\dot{E}_{PD} = \dot{E}_{SPD} + \dot{E}_{IPD} \tag{5.21b}$$

where:

$$\dot{E}_{SPD} = -C\left(\frac{V_f}{A_t}\right)\rho_s\,(1-\varepsilon)U_s^2\left(\frac{\partial U_s}{\partial x}\right)/E_{sp} \tag{5.21c}$$

$$\dot{E}_{IPD} = -C\left(\frac{V_f}{A_t}\right)\rho_s\,(1-\varepsilon)V_s^2\left(\frac{\partial V_s}{\partial y}\right)/E_{sp} \tag{5.21d}$$

The finite-difference approximation to Eq. 5.21c is given by Eq. 5.12b for a horizontal wall, and the finite-difference approximation to Eq. 5.21d for a horizontal wall can be given by reference to Fig. 14 as

$$\dot{E}_{IPD} = -C\,(1-\varepsilon_o)\rho_s V_{s2}^2\Delta y\left(\frac{V_{s2}-V_{s1}}{\Delta y}\right)/E_{sp} \tag{5.22a}$$

but, because $V_{s1} = 0$, Eq. 5.22a becomes simply

$$\dot{E}_{IPD} = -C\,(1-\varepsilon_o)\rho_s V_{s2}^3/E_{sp} \tag{5.22b}$$

which bears a strong resemblence to Finnie's erosion model, Eq. 3.2a.

The full two-dimensional power dissipation model given by Eq. 5.20 was differenced, and the erosion rates around the rectangular obstacle were calculated, using the time-averaged porosity and solids phase velocities. Details of the finite-differencing are given in Sec. 5.2.3. Because both positive and negative values of the power dissipation resulted for locations around the obstacle, it was concluded that the two-dimensional power dissipation model was incomplete.

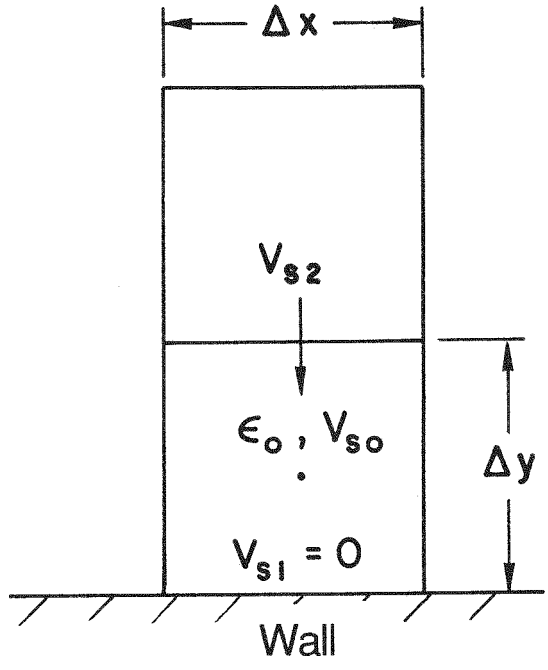

FIGURE 14 Finite-Difference Region for Two-Dimensional Power Dissipation Model

5.2 ENERGY DISSIPATION EROSION MODEL

The power dissipation model was discussed in Sec. 5.1.1. It is necessary to extend that model to a two-phase continuum, consisting of solids and fluid phases. The power dissipation model will be shown to be a special case of the more general energy dissipation model developed in this section. Details of the model implementation using outputs from the hydrodynamic model, and its finite-difference representation are also presented in this sections.

5.2.1 Derivation of the General Transient Energy Dissipation Model

The solids phase momentum equation given by Eqs. 2.4 and 2.6 with the viscous shear, $\bar{\bar{\tau}}_{sv}$, retained may be written in vector form as

$$\frac{\partial}{\partial t}[\rho_s(1-\epsilon)\vec{v}_s] + \nabla\cdot[\rho_s(1-\epsilon)\vec{v}_s\vec{v}_s]$$

$$= -(1-\epsilon)\nabla P + \bar{\bar{\beta}}(\vec{v}_g - \vec{v}_s) + G(\epsilon)\nabla\epsilon + \rho_s(1-\epsilon)\vec{g} \qquad (5.23a)$$

$$+ \nabla\cdot[(1-\epsilon)\bar{\bar{\tau}}_{sv}]$$

Equation 5.23a may be written in nonconservation form as

$$\rho_s(1-\varepsilon)\frac{\partial \vec{v}_s}{\partial t} + \rho_s(1-\varepsilon)\vec{v}_s \cdot \nabla \vec{v}_s = -(1-\varepsilon)\nabla P + \bar{\bar{\beta}}(\vec{v}_g - \vec{v}_s) + G(\varepsilon)\nabla\varepsilon + \rho_s(1-\varepsilon)\vec{g} + \nabla\cdot[1-\varepsilon)\bar{\bar{\tau}}_{sv}] \tag{5.23b}$$

Following Bird, Stewart, and Lightfoot,[89] the equation of mechanical energy is obtained by taking the scalar product of the solids velocity, $\vec{v}_s$, with Eq. 5.23b to obtain:

$$\rho_s(1-\varepsilon)\vec{v}_s \cdot \frac{\partial \vec{v}_s}{\partial t} + \rho_s(1-\varepsilon)\vec{v}_s \cdot (\vec{v}_s \cdot \nabla\vec{v}_s) = -(1-\varepsilon)\vec{v}_s \cdot \nabla P + \vec{v}_s \cdot \bar{\bar{\beta}} \cdot (\vec{v}_g - \vec{v}_s) + v_s \cdot G(\varepsilon)\nabla\varepsilon + \rho_s(1-\varepsilon)\vec{v}_s \cdot \vec{g} + \vec{v}_s \cdot [\nabla \cdot (1-\varepsilon)\bar{\bar{\tau}}_{sv})] \tag{5.23c}$$

This derivation follows that of Bird, Stewart, and Lightfoot extended to multiphase flow.[89] Note that the sign convention of the viscous terms used is opposite to that of Bird et al., and agrees with that used in the K-FIX computer code.[36]

The very last term in Eq. (5.23b) may be split into two terms as:

$$\vec{v}_s \cdot [\nabla \cdot (\varepsilon_s \bar{\bar{\tau}}_{sv})] = \nabla \cdot [(\varepsilon_s \bar{\bar{\tau}}_{sv}) \cdot \vec{v}_s] - (\varepsilon_s \bar{\bar{\tau}}_{sv}) : \nabla \vec{v}_s \tag{5.24}$$

The first term in Eq. (5.24) represents the rate of reversible work done by the solids viscous forces, while the second term represents the rate of irreversible convertion to internal energy and can be shown to be always by positive.[89] Substitution of Eq. (5.24) into Eq. 5.23b) and solving for the rate of irreversible conversion to internal energy, $E_{vs} = -dKE_s/dt$,

$$e_{vs} = -\frac{dKE_s}{dt} = (\varepsilon_s \bar{\bar{\tau}}_{sv}) : \nabla \vec{v}_s = \underbrace{-\varepsilon_s\rho_s\vec{v}_s \cdot \frac{\partial \vec{v}_s}{\partial t}}_{1} + \underbrace{\varepsilon_s\rho_s\vec{v}_s \cdot (\vec{v}_s \cdot \nabla \vec{v}_s)}_{2} + \underbrace{(\varepsilon_s \vec{v}_s) \cdot \nabla P}_{3} + \underbrace{\vec{v}_s \cdot \beta \cdot \vec{v}_s - (\vec{v}_s - \vec{v}_g) - \vec{v}_g}_{4} - \underbrace{\vec{v}_s \cdot G(\varepsilon) \nabla \varepsilon}_{5} - \underbrace{\varepsilon_s\rho_s\vec{v}_s \cdot \vec{g}}_{6} - \underbrace{\nabla \cdot [(\varepsilon_s \bar{\bar{\tau}}_{sv}) \cdot \vec{v}_s]}_{7} \tag{5.25}$$

Where ε_s is $1 - \varepsilon$.

Equation 5.25 is simply that portion of the solid phase mechanical energy equation resulting in the rate of *irreversible* conversion to internal energy, a portion of which is available for energy transfer to the solid surface to produce erosion (i.e., the rate of kinetic energy dissipation per unit volume). It is a direct extension of the well-accepted single-phase expression.[89] The seven terms on the righthand side of Eq. 5.25 represent to following:

Term 1 = rate of increase in kinetic energy

Term 2 = net rate of input of kinetic energy by bulk flow

Term 3 = rate of reversible conversion to internal energy plus rate of work done by pressure of surroundings on volume element

Term 4 = rate of work done by drag between the gas and solids on volume element

Term 5 = rate of work done by solids stress on volume element

Term 6 = rate of work done by gravitational force on volume element

Term 7 = rate of work done by viscous forces on volume element

Clearly, each term must be present, because each has a physical interpretation contributing to the energy dissipation. Equation 5.25 is the rational extension of the kinetic energy dissipation given by Eq. 5.10a in the power dissipation erosion model. Hence, the energy dissipation with $\underline{\underline{\tau}}$ set to equal zero can be expressed as:

$$\frac{dKE_s}{dt} = \frac{dKE_{sPD}}{dt} + \varepsilon_s \vec{v}_s \cdot \nabla P + \vec{v}_s \cdot \vec{\beta}(\vec{v}_s - \vec{v}_g) \qquad (5.26)$$

$$- \vec{v}_s \cdot G(\varepsilon)\nabla\varepsilon - \varepsilon_s \rho_s \vec{v}_s \vec{g}$$

For nonviscous flow (zero shear), the energy dissipation would be zero, and all the energy forms in Eq. 5.25 would be freely interconvertible. However, the introduction of stationary surfaces, such as obstacles, introduces gradients because of the prescription of zero normal and tangential velocities on the surfaces. Therefore, nonzero energy dissipation is produced, which can only be computed from the numerical solution of a problem where the flow has evolved from the imposition of the obstacle.

In Cartesian coordinates, Eq. 5.25 becomes

$$\frac{dKE_s}{dt} = \varepsilon_s\rho_s[\frac{\partial}{\partial t}(\frac{1}{2}U_s^2) + \frac{\partial}{\partial t}(\frac{1}{2}V_s^2)]$$

$$+ \varepsilon_s\rho_s[U_s(U_s\frac{\partial U_s}{\partial x} + V_s\frac{\partial U_s}{\partial y}) + V_s(U_s\frac{\partial V_s}{\partial x} + V_s\frac{\partial V_s}{\partial y})] \qquad (5.27)$$

$$+ \varepsilon_s U_s\frac{\partial P}{\partial x} + \varepsilon_s V_s\frac{\partial P}{\partial y} + U_s\beta_x(U_s - U_g) + V_s\beta_y(V_s - V_g)$$

$$- U_s G(\varepsilon)\frac{\partial \varepsilon}{\partial x} - V_s G(\varepsilon)\frac{\partial \varepsilon}{\partial y} + \varepsilon_s\rho_s V_s g$$

where $\vec{g} = -g$ (gravity negative downward).

5.2.2 Derivation of the Time-Averaged Energy Dissipation Model

When the time-dependent terms are dropped, the steady-state energy dissipation model results.

Define the time average of some function f as

$$\langle f\rangle = \int_{t_o}^{t_o+\Delta t} f\, dt/\Delta t \qquad (5.28)$$

The time average of the solids continuity equation (Eq. 2.2) is given (after interchanging the order of averaging and differential operations) by:

$$\frac{\partial}{\partial t}\langle\varepsilon_s\rho_s\rangle + \frac{\partial}{\partial x}\langle\varepsilon_s\rho_s U_s\rangle + \frac{\partial}{\partial y}\langle\varepsilon_s\rho_s V_s\rangle = 0 \qquad (5.29)$$

With reference to Fig. 15, if we assume that Δt is large compared with the period of the oscillations and that a limit-cycle steady state is achieved as indicated, then

$$\lim_{t\to\infty}\langle\varepsilon_s\rho_s\rangle = \langle\varepsilon_s\rho_s\rangle_{ss} \neq f(t) \Rightarrow \lim_{t\to\infty}\frac{\partial}{\partial t}\langle\varepsilon_s\rho_s\rangle \to 0 \qquad (5.30)$$

Ideally, the time to begin the time-averaging is after the first bubble has passed, typically 0.5 s (as shown in Fig. 8 and schematically in Fig. 15); then Δt can be made smaller. If Δt is finite (large compared with the small-scale oscillations, but small compared with the large-scale time variation), the nonoscillatory curve $\langle f\rangle$ would result, as shown in Fig. 15. However, if a limit-cycle steady state exists, the time-averaged function would go to the steady-state value, $\langle f\rangle_{ss}$, as indicated.

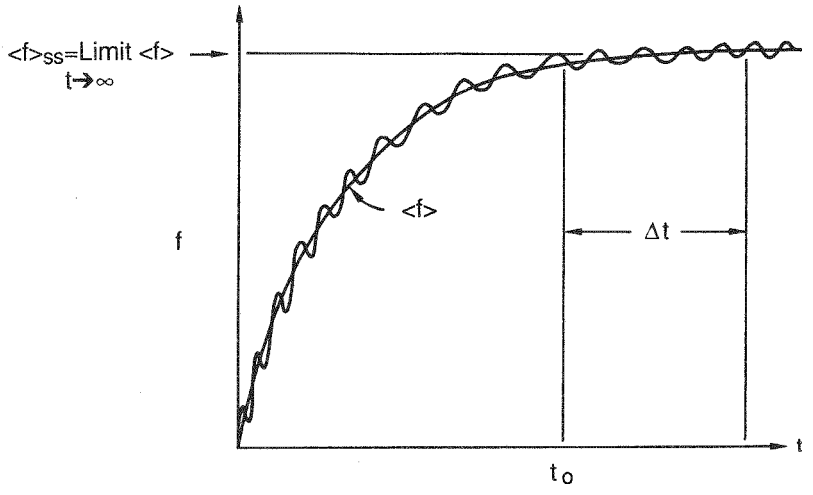

FIGURE 15 Time-Averaging of an Oscillatory Function

With the foregoing arguments, the time-averaged solid-phase continuity equation becomes

$$\frac{\partial}{\partial x}\langle \varepsilon_s \rho_s U_s \rangle + \frac{\partial}{\partial y}\langle \varepsilon_s \rho_s V_s \rangle = 0 \tag{5.31}$$

Time-averaging Eqs. 2.4 and 2.6 and using the same argument used for the continuity equation gives

$$\frac{\partial}{\partial x}\langle \rho_s \varepsilon_s U_s U_s \rangle + \frac{\partial}{\partial y}\langle \rho_s \varepsilon_s V_s U_s \rangle = -\langle \varepsilon_s \frac{\partial P}{\partial x} \rangle + \langle \beta_x (U_g - U_s) \rangle + \langle G(\varepsilon) \frac{\partial \varepsilon}{\partial x} \rangle \tag{5.32a}$$

and

$$\frac{\partial}{\partial x}\langle \rho_s \varepsilon_s U_s V_s \rangle + \frac{\partial}{\partial y}\langle \rho_s \varepsilon_s V_s V_s \rangle = -\langle \varepsilon_s \frac{\partial P}{\partial y} \rangle + \langle \beta_y (V_g - V_s) \rangle - \langle \rho_s \varepsilon_s g \rangle + \langle G(\varepsilon) \frac{\partial \varepsilon}{\partial y} \rangle \tag{5.32b}$$

In the FLUFIX code we now compute the time average of each variable (ε_s, U_s, V_s, U_g, V_g, and P) individually. The density, ρ_s, is constant. Therefore, we must relate the time average of products to the product of time averages. Let each variable be expressed as the sum of the time average plus a fluctuating component:

$$\varepsilon_s = \langle \varepsilon_s \rangle + \varepsilon_s'$$

$$U_s = \langle U_s \rangle + U_s'$$

$$V_s = \langle V_s \rangle + V_s'$$

$$U_g = \langle U_g \rangle + U'_g$$

$$V_g = \langle V_g \rangle + V'_g$$

and

$$P = \langle P \rangle + P'$$

For constant solid phase density, ρ_s, the time-averaged continuity equation (Eq. 5.31) then becomes

$$\frac{\partial}{\partial x}(\rho_s \langle \varepsilon_s \rangle \langle U_s \rangle) + \frac{\partial}{\partial x}(\rho_s \langle \varepsilon_s \rangle \langle V_s \rangle) - \text{DIFFSC} \tag{5.33}$$

where:

$$\text{DIFFSC} = -\frac{\partial}{\partial x}(\rho_s \langle \varepsilon'_s U'_s \rangle) - \frac{\partial}{\partial y}(\rho_s \langle \varepsilon'_s V'_s \rangle) \tag{5.34}$$

The symbol DIFFSC (Diffusion of Solids via Convection) has been used because the extra terms are suggestive of turbulent diffusion.[89] These terms are zero for a true steady state, but not for a limit-cycle steady state.

The time-averaged solid phase momentum equations become

$$\frac{\partial}{\partial x}(\rho_s \langle \varepsilon_s \rangle \langle U_s \rangle \langle U_s \rangle) + \frac{\partial}{\partial y}(\rho_s \langle \varepsilon_s \rangle \langle V_s \rangle \langle U_s \rangle) = -\langle \varepsilon_s \rangle \frac{\partial \langle P \rangle}{\partial x} + \langle \beta_x \rangle (\langle U_g \rangle - \langle U_s \rangle) + \langle G(\varepsilon) \rangle \frac{\partial \langle \varepsilon \rangle}{\partial x} + \text{DIFFSMX} \tag{5.35a}$$

and

$$\frac{\partial}{\partial x}(\rho_s \langle \varepsilon_s \rangle \langle U_s \rangle \langle V_s \rangle) + \frac{\partial}{\partial y}(\rho_s \langle \varepsilon_s \rangle \langle V_s \rangle \langle V_s \rangle) = -\langle \varepsilon_s \rangle \frac{\partial \langle P \rangle}{\partial y} + \langle \beta_y \rangle (\langle V_g \rangle - \langle V_s \rangle) - \rho_s \langle \varepsilon_s \rangle g + \langle G(\varepsilon) \rangle \frac{\partial \langle \varepsilon \rangle}{\partial y} + \text{DIFFSMY} \tag{5.35b}$$

DIFFSMX and DIFFSMY contain terms analagous to DIFFSC, arising from a limit-cycle steady state. Terms contained in DIFFSMX and DIFFSMY are suggestive of turbulent viscosity.

Now, it is possible to combine the solid-phase time-averaged continuity equation with the solid-phase time-averaged momentum equations to obtain the solid-phase momentum equations in nonconservative form as

$$\rho_s\langle\varepsilon_s\rangle\langle U_s\rangle\frac{\partial\langle U_s\rangle}{\partial x} + \rho_s\langle\varepsilon_s\rangle\langle V_s\rangle\frac{\partial\langle U_s\rangle}{\partial y} = -\langle\varepsilon_s\rangle\frac{\partial\langle P\rangle}{\partial x}$$

$$+ \langle\beta_x\rangle(\langle U_g\rangle - \langle U_s\rangle) + \langle G(\varepsilon)\rangle\frac{\partial\langle\varepsilon\rangle}{\partial x} + \text{DIFFSMX} - \langle U_s\rangle\text{DIFFSC} \tag{5.36a}$$

and

$$\rho_s\langle\varepsilon_s\rangle\langle U_s\rangle\frac{\partial\langle V_s\rangle}{\partial x} + \rho_s\langle\varepsilon_s\rangle\langle V_s\rangle\frac{\partial\langle V_s\rangle}{\partial y} = -\langle\varepsilon_s\rangle\frac{\partial\langle P\rangle}{\varepsilon y}$$

$$+ \langle\beta_y\rangle(\langle V_g\rangle - \langle V_s\rangle) - \rho_s\langle\varepsilon_s\rangle g + \langle G(\varepsilon)\rangle\frac{\partial\langle\varepsilon\rangle}{\partial y} \tag{5.36b}$$

$$+ \text{DIFFSMY} - \langle V_s\rangle\text{DIFFSC}$$

The time-averaged energy dissipation can be computed by multiplying Eq. 5.36a by $\langle U_s\rangle$ and Eq. 5.36b by $\langle V_s\rangle$ and adding to obtain

$$\left\langle\frac{dKE_s}{dt}\right\rangle = \rho_s\langle\varepsilon_s\rangle\left[\langle U_s\rangle\left(\langle U_s\rangle\frac{\partial\langle U_s\rangle}{\partial x} + \langle V_s\rangle\frac{\partial\langle U_s\rangle}{\partial y}\right),\right.$$

$$\left. + \langle V_s\rangle\left(\langle U_s\rangle\frac{\partial\langle V_s\rangle}{\partial x} + \langle V_s\rangle\frac{\partial\langle V_s\rangle}{\partial y}\right)\right]$$

$$+ \langle\varepsilon_s\rangle\langle U_s\rangle\frac{\partial\langle P\rangle}{\partial x} + \langle\varepsilon_s\rangle\langle V_s\rangle\frac{\partial\langle P\rangle}{\partial y} + \langle U_s\rangle\langle\beta_x\rangle(\langle U_s\rangle - \langle U_g\rangle)$$

$$+ \langle V_s\rangle\langle\beta_y\rangle(\langle V_s\rangle - \langle V_g\rangle) - \langle U_s\rangle\langle G(\varepsilon)\rangle\frac{\partial\langle\varepsilon\rangle}{\partial x} + \rho_s\langle V_s\rangle\langle\varepsilon_s\rangle g$$

$$- \langle V_s\rangle\langle G(\varepsilon)\rangle\frac{\partial\langle\varepsilon\rangle}{\partial y} + (\langle U_s\rangle^2 + \langle V_s\rangle^2)\text{DIFFSC}$$

$$- \langle U_s\rangle\text{DIFFSMX} - \langle V_s\rangle\text{DIFFSMY} \cdot \tag{5.37}$$

Comparison of Eq. 5.37 with Eq. 5.27 (with the time-dependent terms dropped) shows that extra terms enter into the time-averaged energy dissipation. These extra terms are dropped when the energy dissipation is evaluated using time-averaged FLUFIX hydrodynamic results, and this is considered to be the reason that inaccuracies can arise. Similar inaccuracies arise with the power dissipation model. It is possible to evaluate the extra terms in Eq. 5.37, but it is more straightforward to evaluate the time-dependent energy dissipation, using Eq. 5.27, and then do time-averaging.

From an engineering standpoint, time-averaged equations are more desirable than time-dependent equations for calculating erosion rates. The trade-off is decreased computer storage cost with the acceptance of inaccuracies in the evaluation of the time-averaged energy dissipation with the extra terms dropped, versus improved accuracy in the time-averaged evaluation of the time-dependent energy dissipation, with substantially increased computer storage costs. In many circumstances, the results should be close, and they generally are, as shown in Sec. 6.

5.2.3 Implementation and Finite-Difference Equations

The application of algebraic and differential erosion models to fluidized beds is described in this section, as well as the finite difference equations for the power and energy dissipation models.

5.2.3.1 Coupling of Hydrodynamic and Erosion Models

A typical FLUFIX computational cell next to a tube surface is shown in Fig. 16. If the tube is round, it must be approximated (with a "staircase" approximation) as indicated, because Cartesian coordinates are used. The normal and tangential velocities of the gas and solid phases are set equal to zero on all the approximate tube surfaces. If the obstacle is rectangular and aligned along the coordinate direction, no approximation is necessary.

If the algebraic models described in Sec. 3 are used, the solid phase velocities in each direction are resolved at the cell center and the magnitude of the velocity is obtained. The angle of the resolved velocity vector at the cell center with respect to each horizontal and vertical approximate tube surface is then obtained. The porosity is known at the cell center; so the mass flux of the solid is computed from the magnitude of the velocity resolved at the cell center and the porosity times the density (which is

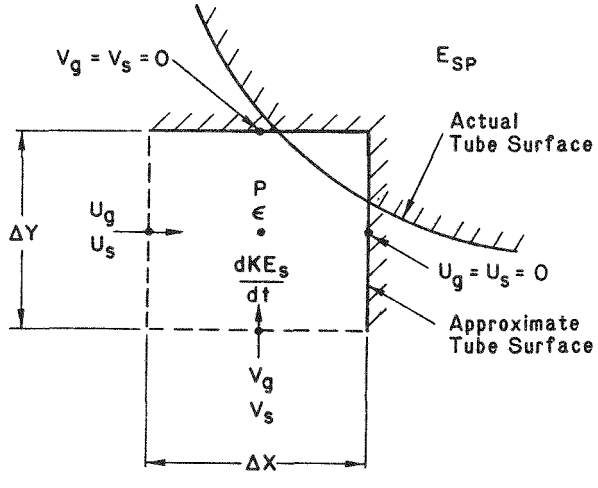

FIGURE 16 Coupling of Hydrodynamic and Erosion Models

constant). Given the tube material hardness, E_{sp}, or flow pressure, p, and some estimate for the fraction of the particles causing material removal, the erosion rate is obtained. This is done at present in a postprocessor code called ENERGY, which uses as inputs either the time-averaged or fluctuating FLUFIX outputs (saved from the solution of the hydrodynamic equations).

If the power dissipation model is used, derivatives of the solid phase kinetic energy must be evaluated to compute the power dissipation at the cell centers around the obstacle. This may be either a transient or a time-averaged calculation.

If the energy dissipation model is used, the gas phase velocities are needed to compute the rate of work done by drag between the gas and solid, and gradients of pressure are needed to evaluate the pressure work terms. A detailed description of the finite-differencing is given in the next section.

5.2.3.2 Energy Dissipation Finite Difference Equations

The energy dissipation expression given by Eq. 5.27 is evaluated in finite-difference form at the middle of each control volume of interest. Because the velocities are known only at the cell edges, they are averaged in each direction when they are needed at the cell center. Figure 17 illustrates the nomenclature used for cell (IJ). The

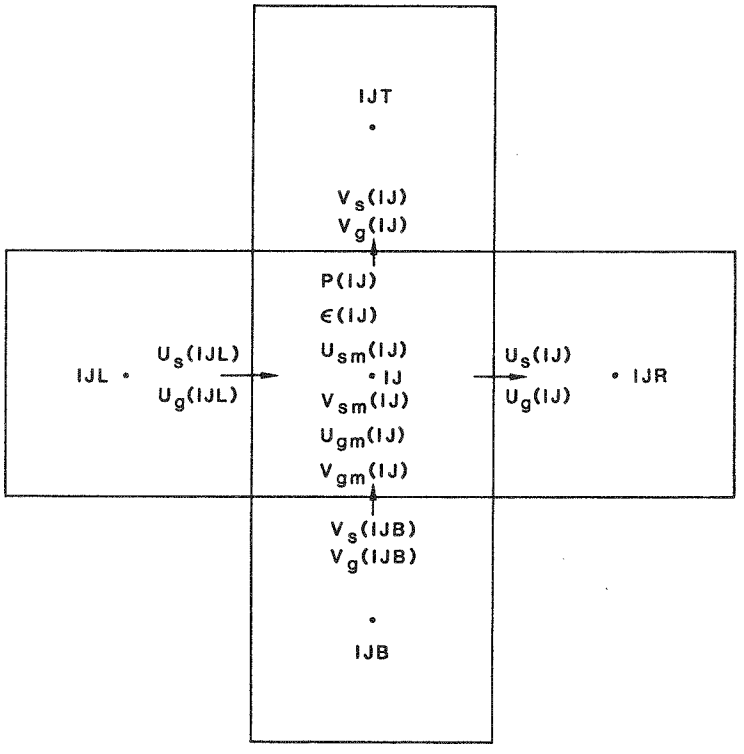

FIGURE 17 General Finite-Difference Nomenclature for Evaluation of Energy Dissipation

indexes IJ, IJL, IJR, IJB, and IJT refer to cells at the center, left, right, bottom, and top, respectively. The average values of the phase velocities at the cell centers, denoted by U_{sm}, V_{sm}, U_{gm}, and V_{gm}, are as follows:

$$U_{sm}(IJ) = [U_s(IJL) + U_s(IJ)]/2 \tag{5.38}$$

$$V_{sm}(IJ) = [V_s(IJB) + V_s(IJ)]/2$$

and similarly for the gas phase. All six variables for cell IJ are shown in Fig. 17, where the cell edge velocities (together with their notation) are also given. The finite-differencing is straightforward, in general, using forward in time and central in space (FTCS) differencing. There is ambiguity in evaluating some of the gradient terms at the obstacle boundary. Therefore, for reference purposes, we summarize all the expressions used and give suggestions for alternatives here.

The general implicit finite-difference approximation to Eq. 5.27 is given by

$$T1 \equiv \varepsilon_s\rho_s \frac{\partial}{\partial t}\left(\frac{1}{2}U_s^2\right) = \frac{1}{2}\rho_s\varepsilon_s^n[(U_{sm}^{n+1})^2 - (U_{sm}^n)^2]/\Delta t\ (IJ) \tag{5.39a}$$

and

$$T2 \equiv \varepsilon_s\rho_s \frac{\partial}{\partial t}\left(\frac{1}{2}V_s^2\right) = \frac{1}{2}\rho_s\varepsilon_s^n[(V_{sm}^{n+1})^2 - (V_{sm}^n)^2]/(IJ)\ \Delta t \tag{5.39b}$$

$$C1 \equiv \varepsilon_s\rho_s U_s^2 \frac{\partial U_s}{\partial x} = \rho_s(\varepsilon_s U_{sm}^2)^{n+1}\ (IJ)[U_s(IJ) - U_s(IJL)]^{n+1}/\Delta x \tag{5.39c}$$

$$C2 \equiv \varepsilon_s\rho_s V_s^2 \frac{\partial V_s}{\partial y} = \rho_s(\varepsilon_s V_{sm}^2)^{n+1}\ (IJ)[V_s(IJ) - V_s(IJB)]^{n+1}/\Delta y \tag{5.39d}$$

$$C3 \equiv \varepsilon_s\rho_s U_s V_s \frac{\partial U_s}{\partial y} = \rho_s(\varepsilon_s U_{sm} V_{sm})^{n+1}(IJ)[U_s(IJT) - U_s(IJB)]^{n+1}/2\Delta y \tag{5.39e}$$

$$C4 \equiv \varepsilon_s\rho_s U_s V_s \frac{\partial V_s}{\partial x} = \rho_s(\varepsilon_s U_{sm} V_{sm})^{n+1}(IJ)[V_s(IJR) - V_s(IJL)]^{n+1}/2\Delta x \tag{5.39f}$$

$$-PUL \equiv \varepsilon_s U_s \frac{\partial P}{\partial x} - U_s G(\varepsilon)\frac{\partial \varepsilon}{\partial x} = (\varepsilon_s U_{sm})^{n+1}(IJ)[P(IJR) - P(IJL)]^{n+1}/2\Delta x$$
$$- [G(\varepsilon)U_{sm}]^{n+1}(IJ)[\varepsilon(IJR) - \varepsilon(IJL)]^{n+1}/2\Delta x \tag{5.39g}$$

$$-PVL \equiv \varepsilon_s \rho_s V_s \frac{\partial P}{\partial y} - V_s G(\varepsilon)\frac{\partial \varepsilon}{\partial y} = (\varepsilon_s V_{sm})^{n+1}(IJ)[P(IJT) - P(IJB)]^{n+1}/2\Delta y$$

$$-[G(\varepsilon)V_{sm}]^{n+1}(IJ)[\varepsilon(IJT) - \varepsilon(IJB)]^{n+1}/2\Delta y \qquad (5.39h)$$

$$-FRIC \equiv U_s \beta_x (U_s - U_g) + V_s \beta_y (V_s - V_g) \qquad (5.39i)$$

$$= [U_{sm}\beta_x((U_{sm}-U_{gm}),\varepsilon,\rho_s)(U_{sm}-U_{gm})]^{n+1}(IJ)$$

$$+ [V_{sm}\beta_y((V_{sm}-V_{gm}),\varepsilon,\rho_s)(V_{sm}-V_{gm})]^{n+1}(IJ)$$

$$-POTSOL \equiv \varepsilon_s \rho_s V_s g = \rho_s g(\varepsilon_s V_{sm} g)^{n+1}(IJ) \qquad (5.39j)$$

The energy dissipation is then given by

$$\frac{dKE_s}{dt} = T1 + T2 + C1 + C2 + C3 + C4 - PUL - PVL - FRIC - POTSOL \qquad (5.40)$$

The rate of dissipation, $-dKE_s/dt$, should always be greater than or equal to zero.

We now consider the special cases of the derivatives in Eq. 5.39 for the six locations around an obstacle, such as that shown in Fig. 8. At present, three "flags" are used to keep track of whether the obstacle is above, below, or to the left of the cell under consideration. These flags are numbered as follows:

FLAG = 1: Obstacle surface above

FLAG = 2: Obstacle surface to the left

FLAG = 3: Obstacle surface below

A special subcase is a cell next to a line of symmetry; this applies to cells 1 and 5, which have a line of symmetry to their left. These flags will be extended in the future to handle additional cases of more than one obstacle surface associated with a cell and lines of symmetry to the right, top, and bottom. Only the expressions that differ from Eqs. 5.39a-5.39i are listed below.

FLAG = 1 (obstacle surface above)

To evaluate term C3, we finite-difference Eq. 5.39e over an interval, $\Delta y/2$, next to the obstacle and set the normal velocity on its solid surface to zero, because it is inpenetrable, to obtain

$$C3 = \rho_s(\varepsilon_s U_{sm} V_{sm})^{n+1}[0 - U_{sm}/(\Delta y/2)]^{n+1}(IJ) \qquad (5.39e')$$

Neither pressure nor void fraction are defined inside the obstacle. One way to evaluate the term PVL is to assume zero gradients of pressure and void fraction on the obstacle surface and to set P(IJT) equal to P(IJ) and ε_s(IJT) to ε_s(IJ) to obtain

$$\begin{aligned} - PVL = {} & (\varepsilon_s V_{sm})^{n+1}(IJ)[P(IJ)-P(IJB)]^{n+1}/2\Delta y \\ & -[G(\varepsilon)V_{sm}]^{n+1}(IJ)[\varepsilon(IJ) - \varepsilon(IJB)]^{n+1}/2\Delta y \end{aligned} \qquad (5.39h')$$

An alternative is to extrapolate the pressures and void fractions linearly, to obtain values on the obstacle surface and then to use this result to evaluate the gradients. This is equivalent to replacing $2\Delta y$ by Δy in Eq. 5.39h'.

Cells 1 and 5

These cells are next to a line of symmetry. In this case, some ambiguity arises concerning the approximation of term C4. One choice is to evaluate the gradient using the average value of the velocity in the right half and the zero gradient in the left half to obtain

$$C4 = \rho_s(\varepsilon_s U_{sm} V_{sm})^{n+1}(IJ)[V_{sm}(IJR) - V_{sm}(IJ)]^{n+1}/2\Delta x \qquad (5.39f')$$

Another choice is to assume zero gradient of axial velocity in the x direction in the left half of the cell and, therefore,

$$C4 = 0 \qquad (5.39f'')$$

The evaluation of the term PUL also gives rise to some ambiguity. One choice is to assume that both the pressure and the void fraction have zero gradient on the left half of the cell, so that P(IJL) is set equal to P(IJ) and ε_s(IJL) is set equal to ε_s(IJ) in Eq. 5.39g to obtain

$$\begin{aligned} - PUL = {} & (\varepsilon_s U_{sm})^{n+1}(IJ)[P(IJR) - P(IJ)]^{n+1}/2\Delta x \\ & [G(\varepsilon)U_{sm}]^{n+1}(IJ)[\varepsilon(IJR) - \varepsilon(IJ)]^{n+1}/(2\Delta x) \end{aligned} \qquad (5.39g')$$

Another possibility is to extrapolate linearly the pressures and void fractions to the line of symmetry, as was done to evaluate PVL. The result would be equivalent to setting $2\Delta x$ to Δx in Eq. 5.39g'.

FLAG = 2 (obstacle surface to the left)

The evaluation of this term is highly prone to inaccuracy, probably because of the very high velocity of axial solids near the obstacle surface, due to the neglect of the gas and solids shear terms. Hwang[90] observed, in his gas-particle calculations, that numerical instability can actually occur if the velocity of the particles is too high. Although hydrodynamic computations are stable, the kinetic energy dissipation may be underestimated (too negative). The term C4 is evaluated by averaging V_{sm} next to the obstacle and then finite-differencing over Δx to obtain

$$C4 = \rho_s(\varepsilon_s U_{sm} V_{sm})^{n+1}(IJ)[V_{sm}(IJ) + V_{sm}(IJR)]^{n+1}/2\Delta x \qquad (5.39f''')$$

Another possibility is to evaluate term C4 in a manner similar to that used with term C3 for FLAG = 1:

$$C4 = \rho_s(\varepsilon_s U_{sm} V_{sm})^{n+1}(IJ)[V_{sm}(IJ)-0]^{n+1}/(\Delta x/2) \qquad (5.39f'''')$$

The term PUL is treated the same as it was for FLAG = 1 for cell 1 (i.e., Eq. 5.39g' is used).

FLAG = 3 (obstacle surface below)

Term C3 is treated as was term C3 for FLAG = 1, except that the sign is changed:

$$C3 = \rho_s(\varepsilon_s U_{sm} V_{sm})^{n+1}[(U_{sm} - 0)/(\Delta y/2)]^{n+1}(IJ) \qquad (5.39e'')$$

The term PVL is evaluated analagously to the evaluation of the term PVL for FLAG = 1, to obtain

$$\begin{aligned} PVL = {} & (\varepsilon_s V_{sm})^{n+1}(IJ)[(P(IJT) - P(IJ)]^{n+1}/\Delta y \\ & - [G(\varepsilon)V_{sm}]^{n+1}(IJ)[\varepsilon(IJT) - \varepsilon(IJ)]^{n+1}/2\Delta y \end{aligned} \qquad (5.39h'')$$

or with $2\Delta y$ replaced by Δy.

The sum of the terms T1, T2, and C1-C4 represents the kinetic energy dissipation, dKE_{SPD}/dt, in the power dissipation model. The steady-state energy dissipation finite-difference equations are identical to the above.

5.2.4 Energy Dissipation Erosion Model

After the energy dissipation has been computed, it must be transformed into an erosion rate. This requires the choice of an erosion model. The one chosen for the preliminary calculations is given by

$$\dot{E}_{ED} = C\ (-dKE_s/dt)d_p/E_{sp} \tag{5.41}$$

where dKE_s/dt is given by Eq. 5.27 for time-dependent energy dissipation and by Eq. 5.37 (DIFFSC, DIFFSMX, and DIFFSMY set to zero) for time-averaged energy dissipation; d_p is the particle diameter and E_{sp} is the specific energy, which is a material property related to hardness, p. Some typical values of hardness are given in Table 3 for the materials used by Wood and Woodford[65] and in Table 4 for data from Ushimaru et al.,[82] who claim that $E_{sp} \approx 2 \times p$.

The energy dissipation erosion model given by Eq. 5.41 can be interpreted in either of two ways. It can be thought of as the extension of the power dissipation erosion model given by Eq. 5.10, with $V_f/A_t = d_p$, or as a generalization of Rittinger's law given by Eq. 5.19, but with no threshold energy. We chose C = 0.1 and E_{sp} = p; we call this the monolayer energy dissipation erosion model.

In their cold fluidized-bed erosion experiments, Wood and Woodford[68] found that the erosion rate increased with increasing particle diameter. For example, they obtained erosion rates of 0.036, 0.48, and 1.16 mm/1000 h for aluminum tubes for 100-, 930-, and 1900-μm silica sand; these values suggest a very nearly linear dependence. Basically linear dependence was found for all the other materials tested. Therefore, the choice of the particle size dependence in the energy dissipation erosion model given by Eq. 5.41. appears reasonable.

The boundary conditions used in the computations performed in this section are given by Eqs. 5.39e', 5.39h, 5.39f', 5.39g', 5.39f'", 5.39e", and 5.39h".

TABLE 3 Hardness of Materials Tested by Wood and Woodford

Material	Crystal Structure	Diamond Pyramid Hardness[a] (kgf/mm^2)	Composition
Aluminum	fcc	18.5	99.99% Al
Iron	bcc	90	Electrolytic Fe (99.95%)
Copper	fcc	104	OFHC Cu (99.99%)
Nickel	fcc	131	Ni 270 (99.95%)
Cobalt	fcc	210	Electrolytic Co (99.92%)
SA213-T11	bcc	177	0.1 C; 0.44 Mn; 0.65 Si; 1.22 Cr; 0.48 Mo;
SS304			18 Cr; 8 Ni; 1.7 Mn; 0.5 Si; 0.05 C.
SS316	fcc	171	17 Cr; 12 Ni; 1.7 Mn; 2.0 Mo; 0.5 Si; 0.05 C.
A 286	fcc	393	53 Fe; 26 Ni; 15 Cr; 1.3 Mo; 0.2 Al; 2.0 Ti; 1.35 Mn; 0.5 Si ;0.05 C; 0.01 SB
Stellite 6B	fcc	377	Co; 29.9 Cr; 2.2 Ni; 1.3 Fe; 1.0 Mo; 4.3 W; 0.48 Si; 1.61 Mn; 0.99 C.
High-speed Steel	bcc	1010	1.2 C; 3.75 Cr; 1.6 V; 2.75 W; 8 Mo; 8.25 Co.
Limestone (CaO)		134	
Silica Sand		766	
Alundum (Al_2O_3)		1890	

[a] 0.5-kg load.

Source: Ref. 65.

TABLE 4 Typical Values of Material Hardness

Metal	Hardness, P (kgf/mm^2)
Lead	5
Aluminum	22-35
Copper	42-120
Brass	42-180
Nickel	115-350
Hardened steel	900

Source: Ref. 82.

6 CALCULATION OF ENERGY DISSIPATION AROUND AND EROSION RATES OF AN OBSTACLE IN A TWO-DIMENSIONAL FLUIDIZED BED

Results of energy dissipation computed from the energy dissipation model are presented in this section. Both time-averaged and fluctuating results are included. The energy dissipation rates are compared with the kinetic energy available for the Finnie erosion model. This comparison is done on a consistent basis, using the monolayer energy dissipation erosion model. A methodology for the consistent and meaningful comparison of the energies is developed. The erosion rates are computed and compared. Because of lack of directly usable data for validation of the erosion models, the computed erosion rates are compared with published literature results obtained under similar operating conditions.

The computed void fraction, gas and solid phase velocity, and pressure fields were found to be relatively insensitive to (1) the parameters in the solids elastic modulus, G, and (2) the treatment of the pressure gradient term.[47] Therefore, only one representative set of time-averaged and one set of time-dependent FLUFIX hydrodynamics outputs were used to calculate the energy dissipations discussed in the next two sections. These results are for hydrodynamic model A, given by Eqs. 2.1-2.6, and elastic modulus model 1, given by

$$G(\varepsilon) = \exp\,[-600(\varepsilon - 0.376)] \tag{6.1}$$

as discussed in Sec. 2.1.

6.1 TIME-AVERAGED ENERGY DISSIPATION CALCULATIONS

Pressure, gas and solid velocity components, and void fraction time-averaged over a 2.0-s time scale are given in Fig. 18 for all the cells bordering the obstacle. The velocity components have been resolved at the cell centers by averaging the values at the cell edges. The dimensions of the obstacle, its location in the fluidized bed, and other details are given in Fig. 1.

The results show that the void fraction is high on the bottom and side and low on the top, where solids are settled. The gas and solids are accelerated around the obstacle with a gas velocity on the side approaching the jet velocity of 5.78 m/s. Plots of the entire time-averaged porosity and gas and solids velocity fields are shown in Figs. 10 and 13.

Using Eq. 5.37 with DIFFSC, DIFFSMX, and DIFFSMY set to zero and the time-averaged FLUFIX hydrodynamic ouputs, time-averaged energy dissipation was computed for the cells around the obstacle. The total energy dissipation, and all of its components are shown in Table 5. The units of erg/(s·cm^2) are consistent with the units of the FLUFIX hydrodynamic results. The # sign refers to the cell numbers around the obstacle. IJ is the number of the cell internal to the FLUFIX code. Also shown in the table are the energy dissipation rates for the lower and upper corner cells, IJ = 70 and 169, respectively.

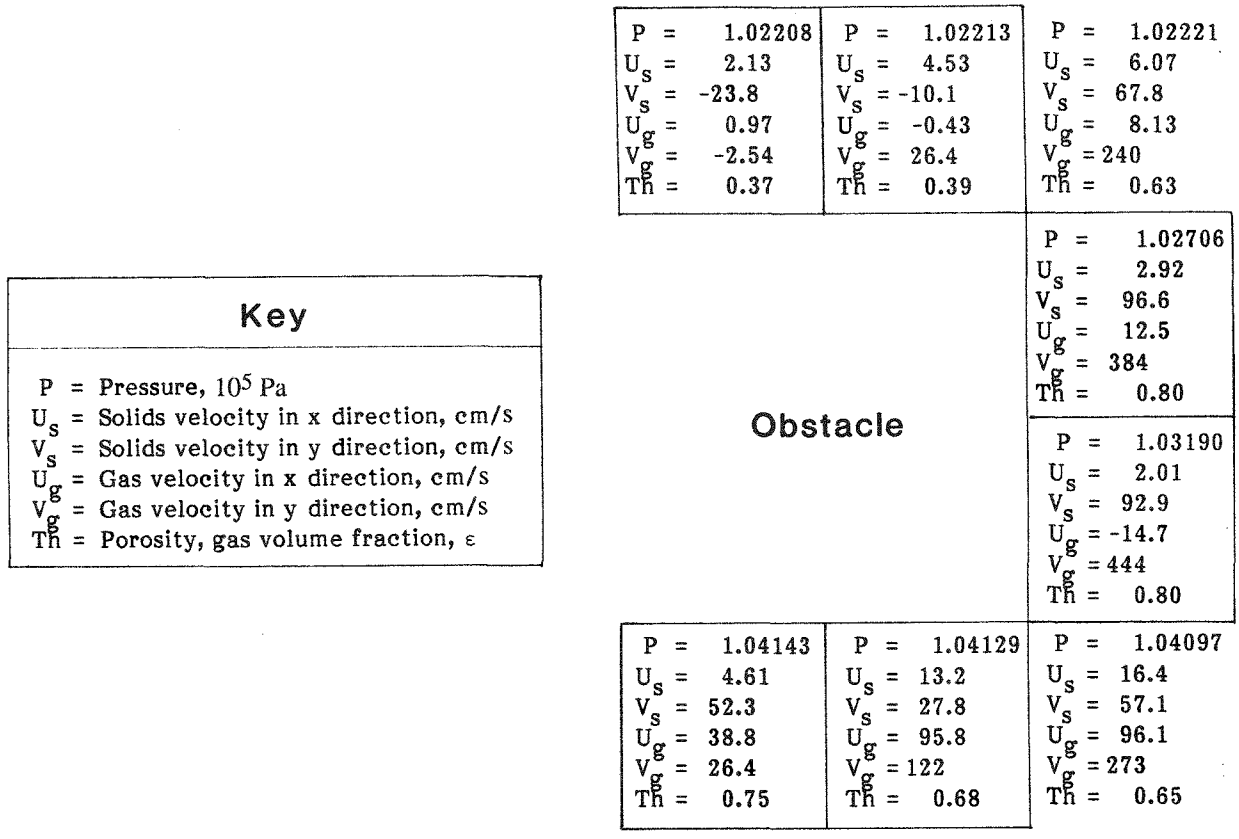

FIGURE 18 Time-Averaged Porosities, Velocities, and Pressures around an Immersed Obstacle — Hydrodynamic Model A, dp = 500 μm, V_{jet} = 5.78 m/s, $V_{secondary}$ = 0.26 m/s

SUM1, which is the sum of terms C1 through C4 given by Eqs. 5.39c through 5.39f, represents the kinetic energy dissipation, dKE_{sPD}/dt, which is obtained from the power dissipation model, Eq. 5.10a. The results for SUM1 clearly show why the power dissipation model is inadequate: some values are positive and some values are negative. All values should be negative so that the erosion rate would be positive. The reason for the sign variations can be seen by examining Figs. 13 or 18. The solids are being accelerated above the lower corner and decelerated near the upper corner. They are also decelerated below and above the obstacle. Hence, the reason for the sign variations and the unacceptability of the power dissipation erosion model. The results obtained by Usimaru et al.[82] were fortuitous, in that they had decelerating solids flow in their slurry jet pump model.

PTOT is the sum of PUL and PVL, given by Eqs. 5.39g and 5.39h. RESID is the sum of all the terms given by Eq. 5.40 (with T1 and T2 equal to zero) and represents the total energy dissipation. All these terms are negative, as they should be. The total time-averaged energy dissipation in SI units is tabulated in Table 6 for reference, where it is compared with the time average of the transient energy dissipation (calculated in Sec. 6.2, where the reason for the differences is discussed).

TABLE 5 Computed Time-Averaged Energy Dissipation, dKE_s/dt, and its Components in erg/(s·cm^2)

#	IJ	C1*	C2*	C3*	C4*	SUM1	PUL*	PVL*	PTOT	FRIC*	POTSOL*	RESID
1	68	188	-35529	-276	-2841	-38457	128	8949	9077	34262	-30998	-50798
2	69	1697	-6881	-1547	1078	-5653	1526	6187	7713	10642	-21320	-2688
-	70	-507	17773	1011	21832	40108	2626	32609	35236	68001	-47606	-15523
3	103	13	35065	-127	12795	47746	-30	26654	26624	113897	-44666	-48110
4	136	39	-31151	58	20032	-11023	17	19469	19486	82562	-46815	-66256
5	167	47	-8551	-68	-852	-9423	215	-8815	-8601	-6195	35958	-30586
6	168	26	-618	-125	-4873	-5590	-283	-2841	-3124	-4141	14504	-12829
-	169	134	-20939	-185	25585	4595	-98	24250	24151	57476	-59731	-17301

Note: to convert to W/cm^2, multiply by 10^{-7}.
# = Cell designations in Figure 19
IJ = Cell locations in Computer program
SUM 1 = C1 & C2 & C3 & C4
PTOT = PUL & PVL
RESID = Energy dissipation rate given by Eq. 5.40
* Terms are given is Eqs. 5.39c - 5.39f

We can compare the energy dissipated in the vicinity of the obstacle with the total energy dissipation in the bed, given by

$$E_v = [(AV)_{jet} + (AV)_{sec}] \varepsilon_s \rho_s g h \quad (6.2)$$

Equation 6.2, derived in App. C, states that the energy dissipated in the bed is equal to that required to support the bed weight, which is approximately the dissipation due to drag. Substituting a bed height of 0.28 m, Eq. 6.2 yields a total bed dissipation of 17.8 W for $\varepsilon_s = 0.4$, $\rho_s = 2.6$ g/m^3, and the bed conditions given in Sec. 2.2. From Table 6, the energy dissipated around half the obstacle is 21.13 x 10^{-3} W/cm^3, or an average of 3.5 x 10^{-5} W/cm^3 per cell. Assuming that this energy is dissipated in the monolayer of 0.05 cm, the total energy dissipated around the obstacle is 1.64 x 10^{-2} W. This is less than 0.1% of the total amount dissipated by frictional drag.

TABLE 6 Comparison of Time-Averaged Energy Dissipation and Time-Averaged Transient Energy Dissipation, $-dKE_s/dt$ (10^{-3} W/cm^3)

Cell* Number	Time-Averaged	Time-Averaged Transient
1	5.08	5.58
2	0.27	0.51
3	4.81	1.08
4	6.62	4.56
5	3.06	2.52
6	1.29	2.04
Total	21.13	16.29

*Locations given in Fig. 8

A simple methodology has been developed to compare, on a consistent basis, the computed results of the energy dissipation model with the kinetic energy available for algebraic erosion models. The Finnie erosion model is chosen to illustrate the methodology; its total available kinetic energy KE_{TOT}, is given by

$$KE_{TOT} = \dot{m}_s \vec{v}_s^{\,2}/2 \quad (6.3)$$

where KE_{TOT} has dimensions of W/m^2.

In order to compare the energy dissipation rate with the total kinetic energy defined by Eq. 6.3, the energy dissipation rate is multiplied by the particle diameter:

$$U_{ED} = (-dKE_s/dt)\, d_p \quad (6.4)$$

where U_{ED} also has dimensions of W/m^2. The particle diameter chosen is 500 μm, nominally the same as that used in the analysis of the IIT two-dimensional cold fluidized-bed experiment (see Sec. 2.2).

The maximum amount of the total kinetic energy available for erosion in the Finnie erosion model is given by

$$KE_{FM} = 0.075\ (\dot{m}_s \vec{v}_s^{\,2}/2) = 0.075\ KE_{TOT} \tag{6.5}$$

at an impingement angle of 18.43°. The kinetic energy available for erosion at any other angle is given by

$$KE_F = (1/8)\ \dot{m}_s \vec{v}_s^{\,2}\ f(\alpha) \tag{6.6}$$

where $f(\alpha)$ is given by Eq. 3.4.

The results computed from Eqs. 6.3-6.6 are summarized in Fig. 19 (expressed in W/cm^2) for the six cells surrounding the obstacle. The two corners have been suppressed, because the corners have no area. Also shown are the angles of the solid velocity vector with respect to each surface.

As Fig. 19 shows, the results from the monolayer energy dissipation model are very much lower than the total kinetic energy available for the Finnie model, $\frac{1}{2}\dot{m}_s v_s^2$. The monolayear energy dissipation model results are closer to those for the Finnie maximum model, which uses only 7.5% of the maximum kinetic energy. The spatial trend is basically the same.

The impingement angles are close to 90° on the very top and bottom; so very low available energies, KE_F, are computed with the Finnie model, Eq. 6.6. No available kinetic energy is computed on the top of the side, because the solids flow away from the obstacle.

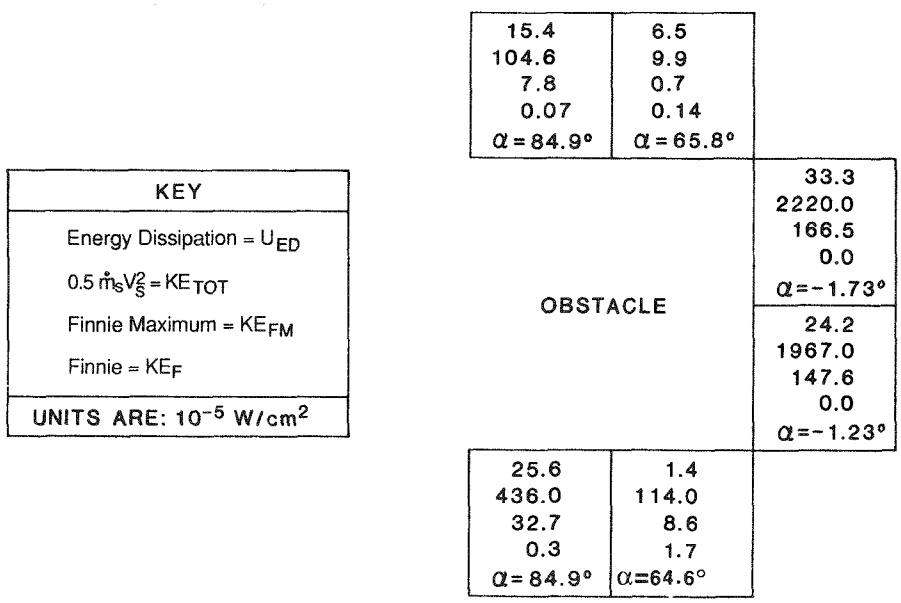

FIGURE 19 Time-Averaged Energy Dissipation, Calculated Results

6.2 TRANSIENT AND TIME-AVERAGED TRANSIENT ENERGY DISSIPATION CALCULATIONS

Fluctuating energy dissipation values around the obstacle were computed using Eq. 6.4. They are plotted for all six cells in Fig. 20, using a particle diameter, d_p = 0.05 cm. The time averages of the transient results for $-dKE_s/dt$, Eq. 6.4, are tabulated in Table 6, where they are compared with the time-averaged results. The two results generally compare favorably. The differences are probably caused by (1) the neglect of DIFFSC, DIFFMX, and DIFFSMY in Eq. 5.37, and (2) inaccurate evaluation of term C4 on the side of the obstacle. The sums of the two sets of results agree closely. This close agreement acts as a consistency check on the two sets of independent computations.

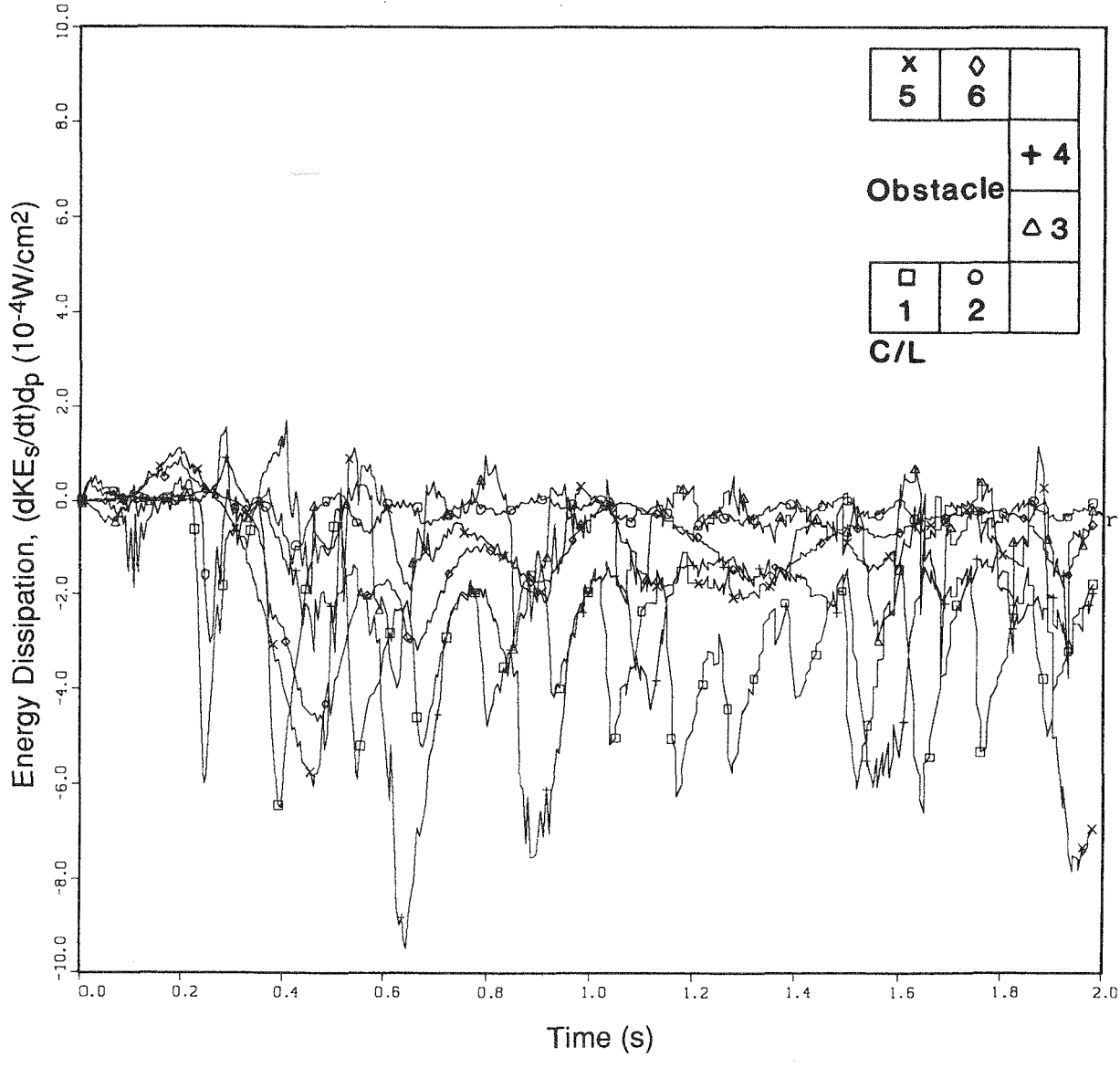

FIGURE 20 Fluctuating Energy Dissipation, Computed Results (dKE$_s$/dt) d$_p$ (d$_p$ = 500 μm)

A rough estimate of the accuracy of the fluctuating energy dissipation calculations can be obtained by the average of the occasional peaks of positive energy dissipation in Fig. 20, which is about 8 x 10^{-5} W/cm^2 (1.6 x 10^{-3} W/cm^3). The time average of the transient computations is believed to be inherently more accurate than the time-averaged computations.

Because it is difficult to follow all six curves in Fig. 20, the energy dissipation for only the two cells under the obstacle is replotted in Fig. 21. For cell 1, the figure clearly reveals the high frequency oscillations (9-10 Hz), which agree with the bubbling frequency observed in the high-speed motion picture study discussed in Sec. 2.2. The computed energy dissipation fluctuations closely follow the computed porosity fluctuations plotted in Fig. 8. Minima in the porosity fluctuations correspond to maxima in the energy dissipation. The fluctuating dissipated energy plotted in Fig. 21 differs from the erosion rate by only a factor of hardness, so the energy curves may be thought of as relative erosion rates. Hence, the erosion rate of cell 1 is much higher than that of cell 2. Erosion results will be presented and discussed in Sec. 6.3.

The passage of the bubbles and associated solids motion causing particles to strike the obstacle over tubes may be closely connected with the erosion process in fluidized beds. This concept has been put forward on an intuitive basis by Asai et al.[15] and Leckner et al.[91] Lockwood[92] attempted to make a connection between in-bed tube geometry and its effect on bubble growth, bubble size, and pressure fluctuations. Thus, so-called "high-quality fluidization" (i.e., smoother operating fluidized beds) may result in less erosion.

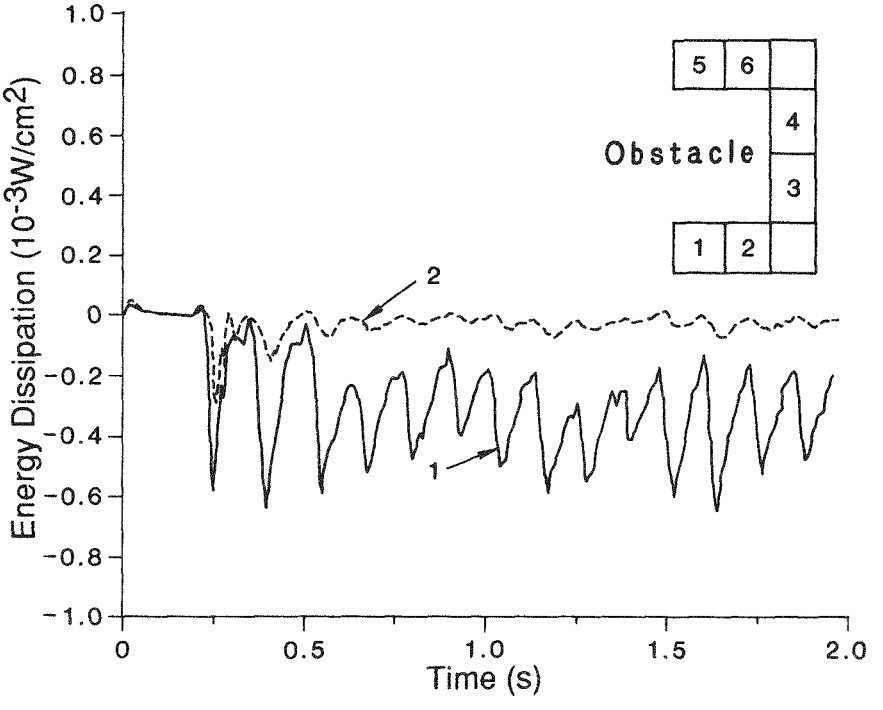

FIGURE 21 Fluctuating Energy Dissipation, Computed Results ($dKE_s/dt)d_p$, for Cells 1 and 2 (d_p = 500 μm)

A breakdown of the component contributions to the total energy dissipation for cell 1 is given in Fig. 22. The breakdown is analogous to that done in Table 5 for the time-averaged computations. For clarity, only the major contributions are plotted. Here, T1 and T2 represent term 1 in Eq. 5.25 and are given by Eqs. 5.39a and 5.39b. Although the sum of these terms shows strong oscillations, it oscillates around zero. SUM1 represents term 2 in Eq. 5.25 and is the sum of terms C1 through C4 given by Eqs. 5.39, etc. This term is negative, because the solids decelerate as they approach the lower surface of the obstacle. The terms PTOT and FRIC are both positive; when they are subtracted, in Eq. 5.40, they become dissipative. -(PTOT + FRIC) represent terms 4 and 3 + 5, respectively, in Eq. 5.25. The last term, POTSOL, is negative. When it is subtracted, in Eq. 5.40, it becomes positive, because it represents a gain in potential energy. -POTSOL represents term 6 in Eq. 5.25. The time average of these various terms is close to the values given in Table 5. The sum of the time average of all the terms is given in Table 6.

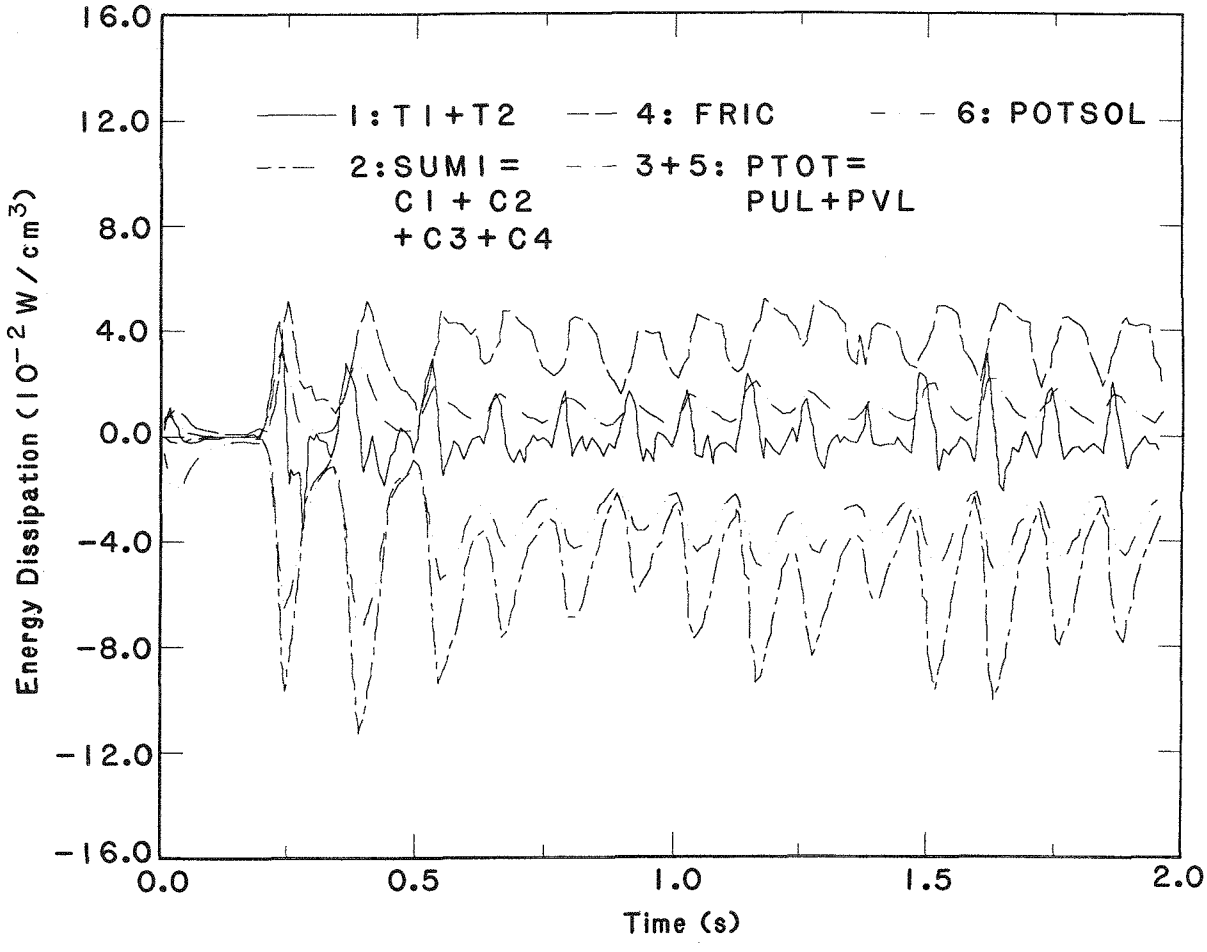

FIGURE 22 Breakdown of the Five Main Terms of the Transient Energy Dissipation, dKE_s/dt (the numbers refer to the terms in Eq. 5.25)

The maximum kinetic energy available for the Finnie erosion model, given by Eq. 6.3, is plotted in Fig. 23 for the six cells surrounding the obstacle. Once again, the high-frequency oscillations at cell 1 are clearly seen. Note the lower-frequency but higher-amplitude kinetic energy oscillations on the side of the obstacle. The maximum amount of kinetic energy available for the Finnie erosion model, KEFM, is only 7.5% at 18.43°, given by Eq. 6.5.

The amount of effective (erosion producing) kinetic energy available for erosion at any other angle, KE_F, given by Eq. 6.6 is plotted in Fig. 24. Very small kinetic energies are calculated for cells 1 and 5, because the solids impingement in these regions is almost normal to the obstacle surface. Larger rates are computed at cells 2 and 3, becuase the impingement angle are closer to 18.43°. The large spikes are caused by changes in the solids flow direction at cell 3. These spike tops are cut off in order that the variation in the other five cells can be seen more clearly. The maximum values of the three cut-off peaks in Fig. 24 are 80, 40, and 15 x 10^{-5} W/cm^2, respectively.

The transient calculations for Eqs. 6.3-6.6, time-averaged over 2 s, are tabulated in Fig. 25. Comparison of these results with those for Fig. 19 shows that the time-averaged energy and time-averaged transient maximum kinetic energy, 0.5 $\dot{m}_s V_s^2$,

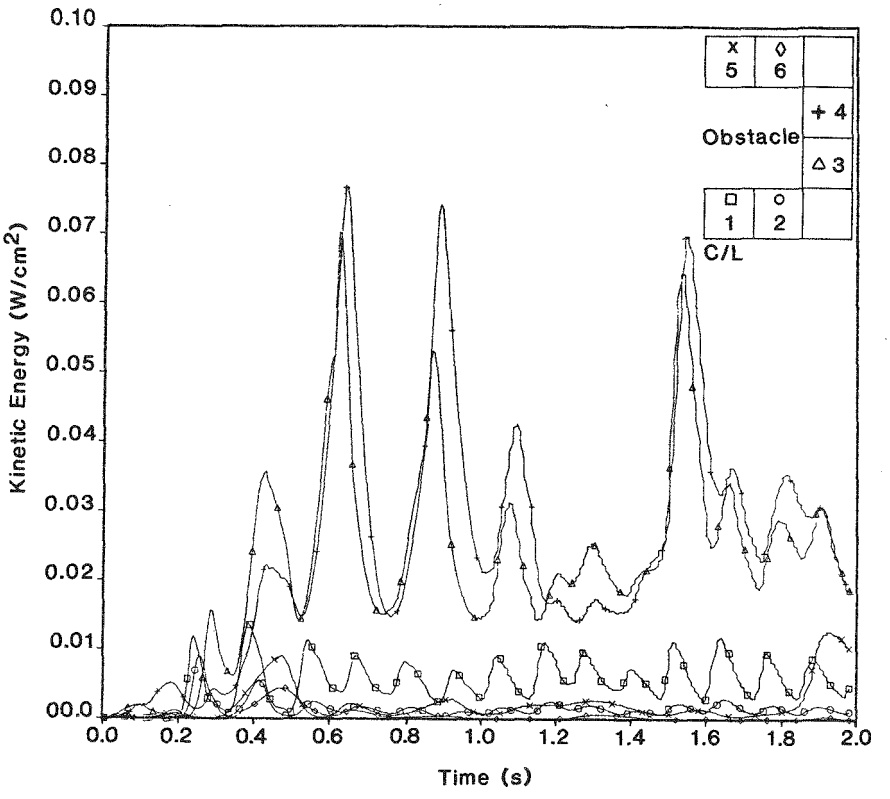

FIGURE 23 Total Kinetic Energy Available for Finnie Erosion Model

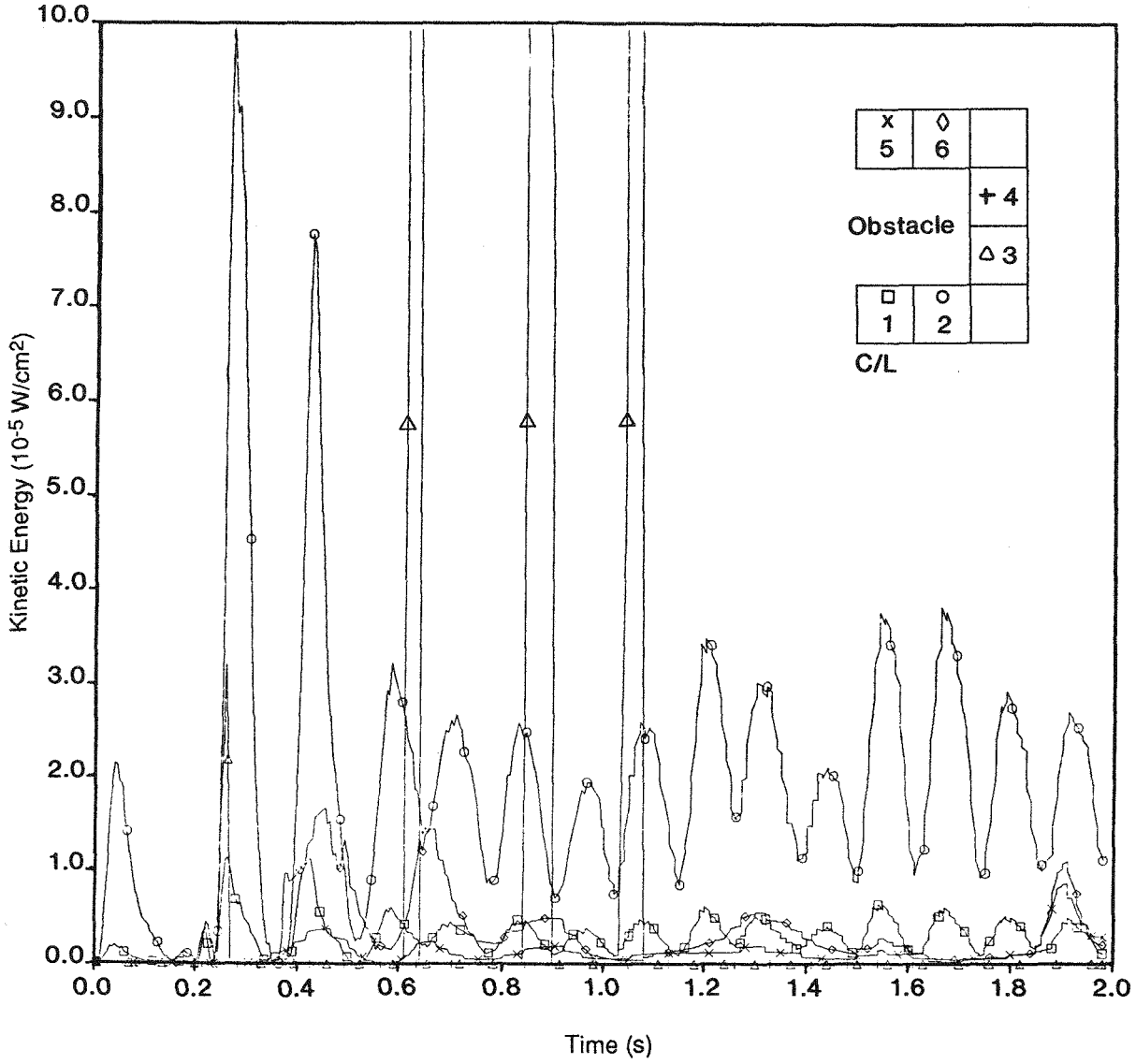

FIGURE 24 Kinetic Energy Available for Finnie Erosion Model with Angular Dependence

are not equal; the latter are consistently larger. If we time-average this transient kinetic energy, we obtain

$$\langle \dot{m}_s \vec{v}_s^{\,2} \rangle = \rho_s \langle \varepsilon_s \vec{v}_s^{\,3} \rangle = \rho_s \langle \varepsilon_s \rangle \langle \vec{v}_s \rangle^3 + \rho_s \langle \varepsilon_s' \vec{v}_s'^{\,3} \rangle \qquad (6.7)$$

because ρ_s is constant. The time-averaged maximum kinetic energy was obtained by using the time-averaged porosity and solids density, neglecting the time average of the

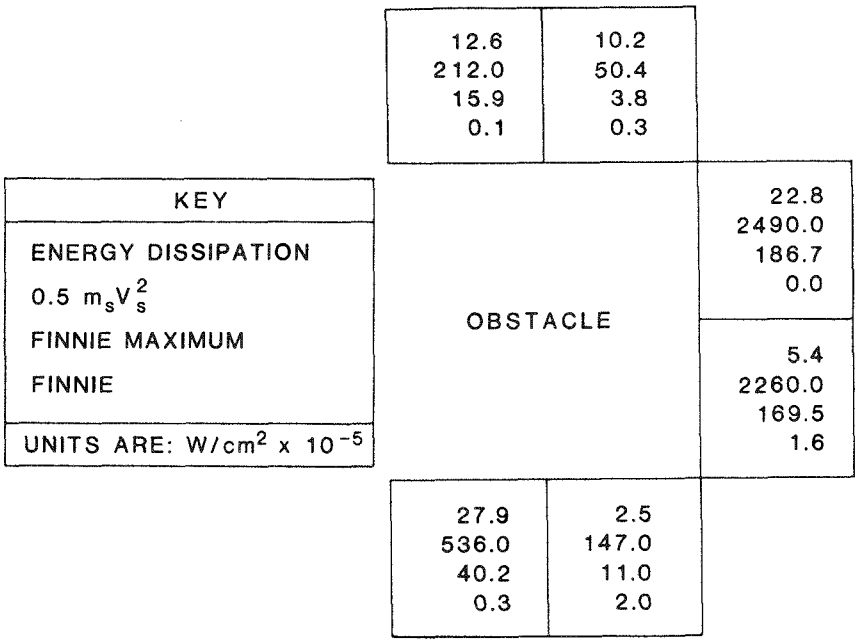

FIGURE 25 Time-Averaged Transient Energy Dissipation, Calculated Results (d_p = 500 μm)

product of the fluctuations. Comparison of the two sets of calculations allows us to quantify the magnitude of the error incurred.

The time averages of the transient energy dissipation calculations are not always higher than the time-averaged values. The difference, however, is within the estimated error in the calculations ($\pm 8 \times 10^{-5}$ W/cm^2). This type of inaccuracy does not exist with the calculations of kinetic energy. The time-averaged and time-averaged transient values of the kinetic energy available at any angle are close, but they differ for the reasons discussed for the maximum available kinetic energy.

6.3 EROSION RATE CALCULATIONS

The time average of the transient energy dissipation computations is believed to be inherently more accurate than the time-averaged computations. Only the former were used to calculate the erosion rates.

The energy dissipation rates shown in Fig. 25 were converted to erosion rates for aluminum. The hardness used was 30 kgf/mm^2 (294 MN/m^2). This value is the average of the range quoted by Ushimaru et al.[82]. The results are displayed in Fig. 26. The transient erosion rates are shown in Fig. 27. These are, to our knowledge, the first computations of local erosion rates in fluidized beds. In calculating the erosion rates for the monolayer energy dissipation erosion model, we applied the empiricism that, when metal is removed, fewer than 10% of the grains in contact with the surface actually remove metal. (The remaining particles cause only elastic deformation, not resulting in

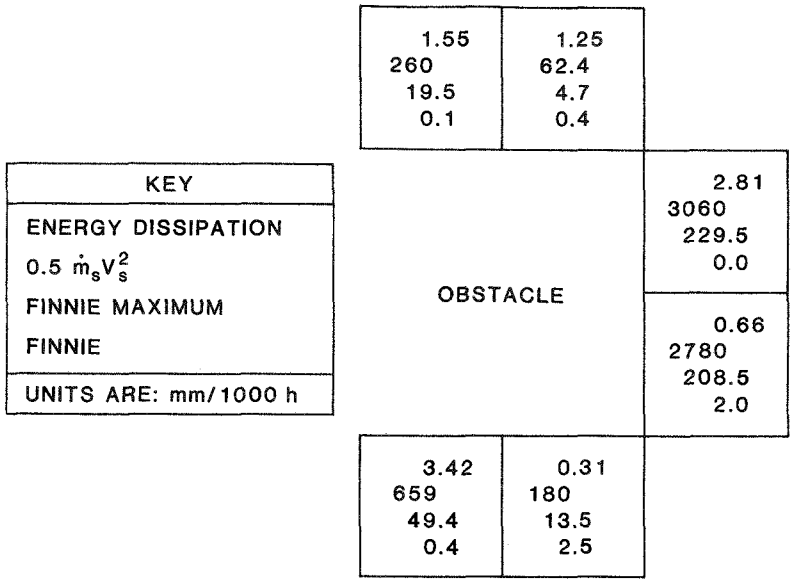

FIGURE 26 Time-Averaged Transient Calculated Erosion Rates for Aluminum, Hardness = 30 kgf/mm^2 (294 MN/m^2), d_p = 500 μm

material wear.[87]) Clearly, this proportion is influenced by the hardness of the erodent relative to the eroding surface and the erosion mechanism, cutting tool (impaction) or sandpaper (abrasion). This factor of 10% may be justified when the hardness of the particle is comparable with that of the wall over a fairly wide range, but it is not on a strong theoretical foundation; its value, or a model for it, should be investigated further. It is not the purpose of this study to investigate materials property models, but rather to develop a best-estimate mechanistic erosion model that incorporates the state of present knowledge of material properties and the results of hydrodynamic modeling.

The erosion rates computed from the monolayer energy dissipation erosion model fall between those for the Finnie maximum erosion model, Eq. 6.5, and the Finnie erosion model with angular dependence, Eq. 6.6, for cells, 1,4,5, and 6 and below for cells 2 and 3.

Because the bottom of the obstacle is located directly above the jet, the erosion rate is higher there than on the side or top. The spatial variation in the erosion rates computed from the monolayer energy dissipation erosion model basically follow those calculated from the Finnie maximum erosion model. However, the erosion rates computed from the monlayer energy dissipation erosion model are supsected to be too high at the top of the obstacle, because experimental evidence shows that predicted solids loading are too high.[47]

Time-averaged erosion rates computed from the Finnie maximum erosion model are large on the sides of the obstacle (cells 3 and 4), because solids velocities are important there. These erosion rates are of the order of 200 mm/1000 h, which are much too high for wear of aluminum by glass beads. The upper bound on tube erosion rates

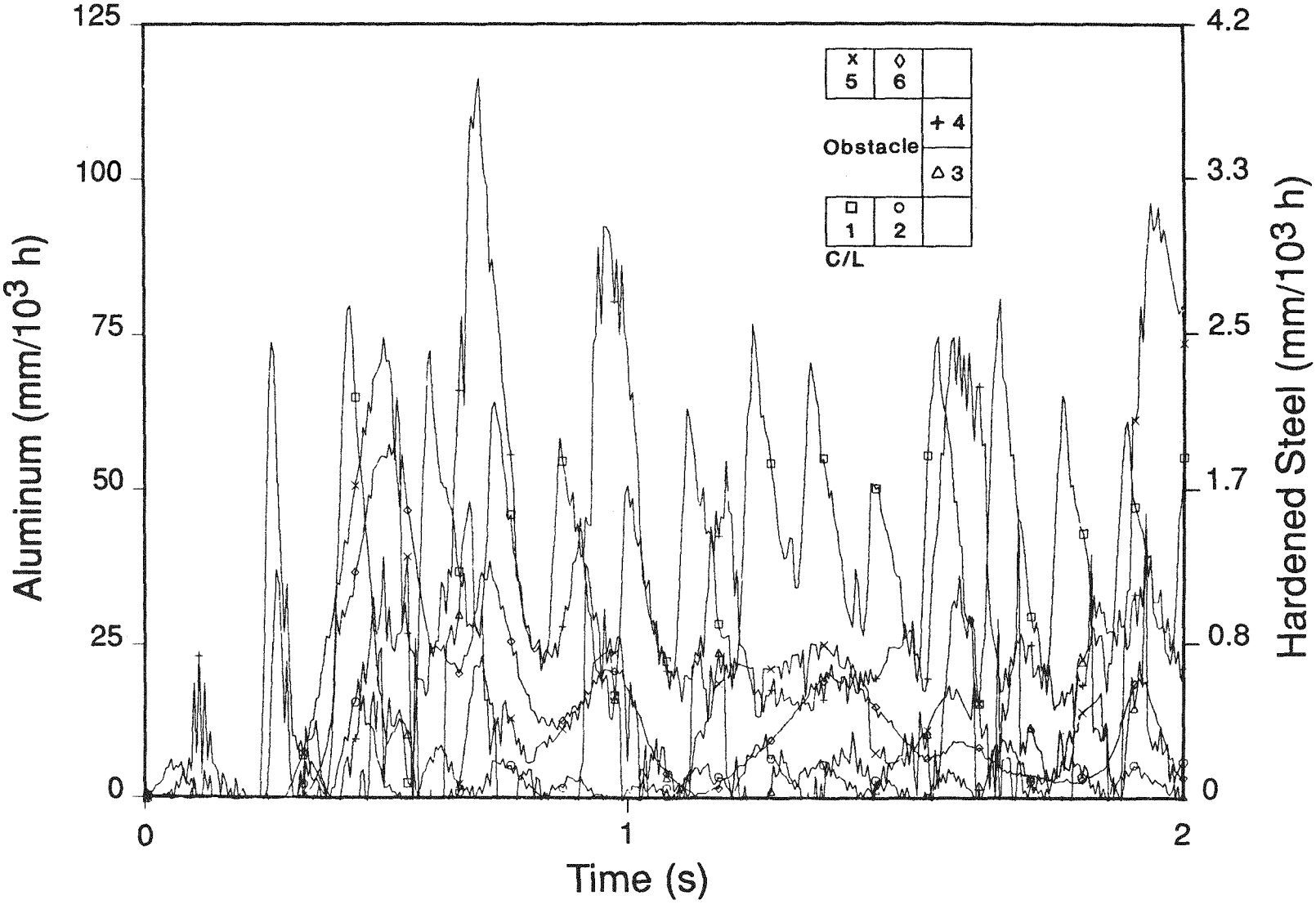

FIGURE 27 Fluctuating Erosion Rates Calculated from the Energy Dissipation Erosion Model for Aluminum and Hardened Steel (d_p = 500 μm)

given by Eq. 6.5, represents the maximum percentage of the total kinetic energy available for erosion, but only part of this energy is actually used in eroding the target.

Finnie's erosion model with the angular dependence, Eq. 6.6, is basically a cutting tool model, hence, it fails to predict both normal impaction erosion wear (cells 1 and 5) and abrasive erosion wear that occurs on the lateral sides of the obstacle (cells 3 and 4). Finnie's model predicts zero erosion rate for cell 4. In this cell, the solids flow tends to be deflected away by the obstacle and, under these conditions, Finnie's model does not predict any tube wear.

The experimental fluidized-bed tube wear data of Wood and Woodford[65] and Parkinson et al.[93] indicate that the erosion rate of aluminum is about 0.3 mm/1000 h for bed material consisting of silica sand. The erosion rate of 0.3 mm/1000 h for the Wood and Woodford data was deduced for 500-μm particles by linearly interpolating the data taken over a particle size range of 100 to 1900 μm. The fluidizing velocity varied from 1.5 to 3.6 m/s.

The erosion rate of approximately 0.3 mm/1000 h for the data of Parkinson et al.[93] was obtained for bare aluminum alloy (RTZ HE 30) tubes. This rate was the average for Run 1, which had a bed material consisting of an equal mixture of 1-2-mm and 0.5-mm silica sand of mean surface diameter 0.86 mm (860 μm) and a fluidizing velocity of 2 m/s. The maximum erosion rate on any tube was approximately 1 mm/1000 h. The agreement of this erosion rate with Wood and Woodford's results[65] may be fortuitous. The aluminum alloy was probably harder (not reported), and the average particle diameter was larger. Considering the many differences between the experiments, the agreement is remarkable.

The average calculated erosion rate of 0.9 mm/1000h from the Finnie erosion model with angular dependence seems to agree more closely with the experimental data than those of the monolayer energy dissipation erosion model (1.6 mm/100 h). This order-of magnitude agreement may be fortuitous, or it may occur because the average computed gas velocity next to the obstacle ≈4 m/s is close to the average interstitial gas velocity of the experiments, ≈4 m/s, at an assumed fluidized-bed porosity of ≈0.5.

The transient erosion rates for hardened steel are plotted in Fig. 27. The hardness used was 900 kgf/mm^2 (8.8 x 10^3 MN/m^2) from Table 4. The time-averaged values of the transient erosion rates are displayed in Fig. 28. Because these rates differ from aluminum erosion rates by a factor of 30, the same comments apply as those made above in regard to the comparison of the energy dissipation rates from the energy dissipation and Finnie erosion models. The experimental data of Wood and Woodford indicate an erosion rate of 0.015 mm/ 1000 h for 316 stainless steel for bed material consisting of 500-μm silica sand and fluidizing velocity in the range of 1.5 to 3.6 m/s. Considering the many geometrical differences, the order-of-magnitude agreement is encouraging.

Other erosion data help to place our computed erosion rates in perspective. Using α-Al_2O_3 with an average particle size of 2.5 μm and a loading of 1270 ppm at 700°C, an FeCrAlY-coated pin of IN 738 eroded at a rate of approximately 40 mm/100 h

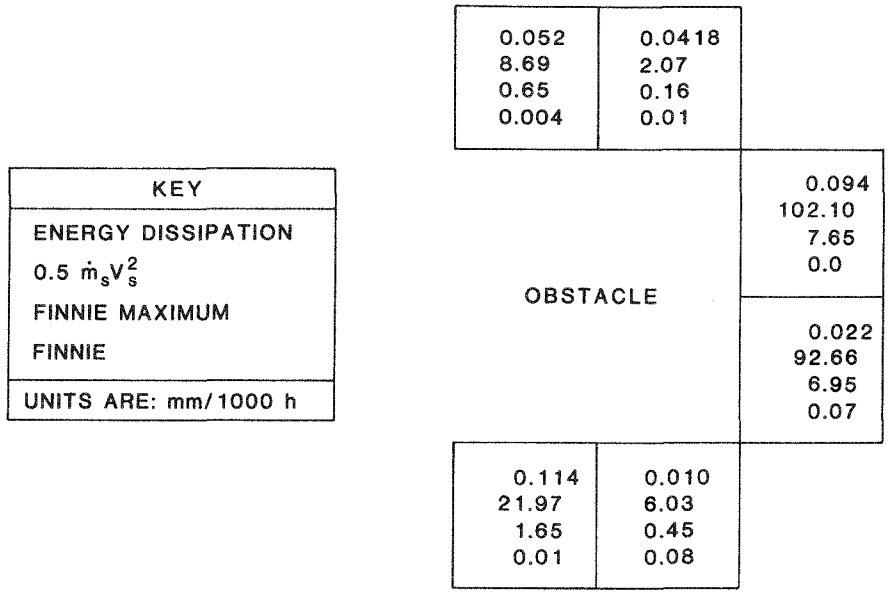

FIGURE 28 Time-Averaged Transient Calculated Erosion Rates for Hardened Steel, Hardness = 900 kgf/mm^2 (8.8 x 10^3 MN/m^2), d_p = 500 μm

a combustion gas velocity of 345 m/s.[94] Grimethorpe reported erosion rates of 2.5 mm/1000 h for the tube bank "C" 9 and about 10 mm/1000 h above the bed material injection port, located about 0.5 m from the bottom row of tubes;[95] the jet velocity was 50-80 m/s.

The superficial gas fluidizing velocity was 1.9 m/s, so the average interstitial gas velocity is again near 4 m/s, close to that next to the obstacle. The average particle size was approximately 1000 μm (dolomite). Several uncertainties exist in the comparison:

- The hardness of the tubes at 800-900°C in Grimethorpe may be much less than that of hardened steel at room temperature qiven in Table 4 and used in the erosion calculations.

- The hardness of dolomite is less than that of silica sand, but Wood and Woodford[65] found no significant difference in the erosion rates of these two materials at the same particle size.

This same report referred to inferred erosion rates of DeCoursin,[96] 2-10 mm/h near a 2-mm jet in an air distributor cap in an AFBC having a comparable velocity. Severe erosive wear of the Grimethorpe bed material injection port deflector plate was reported; in practice, it may have to be replaced at frequent intervals, or a more resistant deflector system will have to be developed. Research was reported in progress at Babcock & Wilcox.

Vaux and Newby[97] report erosion rates of from about 0.0001 to 0.1 cm/min for 304 stainless steel tubing subject to a 1.17-mm diameter, 320-m/s steam jet in a fluidized bed composed of 75-μm MgO, 88-mm nickel, and 72-μm iron powder for tube

spacings of 1-28 cm. At a tube spacing of 10 cm, the penetration rate of the 304 SS tube in the 72-μm iron powder fluidized bed is about 0.1 cm/min. This is the distance from the jet inlet to the bottom of the rectangular object. Assuming that the erosion rate is roughly proportional to the square of the jet velocity at such close spacings, we estimate an erosion rate of about 20 mm/1000 h at a jet velocity of 5.78 m/s.

Large-diameter particles erode faster than small-diameter particles. For example, Wood and Woodford[65] found that high-speed steel was eroded about five times as fast with 1.0-mm silica sand as with 0.1-mm sand. Finally, Ushimaru et al.[82] used their power dissipation model to compute a maximum erosion rate of about 1 mm/100 h, which agreed well with data for a conventional slurry jet pump. The angle of approach of the particles at roughly 50-m/s was near zero.

7 CONCLUSIONS AND RECOMMENDATIONS

A summary of the hydrodynamic calculations for a rectangular two-dimensional fluidized bed containing an obstacle showed good agreement with the limited experimental data. The bubble frequencies of approximately 4 Hz around and 9-10 Hz under the obstacle and the size of the first bubble agree reasonably well with the results of a high-speed motion picture study. The time-averaged porosity distribution also agrees reasonably well with data taken with a gamma-ray densitometer. The computed results are relatively insensitive to the hydrodynamic model and solids elastic modulus parameter.

A critique of six erosion models from the literature was performed. They were shown to have various flaws. For example, Finnie's model predicts no erosion at 0 and 90°. None of the erosion models includes hydrodynamic parameters. A methodology was developed to use these models with the hydrodynamic outputs of the FLUFIX computer program.

The energy dissipation model was developed, and was shown to generalize the so-called power dissipation model developed for low-angle erosion caused by slurries. The basis for the model was shown to be both ball-mill grinding and abrasive-wear laws. By generalizing these laws to multiple dimensions, it was possible to include impaction effects as well. Thus, it was possible to show that impaction and abrasion erosion are basically governed by the same mechanism: the imparting of the force of the particle stream to the eroding material surface or, alternatively, the transfer of a portion of the particle energy to the same surface. The monolayer energy dissipation model was adopted for the preliminary computations.

A methodology was developed to compare the energies available to the Finnie and monolayer energy dissipation models. Both time-averaged computations and time-averaged transient computations were performed using the hydrodynamic outputs of the FLUFIX code for a two-dimensional, cold fluidized bed containing a rectangular obstacle. The results of the latter computations are believed to be inherently more accurate; they are reasonably close, and act as a cross-check on the two independent computations. To our knowledge, these are the first such calculations of their kind. Differences are believed to result from neglecting the cross-correlation terms in the time-averaged energy dissipation model, as well as from inaccuracies in evaluating derivatives at the boundary of the obstacle. The power dissipation model was found to be inadequate. The energy dissipation rates computed from the energy dissipation model are closer to the maximum available from the Finnie model than from the Finnie model with angular dependence. If the results of the energy dissipation model were multiplied by 10%, to account for the empiricism that indicates that not all the grains in contact with the surface remove metal, the results would generally lie between those from the former two models. The variation of the erosion rate around the obstacle differs from that of the Finnie model with angular dependence.

Because of lack of directly useful erosion data to validate the erosion calculations, the results were compared with available literature erosion data taken in cold fluidized beds and found to agree within an order of magnitude. The Finnie model

with angular dependence would appear to agree better with the data. However, if the 10% factor is applied, the results of the energy dissipation model agree to within the same order of magnitude. Comparison with other, nonfluidized-bed erosion experiments helped place the computations in perspective further.

It is concluded that, in order to validate the models, properly a single-obstacle erosion experiment must be performed. The material property relationships also need to be extended to include, for example, attrition of the particles and realistic stress-strain relationships.

NOMENCLATURE

A	Area, m^2
C	$c/(\psi k)$
C'	Constant given by Eq. 3.10a, $(s^{5/2}m^{1/2})/kg$
C_b, C_d	Correction factors for nonsphericity
C_e	Erosion constant defined by Eq. 3.15c
c	Compaction modulus; nondimensional constant in Finnie's erosion model, Eq. 3.1, to allow for nonideal model particle behavior ($0 < c \leq 1$)
c_p	Particle concentration, kg/m^3
d_p	Particle diameter, m
dKE_s/dt	Energy dissipation rate as defined by Eq. 5.25 = e_{vs}, W/m^3
$\dot{E}$	Erosion rate, m/s
$\dot{E}_b, \dot{E}_d$	Brittle and ductile erosion rates, m/s
$\dot{E}_{FM}$	Maximum erosion rate from Finnie's model given by Eq. 3.5, m/s
E_p, E_t	Young's modulus of particle and target, respectively, Pa
E_{pd}	Power dissipation erosion rate given by Eq. 15.9
E_r	Reduced Young's modulus of elasticity given by Eq. 3.8, Pa
E_{sp}	Specific energy of eroding material (related to hardness), Pa
e_v	Rate of kinetic energy dissipation per unit volume, W/m^3
F	Force, N
f	Coefficient of friction
G	Solids elastic modulus, Pa
H	Hardness, Pa
k_p, k_t	Elastic constants defined by Eq. 3.7b = $(1 - \gamma_p^2)/(\pi E_p)$ and $(1 - \gamma_t^2)/(\pi E_t)$ respectively, Pa^{-1}
K	Ratio of vertical to horizontal forces in Finnie's erosion model, Eq. 3.1

K_d^*	Dimensionless erosion resistance given by Eq. 3.17a
K_1	Constant given by Eq. 3.10b, $(m/s)^{1/2}$
g	Acceleration due to gravity, m/s^2
M	Mass of abrasive particles, kg
$\dot{m}_s$	Mass flux of solids = $\varepsilon_s \rho_s \lvert \vec{v}_s \rvert$, $kg/(m^2 \cdot s)$
N_f	Number of cycles to failure
$\dot{N}$	Impaction frequency, s^{-1}
N_{IM}	Impact number given by Eq. 3.17b
P	Pressure, Pa; Power dissipation defined by Eq. 5.7, W/m^2
p	Eroding surface flow stress related to hardness, Pa
$\vec{q}_s$	Particle flux = $(1 - \varepsilon)\rho_s \vec{v}_s \Delta$
R_p	Particle radius, m
r^*	Ratio of rebound to approach velocity, V_2/V_1
S	Specific erosion rate given by Eq. 3.27, dimensionless
S_p	Moh's scale hardness of particles, Pa
S_s	Brinell Hardness, Pa
t	Time, s
U	Energy, J
U_g, U_s	Gas and solid phase velocities in the x direction, respectively, m/s
U_p	Velocity of abrasive particles, m/s
V	Velocity, m/s; Volume, m^3
V_c	Crater volume, m^3
V_g, V_s	Gas and solid phase velocities in the y direction, respectively, m/s
V_{el}	Threshold velocity defined by Eq. 3.8, m/s

V_p Threshold velocity defined by Eq. 3.12

V_1, V_2 Approach and rebound velocities, respectively, m/s

$\vec{v}$ Velocity vector, m/s

$|\vec{v}|$ Magnitude of velocity vector, m/s

v_r Relative velocity = $v_f - v_p$, m

W Volume of eroding surface, removed, m^3

W_b Volume of eroding surface removed by deformation (brittle) erosion, m^3

W_d Volume of eroding surface removed by cutting (ductile) erosion, m^3

x Lateral coordinate, m

y Axial coordinate, m

Greek Letters

α Impingement angle, degrees

α_o Transitor Impingement angle, degrees

β_x, β_y Fluid-particle friction coefficient in the x- and y-directions, respectively, $kg/(m^3 \cdot s)$

γ_p, γ_t Poisson's ratio of particle and target, respectively

Δ Layer thickness = (V_f/A_t)

δ Viscous boundary layer thickness; thickness of layer removed, m

ε Gas volume fraction

ε_b Deformation wear factor, Pa

ε_f Tensile stress at failure

ε_s Solids volume fraction = $1 - \varepsilon$

ε^* Compaction gas volume fraction

$\varepsilon_b, \varepsilon_d$ Energy to remove a given volume of target material for brittle and ductile erosion, respectively, J/m^3 or Pa

η_b, η_d	Mechanical efficiency of impact for brittle and ductile erosion, respectively
σ_b, σ_d	Yield strength for brittle and ductile erosion, respectively, Pa
σ_f	Tensile strength at failure, Pa
σ_y	Elastic load limit, Pa
τ	Solids stress, related to particle-to-particle pressure, Pa
$\overline{\overline{\tau}}_{sv}$	Solids viscous stress, Pa
ρ	Density, kg/m^3
ρ_f, ρ_p	Fluid and particle densities, respectively, kg/m^3
ρ_s, ρ_g	Solid and gas phase densities, respectively, kg/m^3
ψ	Ratio of depth of contact to depth of cut in Finnie's erosion model, Eq. 3.1
ϕ	Cutting wear factor, Pa
μ_f	Fluid viscosity, $Pa \cdot s$

Subscripts

b	Brittle
d	Ductile
f	Fluid
F	Finnie
FM	Finnie maximum
g	Gas
p	Particle
s	Solids
ss	Steady state
t	Target
x	x-direction coordinate

y	y-direction coordinate

Superscripts

.	Denotes time rate of change
$\rightarrow$	Denotes a vector quantity
=	Denotes a tensor quantity
n,n+1	Time levels $n\Delta t$ and $(n+1)\Delta t$, respectively

Operators

$\frac{d}{dt^s}$	Total derivative following the solids = $\frac{\partial}{\partial t} + \vec{v}_s \cdot \nabla$
$\nabla\cdot$	Divergence
∇	Gradient
<>	Time average

REFERENCES

1. Erlich, S., *Fluidized Combustion — Is It Achieving Its Promise?*, Conference Preprints, Third International Fluidized Combustion Conference, The Institute of Energy, London Vol. 2, pp. KA/1/1-KA/1/29, (Oct. 1984).

2. Wright, S.J., *Combustion of Coal in Fluidized Beds*, Physics in Technology, *8*:244-248 (Nov. 1977).

3. Beer, J.M., *The Fluidized Combustion of Coal*, Sixteenth Symposium (International) on Combustion, The Combustion Institute, Pittsburgh, pp. 439-460, (1976).

4. Fennelly, P.F., *Fluidized Bed Combustion*, American Scientist, *72*:254-261 (1984).

5. Schwieger, R., *Fluidized-Bed Boilers Achieve Commercial Status Worldwide*, Power, *129*(2):S1-S16 (Feb. 1985).

6. Krishnan, R.P., C.S. Daw, and J.E. Jones, Jr., *A Review of Fluidized Bed Combustion Technology in the United States*, in Heat and Mass Transfer in Fixed and Fluidized Beds, W.P.M. van Swaaij and N.H. Afgan, eds., Hemisphere Publishing Corp., Washington, D.C., pp. 433-455 (1985).

7. NCB (IEA Grimethorpe) Ltd., *Overall Project Review*, Grimethorpe, Barnsley, U.K. (May 1985).

8. Stringer, J., and I. Wright, *Overview of In-Bed Erosion in Fluidized-Bed Combustors*, in Materials and Components in Fossil Energy Applications, U.S. Department of Energy Report DOE/FE-0054/54 (Feb. 1, 1985).

9. NCB (IEA Grimethorpe) Ltd., *Incident Report Tube Bank 'C' -Metal Wastage Status Report - November 1982*, U.S. Department of Energy Report DOE/METC-83-54 (DE83008239) (Nov. 1982).

10. Kobro, H., *Discussion of the Operation and Performance of a 2.5 MW Fast Fluidized Bed Combustor and a 16 MW Bubbling Bed Combustor*, Conf. Preprints, Third International Fluidized Combustion Conf., The Institute of Energy, London, Vol. 1, pp. DISC/14/110-DISC/14/120, (Oct. 1984).

11. Xu-Yi, Z., *The Progress of Fluidized-Bed Boilers in People's Republic of China*, Proc. Sixth International Conf. on Fluidized Bed Combustion, U.S. Department of Energy Report CONF-800428, Vol. 1, pp. 36-40 (Aug. 1980).

12. Stringer, J., and I. Wright, *Materials Issues in Fluidized Bed Combustion*, presented at ASM Conf. on Materials for Future Energy Systems, Washington, D.C. (May 1984) [Reference 8 is an abstract of this paper.]

13. LaNauze, R.D., *Fundamentals of Coal Combustion in Fluidized Beds*, Chemical Engineering Research Design, *63*:3-33 (1985).

14. Muroyama, K., and L.S. Fan, *Fundamentals of Gas-Liquid-Solid Fluidization*, AIChE J., *31*(1):1-34 (1985).

15. Asai, M., K. Aohi, and S. Tsuji, *Particle Behavior in the Vicinity of Tubes in Fluidized-Bed Boiler*, Conf. Preprints, Third International Fluidized Combustion Conf. The Institute of Energy, London, Vol. 1, pp. DISC/1/1-DISC/1/8 (Oct. 1984).

16. Jansson, S.A., *Erosion and Erosion-Corrosion in Fluidized Bed Combustor Systems*, Proc. Corrosion-Erosion-Wear of Materials in Emerging Fossil Energy Systems, A.V. Levy, ed., National Assm. of Corrosion Assn. Engineers, Houston, pp. 548-560 (1982).

17. Volpicelli, G., L. Massimilla, and F.A. Zenz, *Nonhomogeneities in Solid-Liquid Fluidization*, in Fluidized-Bed Technology, J.A. Buckham and N.M. Levitz, eds., CEP Symposium Series, American Institute of Chemical Engineers, *62*(67):42-50 (1966).

18. Loew, O., B. Schmutter, and W. Resnick, *Particle and Bubble Behavior and Velocities in a Large-Particle Fluidized Bed With Immersed Obstacles*, Powder Technology, *22*:45-57 (1979).

19. Merry, J.M.D., and J.F. Davidson, *Gulf Stream Circulation in Shallow Fluidized Beds*, Trans. Institution of Chemical Engineers, *51*:361-368 (1973).

20. Patrose, B., and H.S. Caram, *Optical Fiber Probe Transit Anemometer for Particle Velocity Measurements in Fluidized Beds*, AIChE Journal, *28*(4):604-609 (July 1982).

21. Chen, M.M., B.T. Chao, and J. Liljegren, *The Effect of Bed Intervals on the Solids Velocity Distribution in Gas Fluidized Beds*, in Fluidization, D. Kunii and R. Toer, eds., Engineering Foundation, New York pp. 203-218 (1984).

22. Lin, J.S., M.M. Chen, and B.T. Chao, *A Novel Radioactive Particle Tracking Facility for Measurement of Solids Motion in Fluidized Beds*, AIChE J., *31*(3):465-473 (1985).

23. Rowe, P.N., and H. Masson, *Intersection of Bubbles with Probes in Ga Fluidized Beds*, Trans. Institution of Chemical Engineers, *59*:176-185 (1981).

24. Rowe, P.N., and D.J. Everett, *Fluidized Bed Bubble Viewed by X-Rays Part I - Experimental Details and the Interaction of Bubbles with Solid Surfaces*, Trans. Institution of Chemical Engineers, *50*:42-48 (1972).

25. Fakhimi, S., and D. Harrison, *The Void Fraction near a Horizontal Tube Immersed in a Fluidized Bed*, Trans. Institution of Chemical Engineers, *58*:125-131 (1980).

26. Davidson, J.F., *Symposium on Fluidization — Discussion*, Trans. Institution of Chemical Engineers, *39*:230-232 (1961).

27. Smoot, L., *Modeling of Coal-Combustion Processes*, Progress in Energy and Combustion Science, *10*(2):229-272 (1984).

28. Gidaspow, D., *Hydrodynamics of Fluidization and Heat Transfer: Supercomputer Modeling*, Twenty-Third National Heat Transfer Conf., Applied Mechanics Review *39*(1):1-23 (Jan. 1986).

29. Gidaspow, D., B. Ettehadieh, and R.W. Lyczkowski, *Computer Modeling of Fluidization of Sand in a Two-Dimensional Bed with a Jet*, presented at 74th Annual of Meeting AIChE (Nov. 8-12, 1981).

30. Gidaspow, D., B. Ettehadieh, C.L. Lin, and R.W. Lyczkowski, *Theoretical and Experimental Hydrodynamics of a Jet in a Fluidized Bed of Particles*, Proc. International Symp. on Powder Technology, 1981, K. Iinoya, K. Beddow, and G. Jimbo, eds., Society of Powder Technology, Kyoto, Japan, pp. 672-681 (1982).

31. Gidaspow, D., C.L. Lin, and Y.C. Seo, *Fluidization in Two-Dimensional Beds with a Jet: 1. Experimental Porosity Distribution*, I&EC Fundamentals, *22*:187-193 (1983).

32. Gidaspow, D., and B. Ettehadieh, *Fluidization in Two-Dimensional Beds with a Jet: 2. Hydrodynamic Modeling*, I&EC Fundamentals, *22*:193-201 (1983).

33. Ettehadieh, B., D. Gidaspow, and R.W. Lyczkowski, *Hydrodynamics of Fluidization in a Semicircular Bed with a Jet*, AIChE J., *30*(4):529-536 (1984).

34. Gidaspow, D., Y.C. Seo, and B. Ettehadieh, *Hydrodynamics of Fluidization: Experimental and Theoretical Bubble Sizes in a Two-Dimensional Bed with a Jet*, Chemical Engineering Communications, *22*:253-272 (1983).

35. Lyczkowski, R.W., J. Bouillard, and D. Gidaspow, *Computed and Experimental Motion-Picture Determination of Bubble and Solids Motion in a Two-Dimensional Fluidized Bed with a Jet and Immersed Obstacle*, Proc. Eighth International Heat Transfer Conf., Hemisphere Publishing Corp., Washington, D.C., Vol. 5, pp. 2593-2598 (Aug. 1986).

36. Rivard, W.C., and M.D. Torrey, *K-FIX: A Computer Program for Transient, Two-Dimensional, Two-Fluid Flow*, Los Alamos Scientific Laboratory Report LA-NUREG-6623 (April 1977).

37. Rivard, W.C., and M.D. Torrey, *K-FIX: A Computer Program for Transient Two-Fluid Flow — THREED: An Extension of the K-FIX Code for Three-Dimensional Calculations*, Los Alamos Scientific Laboratory Report LA-NUREG-6623, Supplement II (Jan. 1979).

38. Harlow, F.H., and A.A. Amsden, *Numerical Calculation of Multiphase Fluid Flow*, J. Computational Physics, *17*:19-52 (1975).

39. Lyczkowski, R.W., D. Gidaspow, C. W. Solbrig, and E.C. Hughes, *Characteristics and Stability Analyses of Transient One-Dimensional Two-Phase Flow Equations and Their Finite Difference Approximations*, Nuclear Science and Engineering, 66:378-396 (1978).

40. Rietma, K., and S.M.P. Mutsers, *The Effect of Interparticle Forces on Expansion of a Homogeneous Gas-Fluidization*, Proc. International Symp. on Fluidization, Toulouse, France, pp. 32-33 (1973).

41. Orr, C. Jr., *Particulate Technology*, Macmillan Co., New York, p. 421 (1966).

42. Shinora, K., *Rheological Property of Particulate Solids*, in Handbook of Powder Science and Technology, M.E. Fayed and L. Otten, eds., Van Nostrand Reinhold, New York, pp. 129-169 (1984).

43. Gidaspow, D., and M. Syamlal, *Solid-Gas Critical Flow*, presented at the 1985 Annual Meeting, AIChE, paper 74e (Nov. 1985).

44. Altiner, H.K. and J.F. Davidson, *Powder Flow from an Aerated Hopper*, in Fluidization, J.K. Grace, and J.M. Madsen, eds., Plenum Press, N.Y., pp. 461-460 (1980).

45. Ergun, S., *Fluid Flow Through Packed Columns*, Chemical Engineering Progress, *48*(2):89-94 (1952).

46. Wen, C.Y. and Y.H. Yu, *Mechanics of Fluidization*, Series No. 62, *62*, B.S. Lee, ed., American Institute of Chemical Engineers, N.Y., pp. 100-112 (1966).

47. Bouillard, J.X., *Hydrodynamics of Sedimentation, Fluidization, and Erosion*, Ph.D. Dissertation, Illinois Institute of Technology, Chicago, (Dec. 1986).

48. Buyevich, Y.A., V.N. Korolyov, and N.I. Syromyatnikov, *Hydrodynamic Conditions for the External Heat Exchange in Granular Beds*, in Heat and Mass Transfer in Fixed and Fluidized Beds, W.P.M. van Swaaij and N.H. Afghan, eds., Hemisphere Publishing Corp., Washington, D.C., pp. 333-342 (1986).

49. Engel, P.A., *Impact Wear of Materials*, Elsevier Scientific Publishing Co., Amsterdam (1978).

50. Sarkar, A.D., *Friction Wear*, Academic Press, New York (1980).

51. Wei, W., and Deffenbaugh, D., *Effect of Operating and Design Parameters on Fluidized-Bed Combustor In-Bed Metal Wastage-Literature Review*, Southwest Research Institute Draft Quarterly Report DOE/MC/22077-2022, San Antonio, (Feb. 1986).

52. Padhye, A.R., *Literature Review of Fundamental Erosion/Abrasion Models as Applicable to Wear of Fluidized Bed Internals*, Topical Report, EG&G WASC, Inc., Morgantown, W.Va. (Dec. 1985).

53. Urso, T.L., *Model for Single-Particle Erosion of Ductile Materials*, Morgantown Energy Technology Center, Morgantown, W.Va., U.S. Department of Energy Report DOE/METC-86/4066 (Jan. 1985).

54. Finnie, I., *The Mechanism of Erosion of Ductile Metals*, Proc. Third National Congress on Applied Mechanics, American Society of Mechanical Engineers, pp. 527-532 (1958).

55. Finnie, I., *Erosion of Surfaces by Solid Particles*, Wear, 3:87-103 (1960).

56. Pourahmadi, F., and J.A.C. Humphrey, *Modeling Solid-Fluid Turbulent Flows with Application to Predicting Erosion Wear*, Physico Chemical Hydrodynamics, *4*(3):191-219 (1983).

57. Finnie, I., *Some Observations on the Erosion of Ductile Metals*, Wear, *19*:81-90 (1972).

58. Finnie, I., and D.H. McFadden, *On the Velocity Dependence of Ductile Metals by Solid Particles at Low Angles of Incidence*, Wear, *48*:181-190 (1978).

59. Shewmon, P., and G. Sundararajan, *The Erosion of Metals*, Annual Reviews of Material Science, *13*:303-318 (1983).

60. Bitter, J.G.A., *A Study of Erosion Phenomena, Part I*, Wear, *6*:5-21 (1963).

61. Bitter, J.G.A., *A Study of Erosion Phenomena, Part II*, Wear, *6*:161-190 (1963).

62. Neilson, J.H., and A. Gilchrist, *Erosion by a Stream of Solid Particles*, Wear, *11*:111-122 (1968).

63. Sheldon, G.L., and I. Finnie, *The Mechanism of Material Removal in the Erosive Cutting of Brittle Materials*, Trans. ASME, Series B, J. Engineering for Industry, *88*:393-400 (1966).

64. Soo, S.L., *A Note on Moving Dust Particles*, Powder Technology, *17*:259-263 (1977).

65. Wood, R.T., and D.A. Woodford, *Tube Erosion in Fluidized Beds*, General Electric Co. Report 11/ET-FUC79, U.S. Energy Research and Development Administration Report 81-12 (Dec. 1980).

66. Fiore, N.F., K.C. Anthony, and T.H. Kosel, *Abrasion in Multiphase Alloys*, Proc. Corrosion-Erosion-Wear of Materials in Emerging Fossil Energy Systems, Berkeley, Calif. Jan. 17-19, 1982, A.V. Levy, ed., National Assn. of Corrosion Engineers, Houston, pp. 266-294 (1982).

67. Hutchings, I., *Some Comments on the Theoretical Treatment of Erosive Particle Impacts*, Paper No. 36, Proc. Fifth International Conf. on Erosion by Liquid and Solid Impact, Cambridge, England (Sept. 1979).

68. Wood, R.T., and D.A. Woodford, *Tube Erosion in Fluidized Beds*, Paper No. 42, Proc. Fifth International Conf. on Erosion by Liquid and Solid Impact, Cambridge, England (Sept. 1979).

69. Jennings W.H., W.J. Head and C.R. Manning, Jr., Wear, *40*:93-112 (1976).

70. Tabakoff, W., *Erosion Behavior of Materials in Multiphase Flow*, Proc. Corrosion-Erosion-Wear of Materials in Emerging Fossil Energy Systems, Berkeley, Calif., Jan. 17-19, 1982, A.V. Levy, ed., National Assn. of Corrosion Engineers, Houston, pp. 642-676 (1982).

71. Wolak, J., P. Worm, I. Patterson, and J. Bodia, *Parameters Affecting the Velocity of Particles in an Abrasive Jet*, Trans. ASME, J. Engineering Materials & Technology, *99*:147-152 (1977).

72. Tsai, W., J.A.C. Humphrey, I. Cornet and A.V. Levy, *Experimental Measurement of Accelerated Erosion in a Slurry Pot Tester*, Wear, *68*:289-303 (1981).

73. Hussain, M.F., and W. Tabakoff, *Dynamic Behavior of Solid Particles Suspended by Polluted Flow in a Turbine Stage*, J. Aircraft, *10* (July 1973).

74. Hussain, M.F., and W. Tabakoff, *Computation and Plotting of Solid Particulate Flow in Rotating Cascades*, Computers and Fluids, *2* (1974).

75. Grant, G., and W. Tabakoff, *Erosion Predictions in Turbomachinery Resulting from Environmental Solid Particles*, J. Aircraft, *12*:642-676 (May 1975).

76. Stringer, J., Electric Power Research Institute, Palo Alto, Calif., personal communication (Oct. 25, 1985).

77. Sheldon, G.L., J. Maji, and C.T. Crowe, *Erosion of a Tube by Gas Particle Flow*, Trans. ASME, Series H, J. Engineering Materials and Technology, *99*:138-142 (1977).

78. Crowe, C.T., M.P. Sharma and D.E. Stock, *The Particle-Source-In Cell (PSI-Cell) Model for Gas-Droplet Flows*, J. Fluids Engineering, *99*:325-332 (1977).

79. Rudinger, G., and A. Chang, *Analysis of Non-steady Two-Phase Flow*, Physics of Fluids, *7*:1747-1754 (1964).

80. Gosman, A.D., and W.M. Pun, *Calculation of Recirculating Flows (lecture notes)*, Imperial College, London, Report HTS/74/2 (1974).

81. Mason, J.S., and B.V. Smith, *The Erosion of Beds by Pneumatically Conveyed Suspensions of Abrasive Particles*, Powder Technology, *6*:323-335 (1972).

82. Ushimaru, K., C.T. Crowe, and S. Bernstein, *Design and Applications of the Novel Slurry Jet Pump*, Energy International, Inc., Report EI84-108 (Oct. 1984).

83. Kick, F., *Dar Gesetz der proportionalen Widerstande und seine Anwendung*, Leipzig, Germany (1885).

84. Walker, D.R., and M.C. Shaw, *A Physical Explanation of the Empirical Laws of Comminution*, AIME Mining Engineering Transactions, *6*:313-320 (1954).

85. Rabinowicz, E., *Friction and Wear of Materials*, Wiley, New York (1965).

86. Shook, C.A., S.K. Ghosh, and F.E. Pilling, *Wall Erosion in Slurry Couette Flow*, in Liquid-Solid Flows and Erosion Wear in Industrial Equipment, M.C. Roco, ed., American Society of Mechanical Engineers, New York, pp. 63-68, (1983).

87. Mulhearn, T.O. and L.E. Samuels, *The Abrasion of Metals: A Model of the Process*, Wear, 5:478-498 (1962).

88. Von Rittinger, P.R., *Lehrbuch der Aufbereitungskunde*, Ernstand Korn, Berlin (1867).

89. Bird, R.B., W.E. Stewart, and E.N. Lightfoot, *Transport Phenomena*, Wiley, New York, 3rd printing, (1960).

90. Hwang, C.J., *A Theoretical Study of Compressible Two-Phase Interval Flow* (doctoral dissertation), University of Tennessee, U.S. Department of Energy Report DOE/ET/10815-99 (Aug. 1984).

91. Leckner, B., F. Johnson, and S. Andersson, *Erosion in Fluidized Beds — Influence of Bubbles*, in Workshop on Materials Issues in Fluidized Bed Combustion, Nova Scota, July 29-Aug. 1, 1985, EPRI (1985).

92. Lockwood, D.W., *Effects of Heat Exchanger Tube Spacing and Arrangement on the Quality of Fluidization*, Proc. Second Pacific Chemical Engineering Congress, American Institute of Chemical Engineers, New York, Vol. II, pp. 1177-1181 (Aug. 1977).

93. Parkinson, M.J., J.F.G. Grainger, A.W. Jury, and T.J. Kempton, *Tube Erosion at IEA Grimethrope: Cold Model Studies at CRE*, in Reports Commissioned by the Project from Outside Consultants and Others, NCB (IEA Grimethorpe) Ltd., Barnsley, S. Yorkshire, U.K., Vol. 2, (Sept. 1984).

94. Jansson, S.A., *Erosion and Erosion-Corrosion in Fluidized Bed Combustor Systems*, presented at Conf. on Corrosion-Erosion-Wear of Materials in Emerging Fossil Energy Systems, Berkeley, Calif. (Jan. 27-29, 1982).

95. *Materials-Related Problems and Investigations during Test Series I, Category II*, NCB (IEA Grimethorpe) Ltd. Fluidized Bed Combustion Project, Grimethorpe Experimental Facility, U.S. Department of Energy Report GEF/U83116 and DOE/ET/10393-1653 (DE84011999) (Sept. 1984).

96. DeCoursin, D.G., *Materials and Components in Fossil Energy Applications*, U.S. Department of Energy Newsletter, DOE/FE-0053/34, p. 7 (Oct. 1981).

97. Vaux, W.G., and R.A. Newby, *Wear on Tubes by Jet Impingement in a Fluidized Bed*, Powder Technology, *19*:79-88 (1979).

98. Bouillard, J.X., R.W. Lyczkowski, S. Folga, D. Gidaspow, and G.F. Berry, *Hydrodynamics Erosion of Heat Exchanger Tubes in Fluidized-Bed Combustors*, Canadian Journal of Chemical Engineering, 67:218-229 (April 1989).

99. Bouillard, J.X., R.W. Lyczkowski, and D. Gidaspow, *Hydrodynamics of Fluidization: Time-Averaged and Instantaneous Porosity Distributions in a Fluidized Bed with an Immersed Obstacle*, paper submitted to AIChE Journal (July 1987); accepted for publication (March 1989).

APPENDIX A:

SOME CONVERSION FACTORS USEFUL IN EROSION CALCULATIONS

Energy

$$10^7 \text{ erg/s} = \text{J/s} = \text{W}$$

Energy Dissipation

$$\dot{m}_s \vec{v}_s^{\,2} = \text{kg/s}^3 = \text{J/(s}\cdot\text{m}^2\text{)} = \text{W/m}^2$$

$$dKE_s/dt = \dot{m}_s \frac{d\vec{v}_s}{dt_s} = \text{kg/(m}\cdot\text{s}^3\text{)} = \text{J/(s}\cdot\text{m}^3\text{)} = \text{W/m}^3$$

Erosion rate

$$1 \text{ mm/1000 h} = 1 \text{ μm/h} = 2.77 \times 10^{-10} \text{ m/s}$$

Power

$$\text{J} = \text{N}\cdot\text{m} = \text{kg}\cdot\text{m}^2/\text{s}^2$$

Pressure

$$10 \text{ dyne/cm}^2 = \text{Pa}$$

$$9.8 \times 10^6 \text{ kgf/mm}^2 = \text{Pa}$$

$$\text{Pa} = \text{J/m}^3 = \text{kg/(m}\cdot\text{s}^2\text{)}$$

APPENDIX B: DEFINITIONS

Elasticity. A material is elastic so long as the strain disappears with the removal of the load. The elastic limit is the greatest stress a material is capable of developing without incurring permanent deformation on removal of the stress. In the case of ferrous materials (e.g., steel or iron), the deformation (strain), up to the elastic limit, is proportional to the stress; this is known as Hooke's law. The slope of the curve, E, is called the elasticity Young's modulus (see Fig. B.1). At the yield point (or yield stress), the material starts to act inelastically (or plastically). Brittle metals, such as cast iron, have a stress-strain curve that rises continuously until rupture occurs. However, ductile materials may show a domain of plasticity before fracture (Fig. B.1). When a material is deformed in its plastic range, it becomes permanently deformed.

Fatigue. Materials subjected to repeated stresses show failures at a stress considerably lower than the ultimate strength of the material; such failures are referred to as fatigue failures. In this case, spreading of small cracks occurs.

Hardness. Hardness is the ability of a material to resist penetration, wear, or scratching. The property of hardness is complex in nature and cannot be said to depend solely upon strength or any individual property. A number of methods for determining relative hardness are used. Some of them measure the penetrability of the material, as is done for the Brinell, Rockwell, Vickers, and Monotron testing machines. The Shore Scleroscope uses a dropped weight, for which the height of bounce is measured. Certain nonmetallic materials are tested for hardness by their resistance to scratching by another substance. Ten materials arranged in order form the basis of comparison in Mohs' scale of hardness. In Table 3, Sec. 5.2.4, the respective Diamond Pyramid hardnesses of different materials used in fluidized-bed combustors are listed.[65]

Strain. A strain is a dimensionless number; for a compressive or a tensile load, the strain is expressed as the ratio of the change of length, ΔL, per unit of length, L, as follows:

$$\text{Strain} = \Delta L/L \qquad \text{(B.1)}$$

In general, the strain is a tensor of order 3.

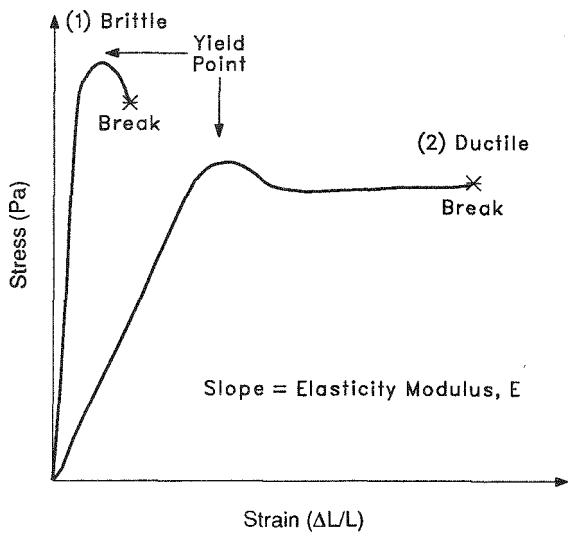

FIGURE B.1 Stress-Strain Diagram for Brittle and Ductile Materials

APPENDIX C:

DERIVATION OF THE ENERGY DISSIPATED BY A FLUIDIZED BED

The purpose of this appendix is to derive an approximate expression for the total energy dissipated by a fluidized bed. This expression is then compared with the solids energy dissipation rates around the rectangular obstacle analyzed in Section 6.

A derivation similar to that used to derive the energy dissipated by the solids phase, Eq. 5.25, can be used to obtain the energy dissipated by the gas phase.[98] If all terms except the one corresponding to term 4 involving the drag are neglected, we obtain

$$-e_{vg} = \vec{v}_g \cdot \bar{\bar{\beta}} \cdot (\vec{v}_s - \vec{v}_g) \tag{C.1}$$

The gas velocity in the x direction is much less than the gas velocity in the y direction, which is much greater than the solids velocity in the y direction. Consequently, Eq. C.1 is approximately equal to the total kinetic energy dissipated per unit volume and may be integrated over the volume of the bed, V_{bed}, to obtain the total energy dissipated, E_v, as

$$-E_v = -\int_{V_{bed}} e_{vg} dV = \int_{V_{bed}} V_g \beta_y (V_s - V_g) dV \tag{C.2}$$

Since, as shown by Bouillard, Lyczkowski and Gidaspow,[99]

$$-\left(\frac{\beta_y}{\varepsilon}\right)(V_s - V_g) = (\rho_s - \rho_g)(\varepsilon_s g) \tag{C.3}$$

Equation C.3 may be rearranged, assuming $\rho_g << \rho_s$, to obtain

$$-\beta_y (V_s - V_g) \simeq \varepsilon \rho_s \varepsilon_s g \tag{C.4}$$

Substitution of Eq. C.4 into Eq. C.2 produces

$$E_v = \int_{V_{bed}} V_g \varepsilon \rho_s \varepsilon_s g \, dV \tag{C.5}$$

Because dV = dAdy, Eq. C.5 may be rewritten as

$$E_v = \int_{A_{bed}} \rho_s g \left(\int_0^h \varepsilon_s \, dy\right) V_g \, \varepsilon \, dA \tag{C.6}$$

Because solids do not leave the bed, $\rho_s \int_0^h \varepsilon_s \, dy$ represents the total solids mass per unit cross-sectional bed area, $\rho_s \varepsilon_{so} h$, where ε_{so} is the initial solids porosity in the fluidized bed having height, h. Therefore, Eq. C-6 may be expressed as

$$E_v = (\rho_s \varepsilon_{so} gh) \int_{A_{bed}} V_g \, \varepsilon \, dA \tag{C.7}$$

The integral in Eq. C.7 represents the total gas superficial velocity and equals that entering through the bed bottom.

As shown in Fig. 2 (Sec. 2.2), pure gas enters the bed through the jet and secondary flow areas, A_{jet} and A_{sec}, respectively at velocities V_{jet} and V_{sec}, respectively. The final approximate result for the total energy dissipated by the bed is therefore given by

$$E_v = (\rho_s \varepsilon_{so} gh) \left[(AV)_{jet} + (AV)_{sec}\right] \tag{C.8}$$

Equation E.8 is the final result given in Eq. 6.2.